THERMAL STUDY OF VULNERABLE ATHEROSCLEROTIC PLAQUE

A Dissertation

by

TAEHONG KIM

Submitted to the Office of Graduate Studies of
Texas A&M University
in partial fulfillment of the requirements for the degree of

DOCTOR OF PHILOSOPHY

December 2007

Major Subject: Mechanical Engineering

THERMAL STUDY OF VULNERABLE ATHEROSCLEROTIC PLAQUE

A Dissertation

by

TAEHONG KIM

Submitted to the Office of Graduate Studies of
Texas A&M University
in partial fulfillment of the requirements for the degree of

DOCTOR OF PHILOSOPHY

Approved by:

Chair of Committee,	Obdulia Ley
Committee Members,	Kalyan Annamalai
	Raymundo Arroyave
	Jay R. Walton
Head of Department,	Dennis O'Neal

December 2007

Major Subject: Mechanical Engineering

ABSTRACT

Thermal Study of Vulnerable Atherosclerotic Plaque. (December 2007)

Taehong Kim, B.S., Ajou University;

M.S., Texas A&M University

Chair of Advisory Committee: Dr. Obdulia Ley

Atherosclerotic plaques with high probability of rupture show the presence of a hot spot due to the accumulation of inflammatory cells. This study utilizes two and three dimensional (2-D and 3-D) arterial geometries containing an atherosclerotic plaque experiencing different levels of inflammation and uses models of heat transfer analysis to determine the temperature distribution in the plaque region.

The 2-D studies consider three different vessel geometries: a stenotic straight artery, a bending artery and an arterial bifurcation which model a human aorta, a coronary artery and a carotid bifurcation, respectively. The 3-D model considers a stenotic straight artery using realistic and simplified geometries. Three different blood flow cases are considered: steady-state, transient state and blood flow reduction. In the 3-D model, thermal stress produced by local inflammation is estimated to determine the effect of inflammation over plaque stability. For fluid flow and heat transfer analysis, Navier-Stokes equations and energy equation are solved; for structural analysis, the governing equations are expressed in terms of equilibrium equation, constitutive equation, and compatibility condition, which are are solved using the multi-physics software COMSOL 3.3 (COMSOL, Inc.).

Our results indicate that the best location to measure plaque temperature in the presence of blood flow is recommended between the middle and the far edge of the plaque. The blood flow reduction leads to a non-uniform temperature increase ranged from 0.1 to 0.25 ^oC in the plaque/lumen interface. In 3-D realistic model,

the multiple measuring points must be considered to decrease the potential error in temperature measurement even within 1 or 2 mm at centerline region of plaque. The most highly thermal stressed regions with the value of 1.45 Pa are observed at the corners of lipid core and the plaque/lumen interface.

The mathematical model developed provides a tool to analyze the factors affecting heat transfer at the plaque surface. The results may contribute to the understanding of the relationship between plaque temperature and the likelihood of rupture, and also provide a tool to better understand arterial wall temperature measurements obtained with novel catheters.

ACKNOWLEDGMENTS

My research is very much the product of a sustained collective endeavour and love. First of all, I would like to thank GOD for leading me whenever I was in difficult problems of my life. Also, I would like to express my deepest gratitude to Dr. Obdulia Ley for her consistent care, enthusiasm, and untiring patience throughout every step of this research. This dissertation would not have been possible without her help. My appreciation goes to Dr. K. Annamalai, Dr. R. Arroyave, and Dr. J. Walton for their guidance and kindness while serving on my advisory committee.

Special thanks are extends to my family in Korea for their unfailing love and encouragement during my Ph.D. program.

Finally, I am most indebted to my wife, Grace Rhee, for being incredibly understanding, supportive, and most of all, patient, and for even helping practice of the final exam. My GOD's gifts, David Inho and Daniel Siho, when they grow up old enough to read, I hope they are proud of their Daddy.

TABLE OF CONTENTS

CHAPTER Page

LIST OF TABLES

LIST OF FIGURES

FIGURE Page

FIGURE Page

CHAPTER I

INTRODUCTION

A. Background

1. Clinical significance of atherosclerosis

Atherosclerosis refers to lesions in which there is an increase in the thickness of the vessel wall. The atherosclerotic lesion is characterized by the accumulation of lipid and connective tissue, which can eventually obstruct blood flow producing stenosis, an abnormal narrowing in a blood vessel, predisposing the vessel to thrombosis, and impairing the vessel's elastic response. Atherosclerosis is a pathological process leading to several important human vascular disorders, including coronary artery disease, cerebrovascular disease, and diseases of the aorta and the peripheral arterial circulation. These disorders, that occur when plaques rupture, are responsible for more deaths than any other diseases in humans [1]. In the United States, nearly 1.1 million patients suffer from acute myocardial infarction (AMI) every year [2], and almost two thirds of the acute coronary syndromes pass undetected [3]. Since 1900, cardiovascular disease (CVD) has been the number-one killer in the United States and accounted for about 37% of all 2.4 million deaths in 2003 [2]. More than 71 million American adults have one or more type of CVD and 13 million suffer from coronary artery disease (CAD) in the United States. More than 60% of these thrombi are caused by sudden rupture of an unstable or vulnerable plaque [4, 5, 6].

Atherosclerosis develops over a long period of time before symptoms appear and

---

This dissertation follows the style of *IEEE Transactions on Biomedical Engineering*.

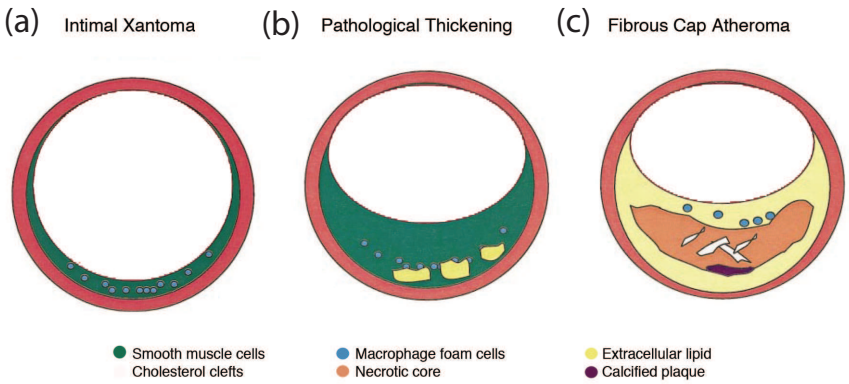

Fig. 1. Plaque classified based on morphological description **(a)** Intimal xantoma is a pre-atherosclerotic lesion that usually does not develop into progressive lesions. **(b)** Pathological intimal thickening is an intermediate type lesion where true necrosis is not apparent and shows scattered macrophages. **(c)** Fibrous cap atheroma. [4]

in 50% of the population it is asymptomatic. Early detection and follow up of such vulnerable plaques are a major challenge to prevent acute coronary syndromes and cardiac events. Unfortunately, current diagnostic methods are unable to reliably predict the high risk plaque associated with a particular lesion. The various stages of atherosclerosis before plaque rupture are classified as: intimal xantoma, pathological intimal thickening, and fibrous cap atheroma (Figure 1).

In recent years, cardiovascular research has sought potential clinical strategies to overcome the limited ability to detect high-risk plaques and eventually guide targeted therapy [7]. Traditionally, angiography has been used to detect and characterize atherosclerotic plaque by considering only the plaque size, and the level of occlusion in artery. It has been reported that plaque composition rather than the degree of stenosis determines the risk of acute coronary syndrome [8, 9]. In 1998, a research team showed that about 70% of myocardial infarctions (MIs) involved small non-obstructive lesions,

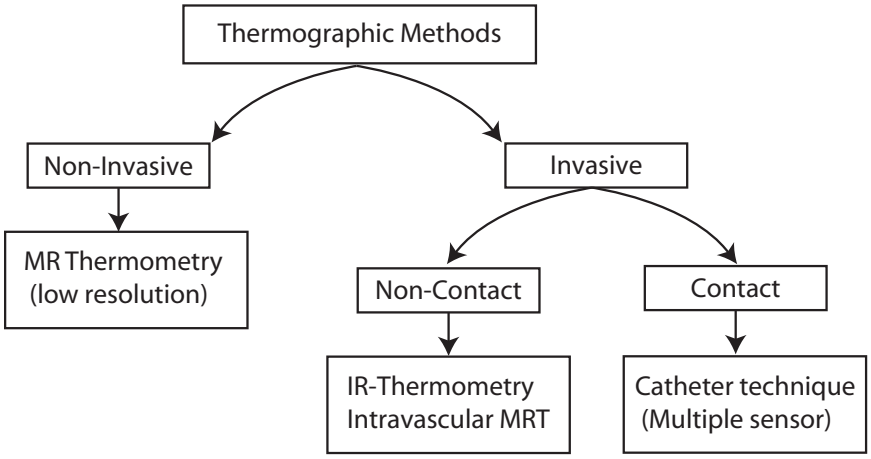

Fig. 2. Classification of arterial wall thermometry methods available in clinical practice.

that showed high activity and instability; these lesions are referred as vulnerable plaque [10]. It has been observed that a coronary atherosclerotic plaque can rupture and produce a cardiac event long before it produces significant lumen narrowing [11]. A series of autopsy studies have demonstrated that vulnerable plaques that undergo rupture and erosion are correlated with the appearance of local inflammation sites at the arterial wall [12, 13]. In-vivo studies have shown that there is thermal heterogeneity in human carotid atherosclerotic plaques, and that heat released by activated inflammatory cells of atherosclerotic plaques may be detected to predict rupture and thrombosis, both factors leading to acute coronary syndrome (ACS) and sudden cardiac death [14, 15, 16]. In recent years, cardiovascular research has sought potential clinical strategies to overcome the limited ability to detect high-risk plaques and eventually guide targeted therapy [7, 17].

Given the increased interest in plaque activation, metabolism and consequently temperature [3, 18, 19, 20], clinicians have developed different techniques to measure the temperature inhomogeneity; these techniques have received the name of

Arterial Wall Thermography (AWT) [19], and its classification is shown in Figure 2. Thermographic methods can be categorized into invasive and non-invasive. Magnetic resonance thermometry (MRT) is a novel non-invasive method for studying tissue temperature, but lacks the required resolution when it comes to small regions, such as blood vessels. The invasive techniques are divided into two main groups: non-contact and contact techniques. The non-contact techniques are based on detection of oxygen concentration and tissue metabolic activity using nuclear magnetic resonance, other spectroscopy techniques, or detection of infrared radiation emitted by the inflamed plaque. Infrared (IR) thermal imaging used in dermatology to study skin disease and tumors has limitations of accuracy, resolution for scattering of IR radiation by blood particles as well as limitations related to depth [15]. The contact or direct measurement techniques are based on the fabrication of special catheters using thermocouples. As a direct measuring tool, a catheter-based technique is used to identify plaques that are prone to rupture and thrombosis. Independently of their invasiveness, the catheter techniques are the most feasible to measure AWT because thermal mapping of the arterial wall using basket catheters with multiple thermal sensors provides the best way of analyzing spatial gradients and therefore, localize the hot spot [13, 15, 18, 19]. Figure 3 shows different thermography catheters utilized in vivo. Contact thermography using catheter in general provides in vivo temperature data that is underestimated due to the cooling effect of continuous blood flow [16, 21]. A good thermal contact on the vascular wall is required to satisfy accurate and reproducible temperature measurements because of the possibility of passing close to the hottest point of the arterial wall [18]. This technique can generally obstruct blood flow and cause major complications, such as plaque rupture due to tearing the sensitive and unstable plaque surface. Under these limitations, more effective measurement strategies are essential to improve outcome to predict which of the atherosclerotic

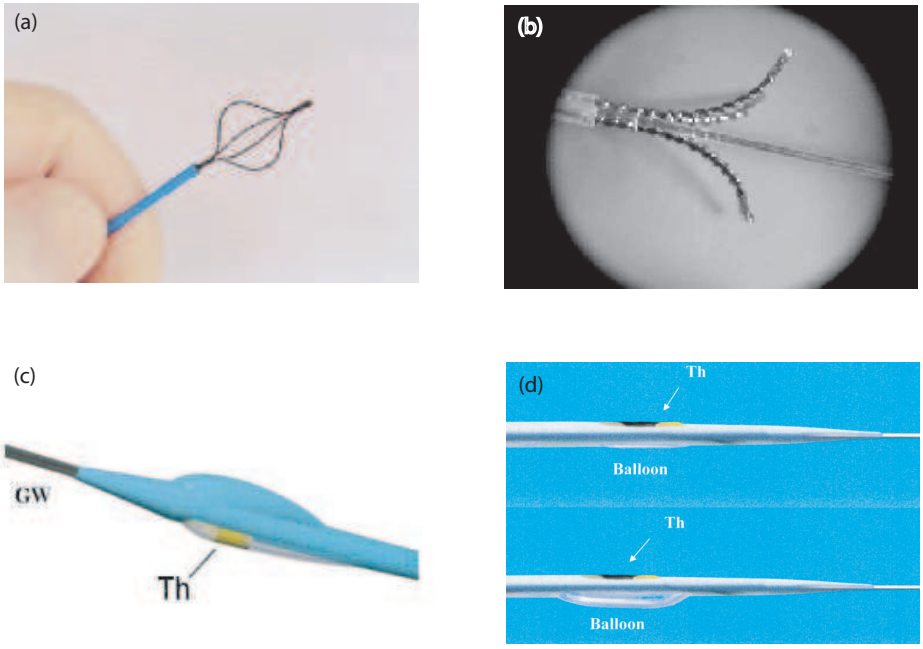

Fig. 3. Different thermography catheters: **(a)** thermography basket catheter using thermocouple at the maximum curve of each nitinol wire [3], **(b)** four deployable flexible sensor-equipped arms catheter [19], **(c)** catheter with hydrofoil designed to use blood stream to drive thermistor against vessel wall [13], and **(d)** balloon-thermography catheter with balloon to inflate for the interruption of the flow during temperature recording [16].

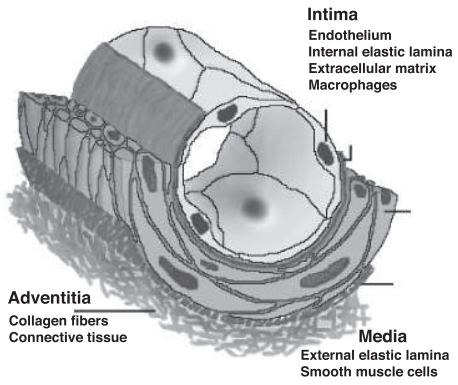

Fig. 4. Cross-sectional diagram showing the major tissue layers in a normal human artery.

plaque are prone to rupture and hence distinguish metabolically active or vulnerable plaques.

B. Vessel Structure

1. Arterial wall

A blood vessel consists of two regions: arterial wall and lumen where blood flows. Structurally, the walls of arteries and veins are divided into three layers: intima, media and adventitia as shown in Figure 4. Intima consists of connective tissue, smooth muscle cells and a few isolated macrophages. It contains the innermost layer of flattened endothelial cells (endothelium) where acts as a non-thrombogenic physical barrier between the blood and the rest of the intima. Media is the muscular part of arterial walls responsible of mechanical strength and of controlling the vascular tone. Adventitia is the outer and highly microvascular layer, which contains collagen, elastic fibrils, smooth muscle cells, and lymphatic channels [1]. As soft tissues, arterial walls have anisotropic and highly nonlinear mechanical properties. In this study, the three

layers of arterial walls are assumed to have homogeneous and isotropic mechanical and thermal properties. We are interested in thermal properties, as mathematical models will be employed to calculate plaque and arterial wall temperature; and elastic material properties will be introduced in the last part of this study to estimate the thermal stress produced by the formation of hot spots in the inflamed plaque.

2. Blood and its constituents

Blood is essentially a two-phase fluid consisting of cellular components (red blood cells, white blood cells, and platelets) and a liquid medium (plasma). The plasma of the blood occupies about 55% of the blood volume and carries a variety of substances including plasma proteins, non-protein nitrogen, electrolytes, hormones, enzymes and blood gases [22]. The cellular components of the blood account for approximately 40% of the blood by volume. The most numerous cellular component is the red blood cell (erythrocyte) which is soft and flexible, and can travel through the smallest capillaries. An important constituent, hemoglobin, in erythrocyte binds and transports oxygen. Another major type is the white cell (leukocyte) which primarily defends the body against invasion by infectious agents, repairs damaged tissues, and participates in immune reactions. Monocytes comprise about 3 to 8% of the total leukocyte population and their surfaces are characterized by thin folds to engulf material by endocytosis [22, 23]. These cells are suspended in the blood, slide through the endothelium, and accumulate in regions experiencing inflammation, which play an important role in the progression of atherosclerotic disease and plaque rupture. In this study, the blood is assumed to be a homogeneous and Newtonian fluid.

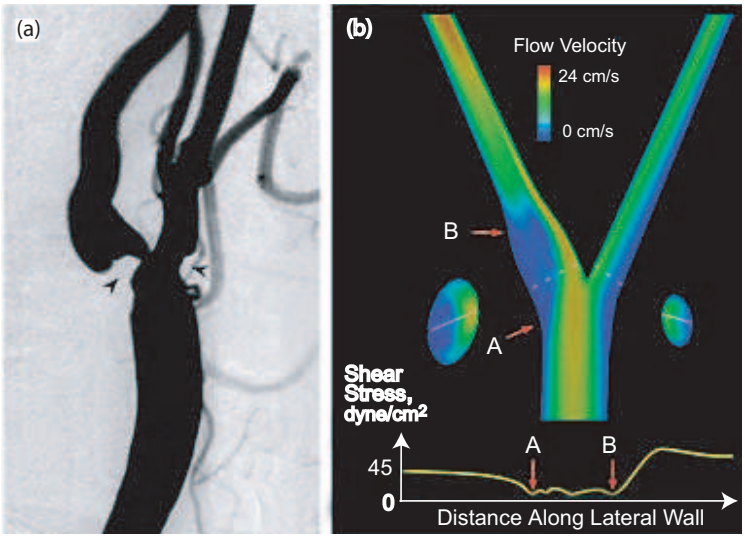

Fig. 5. **(a)** Focal narrowing at the outer walls (arrowheads) of carotid bifurcation in a 75-year-old man who experienced an embolic stroke, and **(b)** velocity map and wall shear stress using computational modeling. The regions A and B with lower velocity and shear stress correspond exactly to the location of the atherosclerotic lesion shown in the carotid bifurcation of part **(a)** [25].

C. Process of Plaque Formation

1. Localization of atherosclerotic plaque

Atherosclerosis occurs mainly in larger and medium-size arteries, which involves an abnormal accumulation of high molecular weight lipoprotein in the arterial wall [24]. In humans, atherosclerotic deposits are most frequently observed in abdominal aorta, coronary arteries, arteries of legs (femoral, iliac, etc.), arch and descending thoracic aorta, internal carotids, and Circle of Willis (arteries of the brain). The lesions are often related with the most susceptible areas where blood flow has flow separation and circulation, resulting in a weak net hemodynamic shear stress [1]. Thus, the disease tends to be localized in regions of the outer walls of bifurcations and the inner walls

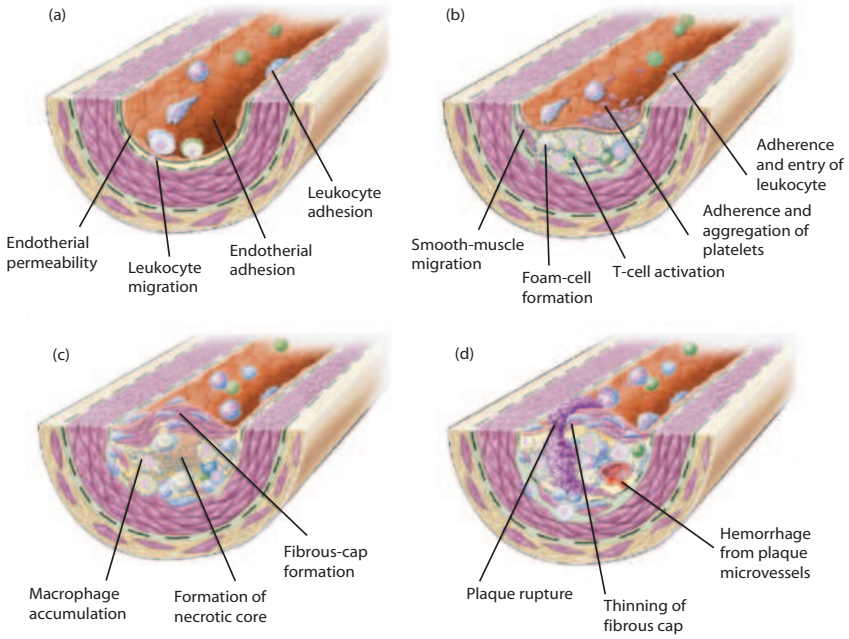

Fig. 6. Stages of atherosclerosis. **(a)** Endothelial dysfunction, **(b)** fatty streak formation, **(c)** formation of an advanced and complicated lesion, and **(d)** disruption of endothelium and thrombus formation [27].

of curvatures where fluid shear stress (shear rate) is altered from its normal patterns [24, 26]. These locations correspond to arterial bends, bifurcations, and in general sites presenting low wall shear stress [1, 24, 26]. Figure 5 shows that the location of atherosclerotic plaque corresponds exactly to the regions with lower velocity and lower shear stress as indicated by computational models [25].

2. Stages of atherosclerosis

Figure 6 presents the histopathological features that precede the formation of an advanced atherosclerotic lesions [27]. The first stage of atherosclerosis corresponds to *endothelial dysfunction* (Figure 6(a)), which is characterized by increased endothelial permeability to lipoproteins and other plasma constituents. Formation of atheroscle-

rotic lesions is proceeded by intimal thickness and lipid accumulation [1]. *Fatty streak* (Figure 6(b)) is the first macroscopically visible stage of atherosclerosis, which initially consists of lipid-laden molecules: monocytes, macrophages (foam cells) and T-lymphocytes [1, 27]. *Intermediate and advanced lesions* in Figure 6(c) tend to form a fibrous cap that walls off the lesion from the lumen. Fibrous cap covers a mixture of leukocytes, lipid and debris, which give rise to a necrotic core. These lesions expand at their shoulders by means of continued leukocyte adhesion and infiltration. *Disruption of plaque* (Figure 6(d)) leads to the formation of an occlusive thrombus, leading to unstable plaque surface or fibrous cap; this produces clinical complications like angina, MI, or sudden death [17, 27]. More recent theories indicate that a significant contribution to the initiation and progression of atherosclerotic plaque is led by direct transport through the *vasa vasorum* or the capillary network feeding the external surface of the arterial wall [28, 29].

3. Inflammation by macrophages

Inflammatory process develops from the early stages of atherosclerotic disease and worsen until rupture is observed. High metabolic activation rate of macrophage leads to increasing heat production in areas of macrophage accumulation and promotes plaque rupture or thrombosis and vasoconstriction in non-ruptured but inflamed plaques [3]. The presence of macrophages in inflamed plaques is responsible for temperature heterogeneity observed around the lesions, and it is considered as a precursor of the ischemic events discussed before [17]. Macrophages encountered in the atherosclerotic plaque are derived from circulating monocytes, which adhere to the injured vessel wall in areas of low wall shear stress [26]. Active macrophages embedded in the vulnerable plaques secrete inflammatory cytokines; these cytokines, in turn, stimulate the production of reactive oxygen species and proteolytic enzymes

which may influence plaque stability and evolution of atherosclerotic plaque [30, 31]. The high glucose uptake and the oxygen consumption of the macrophages cause an increase in the local temperature [17]. Inflamed plaques showed the hot temperature regions varied reproducibly by $0.2 - 0.3\ ^oC$, and 37% of the plaques had substantially warmer regions ($0.4-2.2\ ^oC$) [12]. Inflammation at the immediate site of plaque rupture plays an important role in the destabilization of plaque because macrophages release enzymes that digest extracellular matrix and weaken the overlying fibrous cap [16, 30].

4. Constituents of vulnerable plaque

Temperature heterogeneity has important clinical implication as it provides information about plaque composition (i.e., macrophage content, level of inflammation and cell activation) and vulnerability (rate of which fibrous cap is weaken) [30]. Post-mortem evaluation reports that rupture-prone plaques are characterized by a thin fibrous cap, a large lipid pool in the core of the plaque, and increased macrophage activity [9, 14]. Ex-vivo studies showed that temperature positively correlated with the density of macrophages and inversely with the distance of the cell clusters from the luminal surface in the plaque (fibrous cap thickness) [12, 17]. As the temperature increases, the core becomes softer and more likely to rupture [17]. A soft core may be more vulnerable to rupture because it may not be able to bear the imposed circumferential stress, which is then redistributed to the fibrous cap [18, 30]. The fibrous cap is weakened, which displays strongly reduced numbers of smooth muscle cells and becomes more and more friable [4].

Hence, the vulnerable plaque structure is characterized by the parameters affecting temperature heterogeneity: thickness of plaque, density of macrophage cells, thickness and length of macrophage layer, and depth of macrophage layer (fibrous

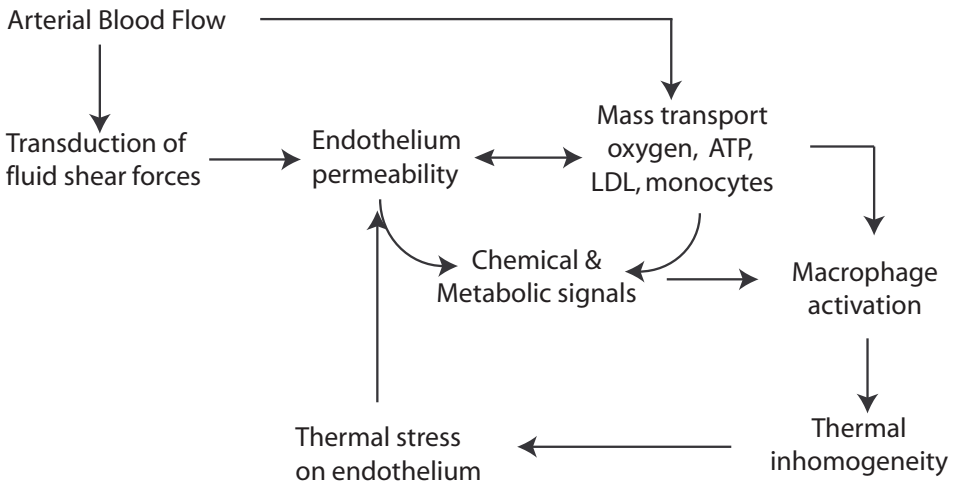

Fig. 7. Factors affecting evolution of atherosclerosis. Thermal stress due to thermal inhomogeneity affect endothelium permeability at plaque surface as soft tissues.

cap thickness) embedded in plaque. Concurrently, the factors characterized by the local temperature heterogeneity can be used to estimate the plaque instability.

5. Thermal stress due to inflammatory process

As we have introduced, the atherosclerotic plaques loaded with inflammatory cells show local regions with thermal heterogeneity. The hot spots are formed due to the transport of macromolecules and activation of macrophage or inflammatory cells embedded in plaque [3, 13, 14, 15, 16, 18, 19, 20]. The appearance of local inflammation sites at the arterial wall are correlated with the likelihood of plaques rupture and erosion [12, 13].

Over the last two decades, plaque rupture has been believed to be related to a variety of physical factors: mechanical shear stress experienced by the endothelial lining the blood vessels [32, 33, 34, 35], circumferential stress distribution [6, 36, 37, 38, 39] and transport and accumulation of macromolecules [40, 41, 42]. Richardson and

colleagues using 2-D simplified computer modeling identified that the stress concentration regions correlate with the locations of plaque rupture [38]. Other studies also using 2-D arterial segment suggested that the circumferential stress is more critical factor to explain a mechanism of overall plaque rupture [36, 37]. All these studies have used isothermal conditions as they have not considered any local heat production to estimate the plaque instability.

This study hypothesizes that the temperature changes in the inflammatory process might cause thermal stress that contributes to weakening of the sensitive plaque surface including enzymic degradation of the connective tissue matrix. This might directly affect endothelium permeability and, consequently cause the evolution of atherosclerosis and plaque vulnerability in Figure 7. Thus, thermal stress may be one of the important factors leading to the plaque evolution and affecting the plaque vulnerability.

D. Motivation and Objectives

In this study, 2-D and 3-D geometrical models of vulnerable plaques are considered, and used to determine plaque temperature distribution by solving the energy and Navier-Stokes equations in selected vessel geometries. As shown in Figure 8, this research intends to quantify the factors that contribute to plaque instability and disruption with the local thermal heterogeneity observed in atherosclerotic plaques. In the 2-D model, plaque is defined by variable parameters such as a lipid core, the thickness of fibrous cap, and the population of macrophages in the lesion. The relationships between the parameters defined and the plaque temperature distributions are analyzed using steady and unsteady calculations. In order to investigate the cooling effect of blood flow, the blood flow occlusion is analyzed assuming that the

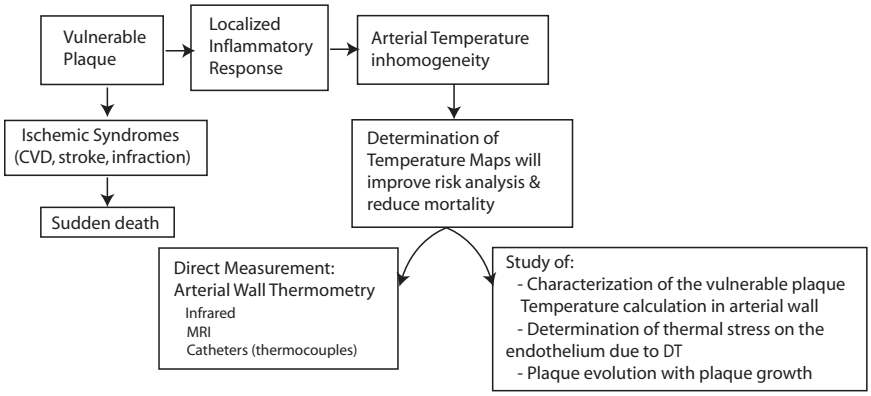

Fig. 8. Motivation and procedures of this research.

blood flow in lumen is gradually reduced when a catheter is introduced to measure the plaque surface temperature. A 3-D model of an atherosclerotic artery is created to study thermal stress based on the temperature changes produced by the inflammatory process. This study is important because the temperature changes in the inflammatory process can cause thermal stress to weaken the sensitive plaque surface and directly affect endothelium permeability to evolve atherosclerosis. Thermal stress analysis demonstrates the relations between temperature heterogeneity of plaque and thermal stress, and between the stress distribution and the inlet pulsatile blood flow, which can contribute to evaluation of plaque instability. This subject focuses on how the thermal heterogeneity affects the permeability of endothelium, and consequently causes the plaque vulnerability and the likelihood of plaque rupture.

The goals of this work are: **(1)** to create tools based on mathematical models that will allow cardiologists to better understand the physical characteristics of the plaque structure and its relationships to AWT, **(2)** to prove the usefulness in evaluating existing or future treatment modalities to predict the vulnerable or instable atherosclerotic plaque, **(3)** to reduce the rate of error from AWT and improve the

ability to identify 'high-risk' patients, and **(4)** to provide a simulation tool that will reduce experimental tests in human or animal models using mathematical simulations.

CHAPTER II

GEOMETRIC MODELS FOR ARTERIES AND PLAQUES

A. System Description

Geometrical irregularity of vessel influences over local temperature distribution as well as blood flow characteristics. One of the objectives of this work is to investigate the effect of arterial geometry on plaque and arterial wall temperature distribution; this study considers several arterial shapes from straight arterial models to bending and bifurcation arteries. In addition, composition and geometry of the atherosclerotic plaque is also varied. The plaque models studied contain a macrophage cell layer that has parametric dimensions varied systematically.

In this study, numerical calculations of temperature distribution at plaque models and arterial wall are performed for different geometries of arterial models and plaque compositions and dimensions. The models and calculations performed will evolve in complexity; we will study idealized 2-D geometric models, which calculate steady state temperature distribution and then transient alterations in AWT by introducing pulsatile blood flow. Finally, simplified and realistic 3-D arterial models will be used to determine temperature distribution in vessel wall and plaques. In 3-D calculations, velocity and temperature profiles calculated are applied to solve structural analysis.

1. Vessel geometries of 2-D and 3-D models

In 2-D model, three different blood vessel geometries are considered: a stenotic straight artery, a bending artery, and an arterial bifurcation with the geometries and dimensions that correspond to the human abdominal aorta, coronary artery, and carotid bifurcation, respectively. The essential geometries and dimensions are illus-

Table I. Geometric parameters of different 2-D vessel types

Vessel Type	Radius (R_i)	length (L_o)	Wall Thickness (d_w)
Straight	3.10	303.8	0.25
Bending	1.765	17.6	0.27
Bifurcation			
Common	3.25	13.83	0.49
Internal	2.175	23.86	0.33
External	1.5	19.95	0.23

where R_i is the radius of the inner-side of vessel, and L_o is the distance along the axis of the vessel which is always perpendicular to the radius. (unit:μm)

trated in Figure 9 and Table I. A central vessel axis perpendicular to the vessel cross section is defined (ℓ), and a cartesian coordinate system (r, ℓ) is laid down at the center of the vessel entrance ($r = 0$, $\ell = 0$). The geometry of straight artery is axi-symmetric, which has a local stenosis simulating the small but high-risk plaque.

The geometry of the straight artery is obtained from the studies in large arteries of Rappitsch and Perktold [45], and Stangeby and Ethier [42]. $L_d = 279\ mm$ of a downstream domain is chosen to minimize the influence of the downstream boundary conditions. The geometry of the bending artery is obtained from an anatomical realistic arterial model of Wada and Karino's study [46] based on a photograph of the human coronary artery used in the flow study of Asakura and Karino [47]. The diameter at the inlet (d_i) and the length along the central axis of the vessel (L_o) were 3.53 and 17.6 mm, respectively. The geometry of bifurcation artery is obtained in the studies of a human carotid artery used by Perktold et al. [48] and Filipovic and Kojic [49]. The essential geometrical parameters are: common, internal and external carotid diameters ($d_i = 6.5\ mm$, $d_{int} = 4.35\ mm$, $d_{ex} = 3\ mm$), maximum carotid

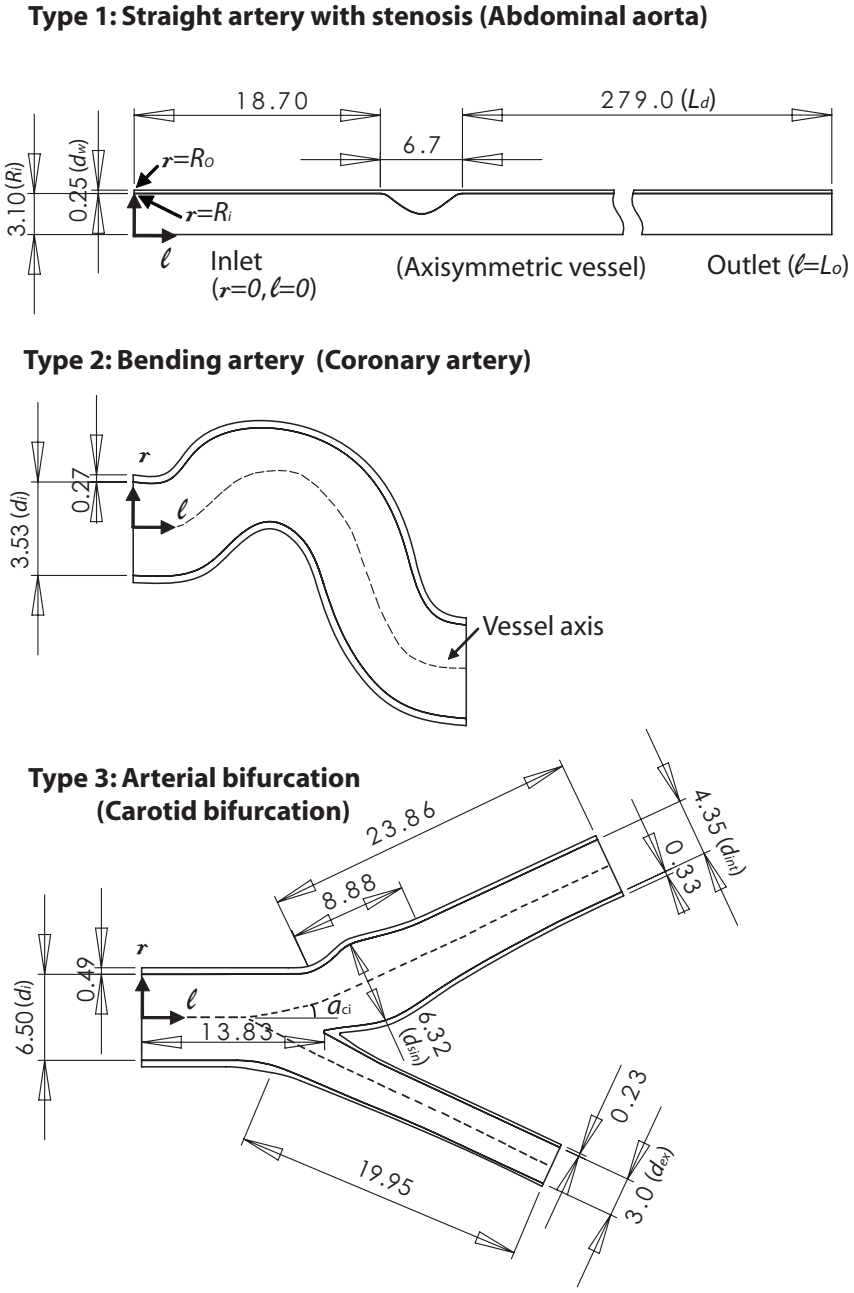

Fig. 9. 2-D vessel geometries considered, and the corresponding geometrical parameters used to describe the vessels. The dimension presented are shown in millimeters.

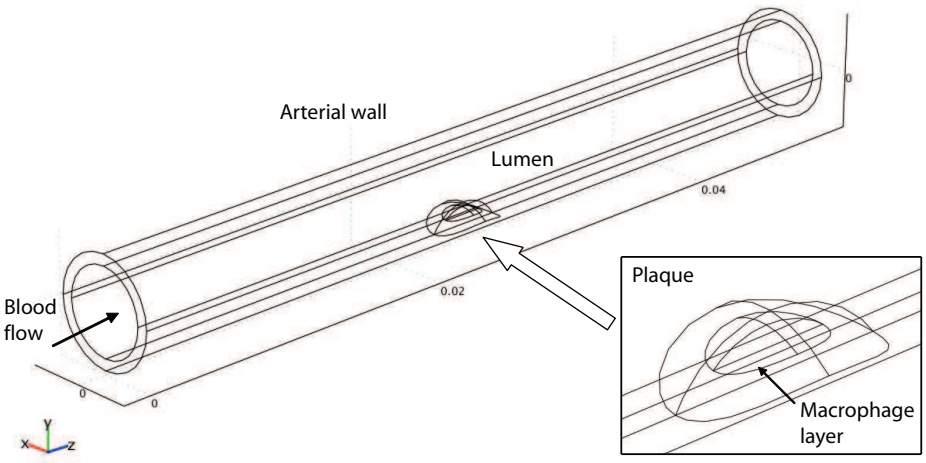

Fig. 10. 3-D simplified geometry of stenotic straight artery consisting of arterial wall, lumen and plaque with macrophage layer. The diameter of the vessel is 6 mm.

sinus diameter ($d_{sin} = 6.32\ mm$), common internal carotid angle ($a_{ci} = 25^o$) and common external carotid angle ($a_{ce} = 25^o$).

The arterial wall thickness of the bending artery is approximately defined by the relationship between vessel diameter (d_i) and wall thickness (d_w), the h/d ratio, which is approximately constant in large arteries [50]. The wall thicknesses (d_w) are 4, 7.6, and 7.5% of the diameters (d_i) of straight, bending, and bifurcation arteries, respectively; these are relatively small, and thus the arterial wall may be modeled as one thin-homogeneous layer. The wall is also assumed to be rigid because the length of the model segment is much smaller than the velocity of the pulse wave propagation [48, 51, 52, 53]. According to comparisons of rigid model and distensible model calculations in human carotid artery analyzed by Perktold and Rappitsch [54], the effect of wall compliance on the flow field and shear stress is about 15% on average. However, the global structure of the flow and stress patterns remains unchanged, and the rigid model is acceptable [54].

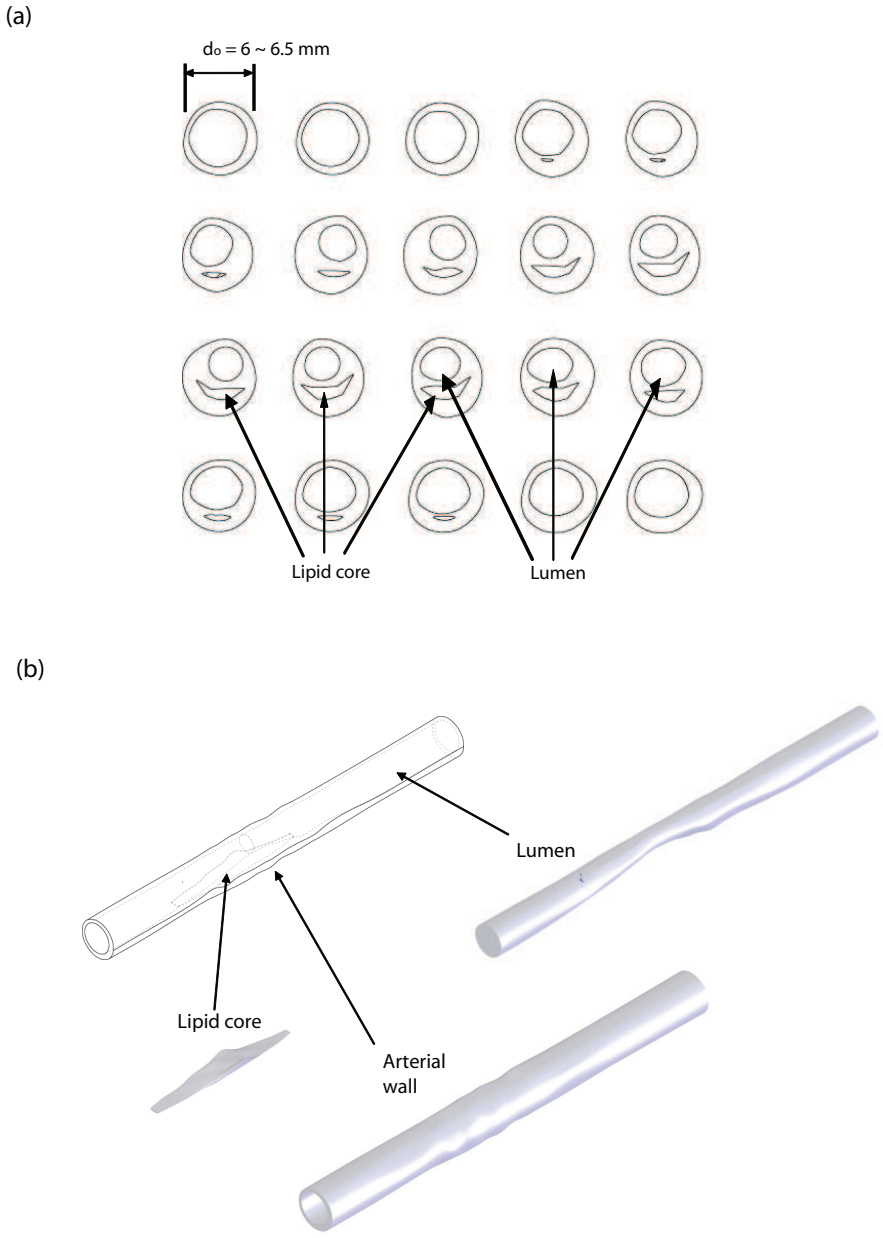

Fig. 11. 3-D realistic geometry of stenotic straight artery consisting of arterial wall, lumen and lipid core. **(a)** 2-D slice CAD images based on 2-D segmented images of human coronary plaque in Tang's study [6]. **(b)** Reconstructed 3-D straight artery where the diameter of the vessel ranges between 6 and 6.5 mm.

The second part of this study considers 3-D simplified and realistic arterial geometries corresponding to an straight artery containing an atherosclerotic plaque. Before the realistic model, the 3-D simplified geometry is created to compare with the results of 2-D calculations. The dimensions and geometry of the 3-D arterial models are similar with these of 2-D straight artery. As shown in Figure 10, the 3-D simplified geometry of stenotic straight artery consists of arterial wall, lumen and plaque containing the macrophage layer. The vessel diameter (d_o) and the length along the central axis of the vessel (L_o) were set to 6 and 50 mm, respectively. The wall thickness of the vessel is 0.6 mm, which may be also relatively small enough to assume as one thin-homogeneous layer.

On the other hand, the 3-D realistic artery geometry was created with 2-D segmented images containing plaque, followed the procedure used in Tang's study [6]. As depicted in 2-D cross-sectional images in Figure 11a, three main regions were considered, corresponding to arterial wall, lumen and lipid core. All the segmented 2-D slices were connected to reconstruct 3-D arterial geometry in CAD software, SolidWorks 2006. For the reconstructed 3-D geometry, all the segmented 2-D slices were connected with $LOFT$ command to produce the smooth surface of the artery as shown in Figure 11b. The 3-D geometry saved in IGES format was imported into COMSOL software to accomplish the mesh generation. The 20 2-D slice set having 1 mm intervals between two slices is 22 mm long in the longitudinal direction. The diameter of the vessel ranges between 6 and 6.5 mm. The vessel was extended uniformly at inlet and outlet by 16 and 30mm so that it became long enough to obtain a fully developed flow profile at the inlet and outlet of the vessel.

2. Plaque composition, size, distribution and location

The vulnerable plaque is based on the following experimental observations: **(1)** Macrophages or inflammatory cells are responsible for the hot spots and forms a thin layer embedded in plaque. Hot spots in atherosclerotic plaque are formed as macrophages in lesions become active. **(2)** Plaque has thin cap with large lipid core (regularly, plaques have a cap thickness of $< 100\ \mu m$ and a lipid core that accounts for $> 40\%$ of plaque's total area (volume)) [55]. **(3)** Size of active plaque is generally small, and flow instabilities, such as flow separation and vorticity downstream of the stenosis, are not easily observed with MRI or other contrast agent methods [18]. **(4)** Temperature change in vulnerable plaque is correlated to macrophage density and the depth from plaque surface at which layer of macrophages are located [4, 56]. **(5)** Vulnerable plaque showing thermal inhomogeneities of 0.4 to 2.2 ^oC has a thickness of 400 μm and a macrophage rich layer of between 15 and 40 μm thick [14].

Based on the plaque characteristics just described, plaque thickness (d_p), macrophage rich layer thickness (d_{mp}), fibrous cap thickness (l_f), plaque extension (l_p), macrophage extension (l_{mp}), wall thickness (d_w) are defined in Figure 12, where a longitudinal cut of an atherosclerotic blood vessel containing a layer of macrophages is shown for 2-D model.

The plaque is located over the arterial wall, and its thickness (d_p) is chosen to be $d_p = \alpha d_w$, where $\alpha = 1, 2$; these values of α represent the case of plaques that produce small occlusions occurring no flow instability in flows. d_{mp} is the macrophage rich layer thickness which is set to 25, 50 and 100 μm. d_{mp} is studied to analyze the relationship between the thickness macrophage layer and plaque temperature variation. l_f is the distance between the vessel lumen and the macrophage layer and physically represents the thickness of the fibrous cap; for the calculations, l_f is set to 50 and 100 μm, these

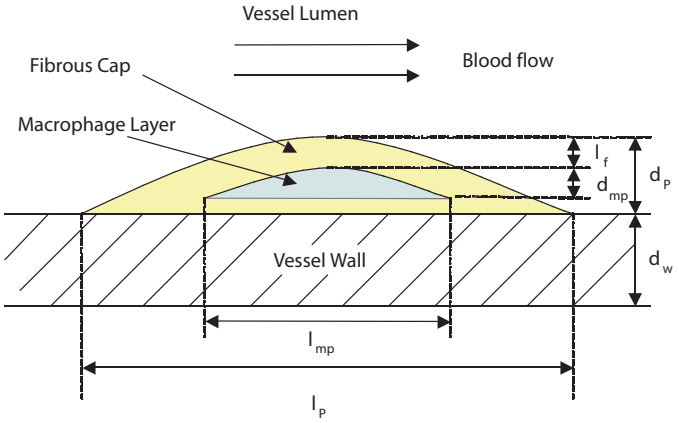

Fig. 12. Plaque geometry and dimensions. d_w is the arterial wall thickness, d_p the plaque thickness, d_{mp} the macrophage rich layer thickness, and l_f the thickness of the fibrous cap. l_p and l_{mp} represent the extension or length of the plaque and the macrophage layer in the longitudinal direction, respectively.

values will serve to analyze the effect on the plaque temperature gradient when the heat source is at different depths. Finally, l_p and l_{mp} denote the extension of the plaque and macrophage layer in the longitudinal direction of the vessel, respectively. The plaque is located in the regions that correspond to the lowest wall shear stress, and l_p is extended to cover these regions in each one of the vessel types considered. The dimension l_{mp} is given by $l_{mp} = \beta l_p$, where $\beta = 0.5$ and 0.25; these values of β were selected from experiments showing high macrophage concentration at the center of the lesion [57]. The plaque geometries and dimensions applied for the variables in 2-D modeling are presented in Table II.

In the 3-D simplified model shown in Figure 10, the plaque is also located over the arterial wall with a dome shape, which has the plaque thickness (d_p) of $1,200$ μm and extensions of $2,000$ μm in the cross-sectional plane (x-axis) and $3,500$ μm in the ℓ-axis, respectively. The macrophage layer with a cone shape is embedded inside

Table II. 2D Plaque geometry and dimensions

Vessel Type	Plaque length (l_p)	Wall thickness (d_w)	Macrophage length (l_{mp})	Plaque thickness (d_p)	Fibrous cap thickness (l_f)	Macrophage thickness (d_{mp})
Straight	6,670	250	1,668	250	50	25
			3,335	500	100	50
				750		100
Bending	3,000	270	1,500	540	50	25
					100	50
						100
Bifurcation	3,000	335	1,500	670	50	25
					100	50
					150	100

unit:(μm)

the plaque; as before, the distance between plaque/lumen surface and location of the macrophage layer is referred as the thickness of the fibrous cap (l_f), and is set to 200 μm. The macrophage layer has a layer thickness (d_{mp}) of 100 μm and extends 800 μm in the cross-sectional plane (x-axis) and $1,700$ μm in the ℓ-axis (l_{mp}), respectively. In the 3-D realistic model of Figure 11, the macrophage layer is assumed to be located inside the lipid core, which is directly embedded in the arterial wall. It has the maximum plaque extensions (l_{mp}) of 5 mm in the cross-sectional (x-axis) and 24 mm in the ℓ-axis, respectively.

3. Blood flow and Fluid-Structure Interaction

Blood flow is assumed to be an incompressible, homogeneous and Newtonian flow, which is acceptable in large arteries where relatively high shear rates occur [48, 51, 58]. It was reported that, although blood exhibits non-Newtonian behavior in small

branches and capillaries, Newtonian assumption of blood is adequate for blood flow in vessels with diameter $> 100\ \mu m$ [48, 52, 53, 59], and also accepted that blood behaves as a Newtonian fluid at shear rates above 100 s^{-1} [59]. The study of Perktold et al. [48] showed that an average difference between Newtonian and non-Newtonian wall shear stress is about 10% in a model carotid artery bifurcation. Blood exhibits non-Newtonian behavior in small branches and capillaries and, in most arteries, blood behaves in a Newtonian fashion with a constant viscosity of 4 centipoise [53]. In our calculations, Fluid-Structure Interaction (FSI) is neglected, based on the studies [60, 61, 62] where neglecting the elastic nature of the arterial wall incurs an error of approximately 10% in the velocity profiles. In addition, the presence of a water transmural flow inside the arterial wall is neglected in the calculations because it is very small in comparison to the blood flow in the luminal region.

B. Summary of Calculations

1. Solution method

In this study, commercially available multi-physics software package COMSOL Multiphysics version 3.3 (COMSOL, Inc., SWEDEN) is used for modeling and solving coupled and uncoupled physics problems of the blood flow, heat transfer and structural fields. The software provides the finite element method to solve partial differential equations (PDEs) which is especially appropriate for the discretization of irregular geometries because of its high flexibility.

For functions of the variables, Piecewise Cubic interpolation method was used using a piecewise cubic Hermite polynomial with continuous first derivatives. When arguments fall outside the grid, extrapolation method selected evaluates the polynomial from the closest grid point at the actual point where a value is required. As

the element shape function, Lagrange element of second order called the quadratic element was used to represent the nature of the solution within each element. Using the time-dependent solver to find the solution to nonlinear unsteady problems, the relative and absolute tolerances of 0.01 and 0.001, respectively, were entered to control the error in each integration step. To control how the solver takes its internal time steps, the Free option was selected for the solver to its time steps arbitrarily. The Assembly block size of 5,000 decides the number of mesh elements to process together during the assembly process. For the solution form, Weak form is used to convert all the equations and boundary conditions into the solution form with one large system of PDEs and boundary conditions before solving it. The weak form is the best to obtain a correct Jacobian Matrix and the assembly in the weak form is faster than other forms such as general and coefficient forms.

The FEM discretization of the time-dependent PDE problem produces a system of ordinary differential equations (ODE) or differential algebraic equations (DAE); COMSOL uses a version of the DAE solver DASPK. To solve the DAE (Differential-Algebraic Equation) system, COMSOL codes uses variable-order variable-stepsize backward differentiation formulas (BDF). COMSOL solvers break down each problems into the solution of several linear systems of equations. Therefore, the solver considering the solution time and memory requirements should be chosen between direct and iterative solvers for linear systems. In our study, UMFPACK direct solver was employed for 2-D calculations, and SPOOLES direct solver was worked for 3-D calculations for using less memory than UMPACK. These direct solvers solve a linear system by Gaussian elimination which is stable and reliable process. The solvers also work on general systems of the form $Ax = b$ using the multifrontal method and direct LU factorization of the sparse matrix A, where L and U are the lower and upper triangular matrices, respectively, in $A = LU$ for a linear system of equations.

2. Mesh generation and grid independence

In the domain, unstructured mesh consisting of triangular and tetrahedral elements was generated for 2-D and 3-D geometries, respectively. The grid distribution was non-uniform to allow a finer grid near the regions of thin plaque cap and macrophage layer with sharp angles to get better resolution and handle the larger velocity and temperature variations. The average numbers of triangular elements used for 2-D geometries were 34,000 for straight artery, 28,000 for bending artery, and 25,000 for bifurcation artery. In 3-D, the numbers of tetrahedral elements were 20,000 and 41,000 for simplified and realistic geometries, respectively.

The number of elements used for the mesh is increased systematically to check for mesh independence; the mesh refinement is stopped when the maximum relative difference for the calculated parameter P for the different meshes satisfied the following condition

$$\frac{P_{fine} - P_{coarse}}{P_{fine}} \leq 0.1\%$$

where the mesh independency was verified under the steady solution of $Re = 300$. The finer meshes were 70,000, 50,000 and 50,000 elements for straight, bending and bifurcation arteries, respectively. Particularly, the maximum difference in the calculated temperature is 0.035% for the straight artery, 0.003% for the bending artery and 0.1% for the arterial bifurcation.

3. Convergence verification

In addition to a grid independence analysis, a convergence verification is performed for the initial condition of the transient calculation; this is needed to verify that the initial temperature used in the calculations corresponds to a stable temperature distribution.

The calculations using the steady state temperature distribution are calculated using a velocity equal to the time-average velocity during one cardiac cycle. Calculations are extended for several cycles using the waveform functions as the inlet velocity condition; the number of cycles is selected to ensure that the temperature at several points along the plaque/lumen interface do not vary considerably between two consecutive cycles.

For 2-D unsteady blood flow case, 6 cycles acceptable to run for the transient computations; the difference in the temperature distribution between the fifth and sixth cycles is 0.87 for the straight artery, 1.08 for the bending artery and 0.96% for the arterial bifurcation, respectively.

For the case of blood flow reduction, the steady state temperature distribution was firstly calculated corresponding to the time-average velocity of the normal cardiac cycles *Cycle 1* through *3* in each artery. Once the convergence verification for the initial condition was performed, calculations were extended for 3 more normal cardiac cycles using normal values for the inlet waveform (this corresponded to stage 1 of the calculation); then blood flow was partially reduced to 50% during one cycle (*Cycle 4*), and finally, during the last stage of the calculation, the blood flow was drastically reduced to 5% for eight more cycles. It was noted that, after the flow reduction in stage 3, the temperature distribution arrives to a steady state within less than three cycles. 6 cycles was found to be sufficient to ensure that the temperature at several points along the plaque/lumen interface vary less than 1% between two consecutive cycles.

CHAPTER III

DETERMINATION OF PLAQUE TEMPERATURE UNDER DIFFERENT CONDITIONS

Arterial wall temperature (AWT) and thermal stress at plaque/lumen surface are analyzed in 2-D arterial geometries (straight, bending and arterial bifurcation) and 3-D arterial (straight) model. Table III presents the overall procedures for this study.

In 2-D model, three different blood flow cases are considered: steady-state, transient state and blood flow reduction. In order to determine plaque locations in each arterial case, wall shear stress (WSS) is calculated for steady-state blood flow. The steady calculations serve as the initial conditions for the transient case, where calculations are performed under the pulsatile inlet blood flows. Temperature distributions are calculated at plaque/lumen surface of three arterial geometries. To analyze the convective cooling effect of the blood flow, the case of blood flow reduction during the introduction of a catheter is simulated by gradual reduction of the inlet pulsatile flow. In 3-D model, thermal stresses at the plaque surface are investigated using temperature distributions in transient case of a stenotic straight artery as it may become one of important factors influencing over plaque revolution and rupture.

A. 2-D Steady Blood Flow Calculations

1. Blood flow analysis

In 2-D steady state calculations, the blood flow in the arteries is governed by Navier-Stokes equations and continuity equation for an incompressible fluid given by

$$\rho\left(\mathbf{v}\cdot\nabla\mathbf{v}\right)=-\nabla P+\mu\nabla^{2}\mathbf{v}, \tag{3.1}$$

Table III. Procedures of numerical calculations

Model type	Calculations	Objectives	Inlet cond.	Arterial geometries
2-D Steady	Wall shear stress (WSS)	- find the most rupturable region corresponding to lower WSS region	Re = 300 & 500	- Straight artery, - Bending artery - Arterial bifurcation
2-D Steady	Velocity & Temperature	- determine AWT at plaque surface - find the important factors affecting AWT - define relation between AWT and the factors	Re = 300 & 500	- Straight artery, - Bending artery - Arterial bifurcation
2-D Transient	Velocity & Temperature	- observe AWT during cardiac cycles - obtain temperature history at representative points of plaque surface	Waveform function	- Straight artery, - Bending artery - Arterial bifurcation
2-D Occlusion blood flow	Velocity & Temperature	- investigate cooling effect of blood flow - observe AWT increase by reducing blood flow	Reduced blood flow during cardiac cycles	- Straight artery, - Bending artery
3-D transient	Velocity, Temperature & Thermal stress	- determine AWT at plaque surface - calculate thermal stress by temperature chage	Waveform function	- Straight artery (Simplified & Realistic geometries)

$$\nabla \cdot \mathbf{v} = \mathbf{0}, \tag{3.2}$$

where $\mathbf{v}$ is the velocity of blood flow, P the blood pressure, ρ the density of blood and μ the viscosity of blood. The boundary conditions required to solve the governing equations (3.1) - (3.12) are as follows. In Figure 9, the velocity u at the inlet has a parabolic profile given by,

$$u = 2u_o \left(1 - \left(\frac{r}{R_i}\right)^2\right), \quad v = 0 \quad \text{at} \quad \ell = 0, \tag{3.3}$$

where r is the radial distance from the center of vessel and R_i is the radius of the inner-side of the vessel. Reynolds numbers of inlet flow, defined with the mean velocity u_o and the radius of the vessel R_i, are 300 and 500 to present minimum and maximum values, respectively, of normal pulsatile blood flow, where $Re = 2u_oR_i/\mu$.

At the outlet, a fully developed flow is assumed on the velocity. No-slip conditions are imposed at the arterial walls. Especially, an axi-symmetric condition is used at

the centerline of straight artery.

$$P = 0 \quad \text{at} \quad \ell = L_o, \tag{3.4}$$

$$u = 0, \quad v = 0 \quad \text{at} \quad r = R_i. \tag{3.5}$$

$$\frac{\partial u}{\partial r} = 0, \quad v = 0 \quad \text{at} \quad r = 0. \tag{3.6}$$

where u and v represent the velocity components. r is the radial distance from the center of the vessel, R_i is the entrance radius of the inner-side of the vessel, $\ell = L_o$ denotes the outlet of the vessel, and $r = 0$ indicates the center of the vessel.

2. Thermal analysis

Given the fact that plaque vulnerability is related to temperature inhomogeneities within the arterial wall of an atherosclerotic artery, the temperature field in a blood vessel is calculated by solving the energy equation. To study the thermal effect of plaque, the artery is modeled as a vessel with variable wall thickness, which contains a region of macrophage layer producing metabolic heat activation. In this system, heat convection due to the luminal blood flow and heat conduction through the vessel walls are considered. The steady state energy equation is

$$\rho_i C_{pi} \left(\mathbf{v} \cdot \nabla T_i\right) - \nabla \cdot \left(k_i \nabla T_i\right) = \dot{q}_{mi} \tag{3.7}$$

where i refers to blood (i=1), arterial wall (i=2), plaque (i=3) and macrophage layer (i=4). T_i represents the temperature, $\mathbf{v}$ the velocity of blood in the lumen region, k_i the thermal conductivity, ρ_i the density, and C_{Pi} the specific heat. The thermophysical parameters used in equations 3.1 and 3.7 are taken from the literature

Table IV. Thermophysical parameters of blood, arterial wall, plaque tissue and macrophage layer

	Blood	Arterial wall	Plaque	Macrophage layer
k_i (W/m^oC)	0.549	0.476	0.484	0.484
ρ_i (kg/m^3)	1050	1075	920	920
Cp_i (J/kg^oC)	4390	3490	4080	4080
μ_i $(Pa \cdot s)$	0.0033			

These parameters where taken from [63, 64, 65].

[63, 64, 65] and are given in Table IV; it is assumed that the different layers in the vessel wall (intima, media and adventitia) have the same thermal properties and that the macrophage layer and the plaque have the same values of thermal conductivity and heat capacity.

The term $\dot{q}_{mi}$ in equation 3.7 represents the metabolic heat produced by the tissue (i=1, 2 and 3), and is significant for the macrophage layer only (i=4), as it accounts for the local inflammatory reaction observed in the vulnerable plaque. The metabolic heat released by the inflamed plaque is a direct function of plaque composition and the developmental stage of the lesion. Macrophages are involved in all evolutionary stages of the lesion, but their activation and subsequent metabolic heat production varies in each stage. For the calculations, the heat generation of the macrophage layer has three different values corresponding to $\dot{q}_m = 0.05,\ 0.1$ and $0.2\ W/mm^3$; the different values of q_m account for the heat produced by macrophages at different activation stages. These values were chosen to reproduce the magnitude of the temperature gradients reported in vulnerable atherosclerotic plaques (0.4 to 2.2 ^oC) [12, 14, 15]. The values of $\dot{q}_m$ for the tissue containing macrophages are approximated from the following expression

$$\dot{q}_m \left[\frac{W}{mm^3}\right] = \frac{q_{cell}}{V_{cell}}, \tag{3.8}$$

where V_{cell} is a volume of a macrophage cell and q_{cell} is a heat produced by a single cell. There are no reports of q_{cell} for active macrophages in atherosclerotic plaques. For the determination of the heat generation $\dot{q}_m$ in plaque tissue, q_{cell}, expressed in W, is defined as heat generation per macrophage cell. The volume of a macrophage cell can be approximately obtained by the figure of Ross and Auger's study [66]. Alveolar macrophages produce around 20 $pW/cell$ and other cells with high metabolic activity, such as hepatocytes, produce 300 $pW/cell$ [67]. Assuming that macrophages have a volume of 30 to 60 μm^3 and $q_{cell} = 10^3$ $pW/cell$, the approximated metabolic heat is between 0.016 and 0.03 W/mm^3. It is convenient to note that cell volume and metabolic activity vary depending on cellular activation.

As shown in Figure 9, at the external vessel wall ($r = R_o$), the boundary conditions correspond to constant arterial or core body temperature (T_a), which is justified by the fact that vessel wall is well perfused by the *vasa vasorum* [1].

$$T = T_a, \text{ at } \mathrm{r} = \mathrm{R_o}, \tag{3.9}$$

The constant blood and tissue temperature are assumed at the entrance of the vessel ($\ell = 0$).

$$T = T_a, \text{ at } \ell = 0, \tag{3.10}$$

No blood and tissue temperature gradient is at the vessel outlet ($\ell = L_o$) to represent how blood flow removes heat from the vessel wall by convection.

[1] Small nutrient blood vessels which supply the walls of large arteries or veins.

$$\frac{\partial T}{\partial \ell} = 0, \text{ at } \ell = \mathrm{L_o}. \tag{3.11}$$

where T_a is a constant that represents the arterial or core temperature and was assigned a value of 37.5 ^oC. Finally, continuity of heat flux and temperature at the lumen-plaque interface, the plaque-vessel wall interface and the plaque-macrophage layer interface is assumed.

3. Plaque localization by low wall shear stress

It has been observed that atherosclerotic lesions are localized at the regions of low and oscillatory wall shear stress [1, 24, 26]. This occurs when the local mass transport of large sized atherogenic molecules is dominated by blood flow convection. In this section, wall shear stress (WSS) of stenotic straight artery is calculated to validate with the results of other studies [26, 45, 68] under steady blood flow condition. After the validation, the atherosclerotic plaques are set up in the regions showing the lowest wall shear stress through arterial walls of a bending artery and arterial bifurcation.

a. Validation of plaque location in straight artery

A stenotic straight artery has a local constriction where the plaque is positioned. The geometric parameters used are matched to a human abdominal aorta. The size of plaque is small enough to cause less flow momentum, which no flow separation is occurred at the plaque region. As a result of calculations, Figure 13 illustrates that WSS is peaked at the local constriction region having the highest velocity of blood flow. The peak magnitude of WSS are 7.9 and 16.3 Nu/m^2 for Reynolds numbers of 300 and 500, respectively. The lowest values of WSS at the rear region of the plaque are -0.7 and -1.3 Nu/m^2 in Reynolds numbers of 300 and 500, respectively.

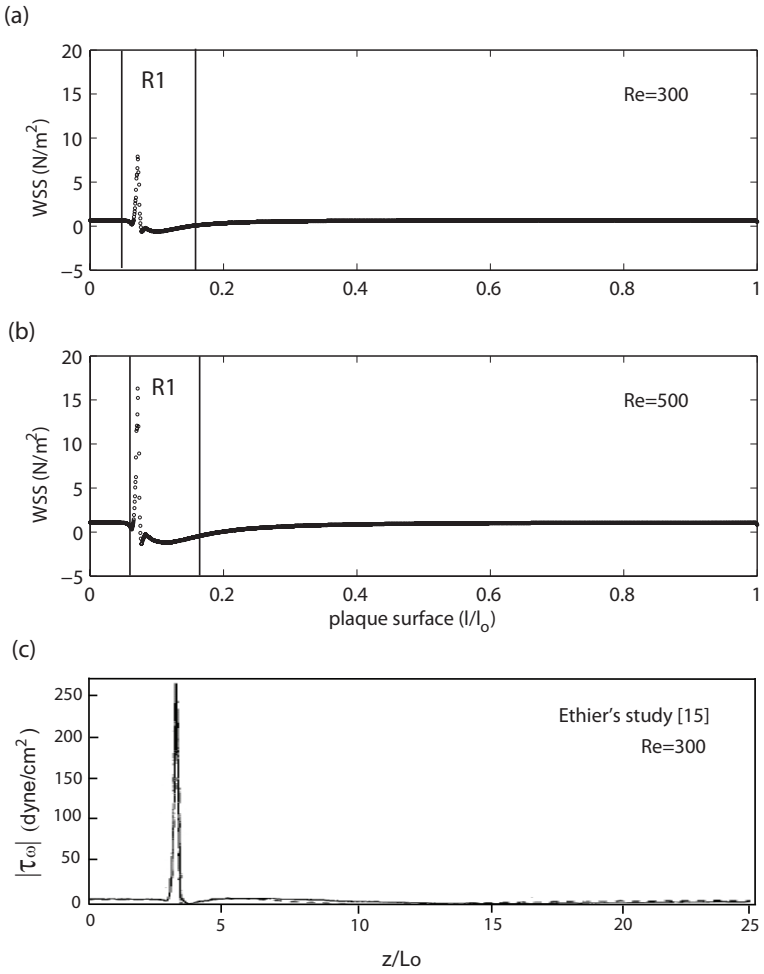

Fig. 13. The comparison of the computed values for **(a)** $Re = 300$, **(b)** $Re = 500$ and **(c)** reference values with a 75% area-reduction plaque at $Re = 300$ (Ethier [26] and Rappitsch [45, 68]), which were calculated in a stenotic straight artery.

Comparing to the studies of Ethier [26] and Rappitsch [45, 68] in Figure 13c, the WSS is qualitatively similar on the pattern of sudden increasing and decreasing between 0 and 270 $dyne/m^2$ of Re = 300 at the contraction and expansion regions of a plaque. The quantitative difference of the values is subject to the different geometry of plaque applied; their stenosis models [26, 45, 68] produced a 75% area-reduction of lumen.

b. Bending and bifurcation arteries

According to direct measurements and other computational models of WSS [25, 32, 69], the most susceptible regions of atherosclerotic plaque are on the order of ± 4 Nu/m^2. Hence, the plaques in bending and bifurcation arteries could be positioned at the lower WSS regions, which is under the order of ± 4 Nu/m^2. Figure 14 shows the characteristics of WSS at $Re = 300$ and 500 at the lower wall in bending artery and the outer ECA in arterial bifurcation. In bending artery, the minimum shear stress is occurred at the region $R1$ ($l/l_p = 0.45$ to 0.52) and the region $R2$ ($l/l_p = 0.82$ to 0.95) in Figure 14a. The sharp rise of WSS at the first bend along lower arterial wall presents the momentum of a blood flow. For bending artery, the region $R1$ is selected to locate the plaque. For arterial bifurcation in Figure 14b, the minimum WSS to locate the plaque is occurred on $R1$ ($l/l_p = 0.4$ to 0.55). Based on the computed WSS, the plaques are positioned at the sites of the lowest WSS in each artery as shown in Figure 15.

4. Results of 2-D steady blood flow

In this section, the temperature distribution along the plaque/lumen interface will be analyzed to investigate what factors mainly contribute to temperature inhomogeneity through varying the following parameters; **(1)** metabolic heat generation produced by inflammatory cells in macrophage layer ($\dot{q}_m$), **(2)** thickness and extension of

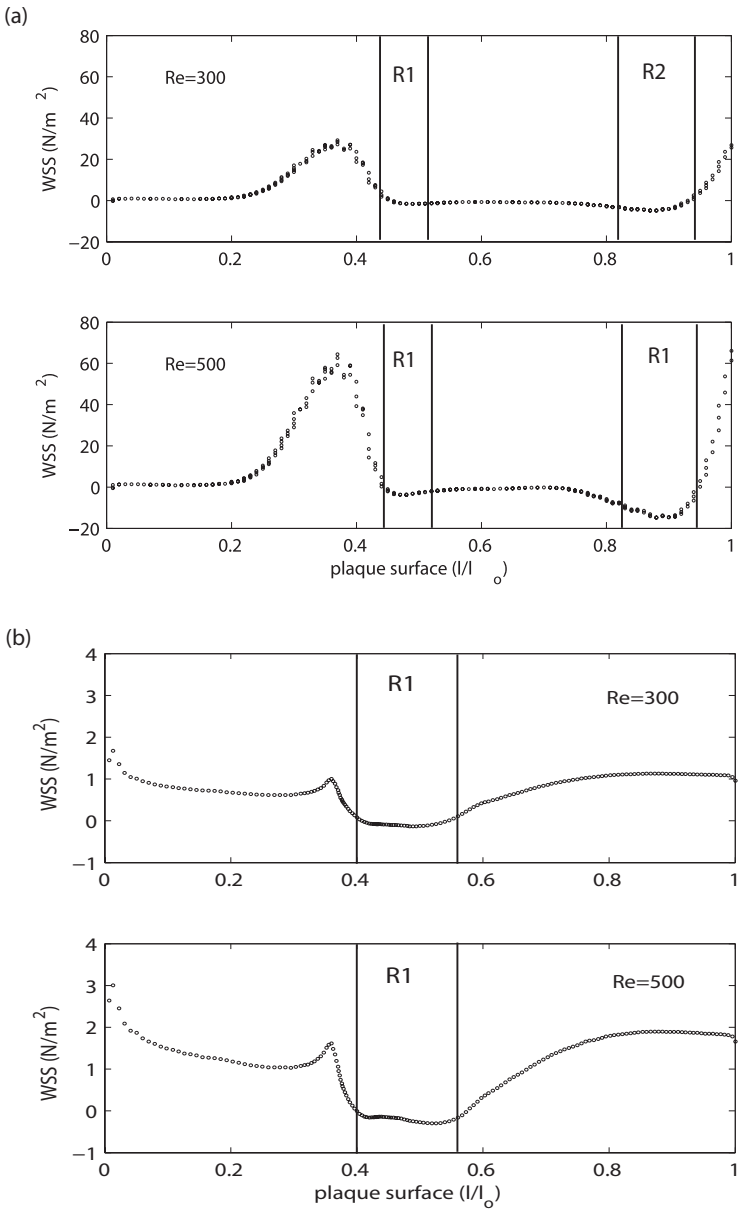

Fig. 14. The computed wall shear stresses of $Re = 300$ and 500 in arteries. **(a)** At the lower wall of bending artery, the minimum WSS occurs between $l/l_p = 0.45$ and 0.52 at $(R1)$ and between $l/l_p = 0.82$ and 0.95 at $(R2)$. **(b)** At the outer ECA of arterial bifurcation where the lower WSS is usually occurred, the minimum WSS is computed at $R1$ ($l/l_p = 0.4$ to 0.55). The higher shear stress regions where the blood flow velocity is higher are less susceptible regions.

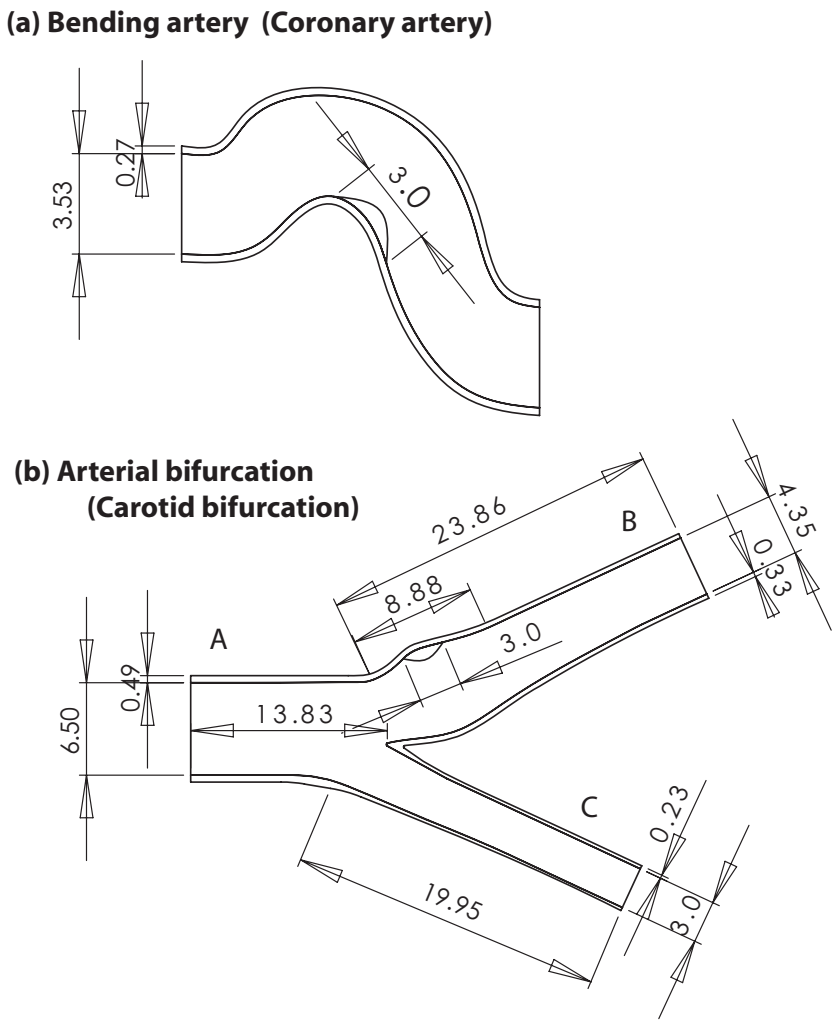

Fig. 15. The plaque locations of **(a)** a bending artery and **(b)** an arterial bifurcation in terms of the computed lowest WSS

macrophage layer (d_{mp} and l_{mp}), **(3)** depth at which macrophage layer is embedded (l_f), and **(4)** size of plaque ($d_p = \alpha d_w$). As the results of the parametric study, the maximum temperature changes $\Delta T_{max} = (T_{max} - T_a)$ at the interface of plaque/lumen surface are presented in Table V. In addition, the flow instabilities occurred at each artery will be discussed because the temperature distribution is also affected by the flow characteristics.

a. Variation of $\dot{q}_m$

As the first variable parameter, the metabolic heat generation $\dot{q}_m$ is varied to investigate the effect of the inflammatory cell density, which takes the values of 0.05, 0.1 and 0.2 W/mm^3. Figure 16 indicates how the temperature along the plaque/lumen interface is varied with the metabolic heat ($\dot{q}_m$) in the macrophage layer. These figures present the temperature change $\Delta T = (T - T_a)$ of straight, bending artery and bifurcation artery at $Re = 300$ and 500.

In Figure 16a, ΔT_{max} of the straight artery ($Re = 300$) is registered at 0.26 ^oC for $\dot{q}_m = 0.05$ and 1.03 ^oC for 0.2 W/mm^3, respectively. The maximum temperature ΔT_{max} occurs at the downstream edge of the plaque because the blood flow forces temperature distribution to further downstream with convection effect.

For bending artery as shown in Figure 16b, ΔT_{max} at $Re = 300$ are 0.21 and 0.82 ^oC for $\dot{q}_m = 0.05$ and 0.2 W/mm^3, respectively. ΔT has the lower increase compared to the straight artery because the cooling effect by blood flow momentum is stronger at the plaque upstream, which contributes to the transport of thermal energy from the plaque surface to the blood flow. Compared to the temperature change of straight arterial case, ΔT_{max} occurs closer to the center of plaque where the boundary layer encounters a separation point. The temperature is relatively higher at the rear of plaque where the convective cooling effect from plaque surface is weaken

Table V. Maximum temperature changes (ΔT_{max}) at the plaque surfaces of the different vessel types for steady-state calculations

Variation of Parameters	Straight Re300	Straight Re500	Bending Re300	Bending Re500	Bifurcation Re300	Bifurcation Re500
$\dot{q}_m$ (W/mm^3)						
0.05	0.26	0.22	0.21	0.17	0.37	0.40
0.1	0.52	0.45	0.41	0.35	0.75	0.81
0.2	1.03	0.90	0.82	0.69	1.50	1.62
						(From Figure 16)
d_{mp} (μm)						
25	0.52	0.45	0.41	0.35	0.75	0.81
50	1.00	0.87	0.80	0.67	1.47	1.59
100	1.87	1.62	1.53	1.3	2.84	3.08
						(From Figure 17)
l_f (μm)						
50	0.52	0.45	0.41	0.35	0.75	0.82
100	0.45	0.39	0.37	0.31	0.70	0.76
150	N/A	N/A	N/A	N/A	0.65	0.71
						(From Figure 19)
d_p (μm)						
250	0.52	0.45	N/A	N/A	N/A	N/A
500	0.55	0.47	N/A	N/A	N/A	N/A
						(From Figure 21)
l_{mp} (μm)						
1,667	0.68	0.58	N/A	N/A	N/A	N/A
3,335	0.88	0.76	N/A	N/A	N/A	N/A
						(From Figure 22)

(unit: ^oC)

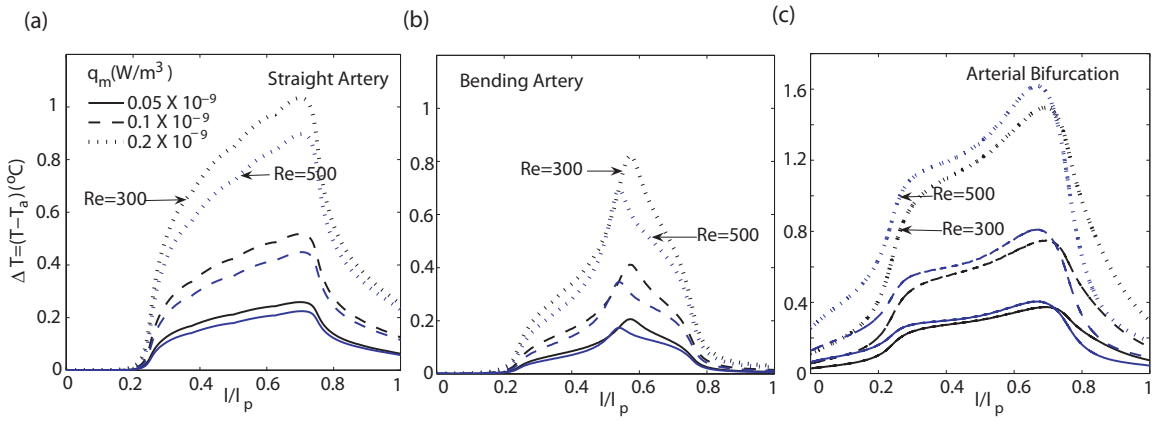

Fig. 16. Temperature change at the plaque/lumen interface produced by variations of $\dot{q}_m$ in **(a)** straight artery with $l_{mp} = 3,335$, $d_{mp} = 25$, $d_p = 250$, and $l_f = 50$ μm, **(b)** bending with $l_{mp} = 1,500$, $d_{mp} = 25$, $d_p = 540$, and $l_f = 50$ μm, and **(c)** bifurcation with $l_{mp} = 1,500$, $d_{mp} = 25$, $d_p = 670$, and $l_f = 50$ μm. The black lines correspond to $Re = 300$ and the gray lines represent $Re = 500$.

by the flow separation.

In the arterial bifurcation (Figure 16c), ΔT_{max} at $Re = 300$ registers 0.37 and 1.62 ^oC for $\dot{q}_m = 0.05$ and 0.2 W/mm^3, respectively. ΔT_{max} occurs relatively closer to the right edge of the plaque. Comparing ΔT at $Re = 300$ and 500, the higher velocity ($Re = 500$) records higher temperature with the lower cooling effect of blood flow due to the flow circulation. In arterial bifurcation, flow circulation is observed at the outer wall of ECA, which affects the temperature distribution. The flow circulation is determined by velocity of blood flow, which is depicted in Figure 24. The details about quantifying the effect of flow circulation over the temperature variation will be discussed in the following subsection of *Flow instabilities due to arterial geometries*.

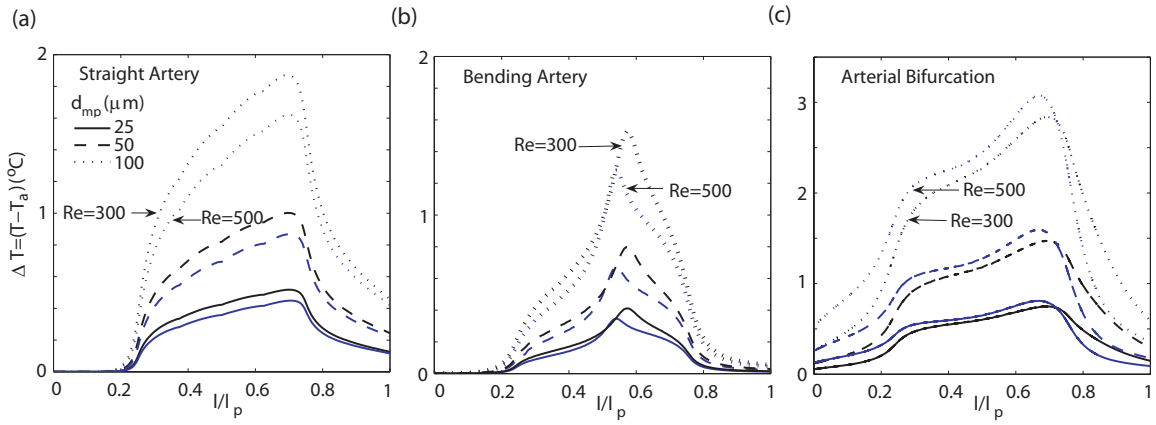

Fig. 17. Temperature change at the plaque/lumen interface produced by variations of d_{mp} at $\dot{q}_m = 0.1\ W/mm^3$. The results correspond to **(a)** straight artery with $l_{mp} = 3,335$, $d_p = 500$, and $l_f = 50\ \mu m$, **(b)** bending artery with $l_{mp} = 1,500$, $d_p = 540$, and $l_f = 50\ \mu m$, and **(c)** arteria bifurcation with $l_{mp} = 1.500$, $d_p = 670$, and $l_f = 50\ \mu m$. The black lines correspond to $Re = 300$ and the gray lines represent $Re = 500$.

b. Variation of d_{mp}

The macrophage layer thickness d_p is varied to investigate the effect of the macrophage layer size, which were 25, 50 and 100 μm. As shown in Figure 17 and Table V, ΔT_{max} for $d_{mp} = 25$ and 100 μm at $Re = 300$ is varied between 0.52 and 1.87 ^oC in straight artery, 0.41 and 1.53 ^oC in bending artery, and 0.75 and 2.84 ^oC in arterial bifurcation, respectively. At $Re = 300$ and 500, increasing d_{mp} of 100% produces the increasing ratio of ΔT_{max} to 92 and 87% for straight, 95 and 91% for bending, and 96 and 93% for arterial bifurcation, respectively. As the result, ΔT_{max} increases proportionally to the macrophage layer thickness d_{mp} with a linear relationship, observed in the experimental studies [12, 15]. The slopes are presented in Table VI, which depends on the arterial geometry as well as other plaque parameters.

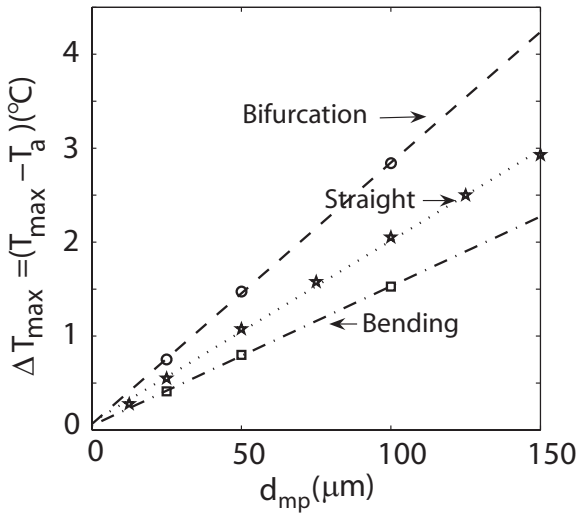

Fig. 18. Maximum temperature change ΔT_{max} at the plaque/lumen interface produced by variations in the macrophage layer thickness d_{mp}. The linear relationships are fitted in the line $\Delta T_{max} = b + m d_{mp}$, where values for the constants b and m are given in Table VI for each vessel geometry. These calculations correspond to $\dot{q}_m = 0.1\ W/mm^3$, $l_f = 50$, $d_p = 500$ (straight), 540 (bending), and 670 μm (bifurcation) at $Re = 300$.

Table VI. Values of slope (m) and intercept (b) in Figure 18 where the relations of $\Delta T_{max} = b + m d_{mp}$ are shown.

Vessel Type	m	b	r
Straight	0.0193	0.0819	0.9992
Bending	0.0148	0.0476	0.9999
Bifurcation	0.0278	0.0641	0.9999

These calculations correspond to the following parameters: $\dot{q}_m = 0.1\ W/mm^3$, $l_f = 50\ \mu m$, $Re = 300$, and $d_p = 500$ (straight), 540 (bending), 670 $(bifurcation)\ \mu m$.

Table VII. Values of slope (m) and intercept (b) for Figure 20 where the lines $\Delta T_{max} = b + ml_f$ are shown.

Vessel Type	m	b	r
Straight	-0.0019	1.1722	0.9999
Bending	-0.0008	04495	1.0000
Bifurcation	-0.0012	0.7521	0.9999

These calculations correspond to the following parameters: $\dot{q}_m = 0.1\ W/mm^3$, $d_{mp} = 50\ \mu m$, $Re = 300$ and and $d_p =$ 500 (straight), 540 (bending), 670 $(bifurcation)\ \mu m$.

c. Variation of l_f

The distance l_f between the macrophage layer and the plaque/lumen interface is also one of the important parameters affecting the plaque temperature distribution. The effect of variations of l_f referred as fibrous cap thickness is shown in Figure 19 for the cases of the straight, bending and arterial bifurcation. Table V presents that the maximum ΔT_{max} for $l_f = 50$ and 100 μm at $Re = 300$ is between 0.52 and 0.45 ^oC in the straight artery, 0.41 and 0.37 ^oC for bending artery, and 0.75 and 0.7 ^oC for arterial bifurcation, respectively.

It is observed that ΔT_{max} is decreased as the magnitude of l_f is increased, and the temperature variations between the cases of $l_f = 50$ and 100 μm are comparably small. Figure 20 shows how ΔT_{max} decreases as the magnitude of l_f increases in each vessel; the inverse relationship between the maximum temperature ΔT_{max} and the fibrous cap thickness l_f has been also observed in experimental study [15]. The values of slope and intercept calculated are presented in Table VII.

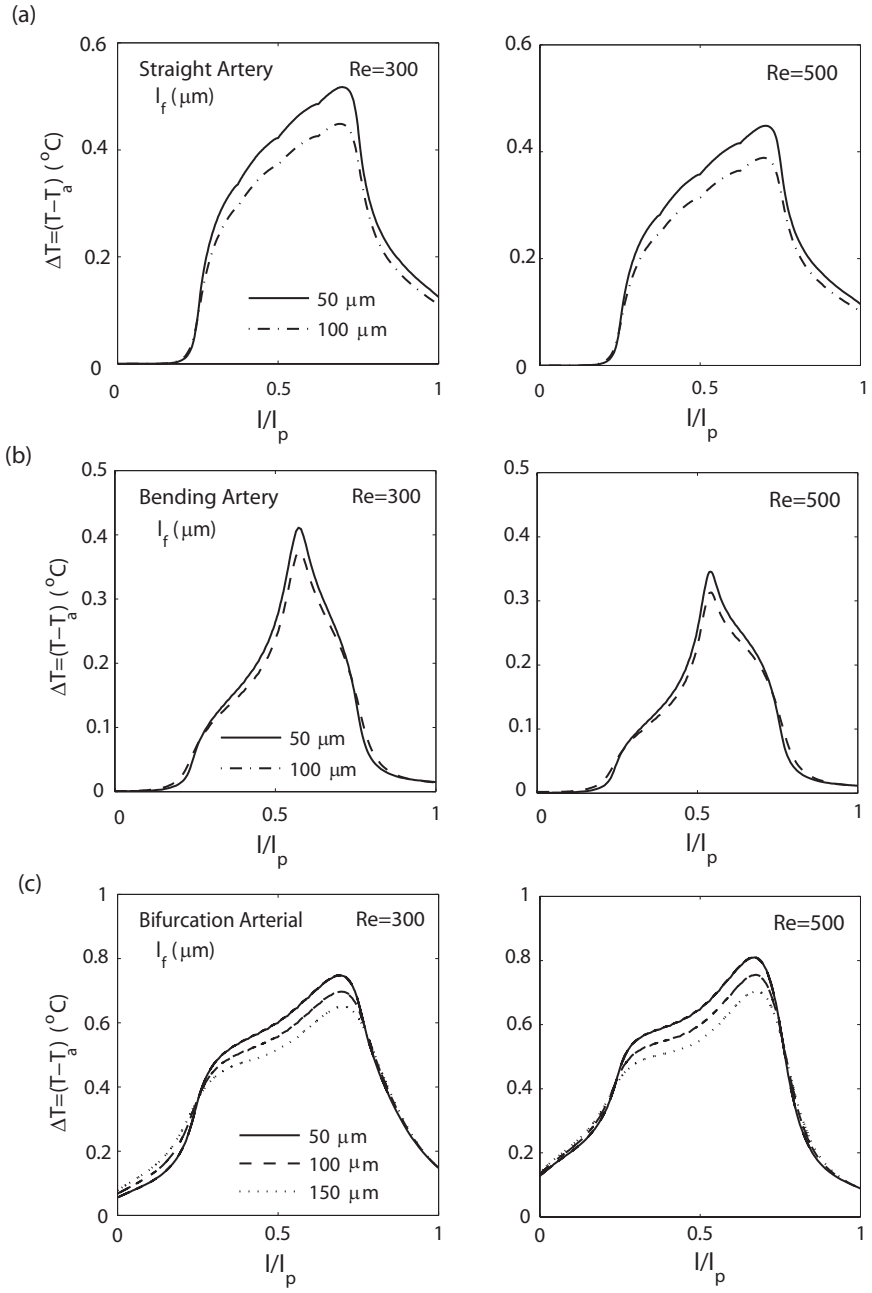

Fig. 19. Temperature change at the plaque/lumen interface produced by variations of the fibrous cap thickness l_f, corresponding to **(a)** stenotic straight artery with $\dot{q}_m = 0.1\ W/mm^3$, $l_{mp} = 3,335$, $d_p = 250$, $d_{mp} = 25\ \mu m$, **(b)** bending artery with $l_{mp} = 1,500$, $d_p = 540$, $d_{mp} = 25\ \mu m$, and **(c)** arterial bifurcation with $l_{mp} = 1,500$, $d_p = 670$, $d_{mp} = 25\ \mu m$.

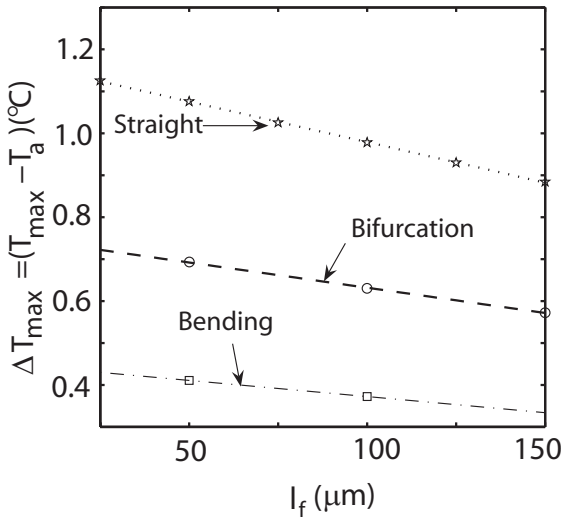

Fig. 20. Maximum temperature change ΔT_{max} at the plaque/lumen interface produced by variations in the fibrous cap thickness l_f for the three arterial geometries considered. The data fits a straight line $\Delta T_{max} = b + ml_f$, where the values of b and m are given in Table VII. Results shown correspond to $\dot{q}_m = 0.1\ W/mm^3$, $d_{mp} = 50\ \mu m$, $Re = 300$, and $d_p = 500$ (straight), 540 (bending), 670 μm (bifurcation).

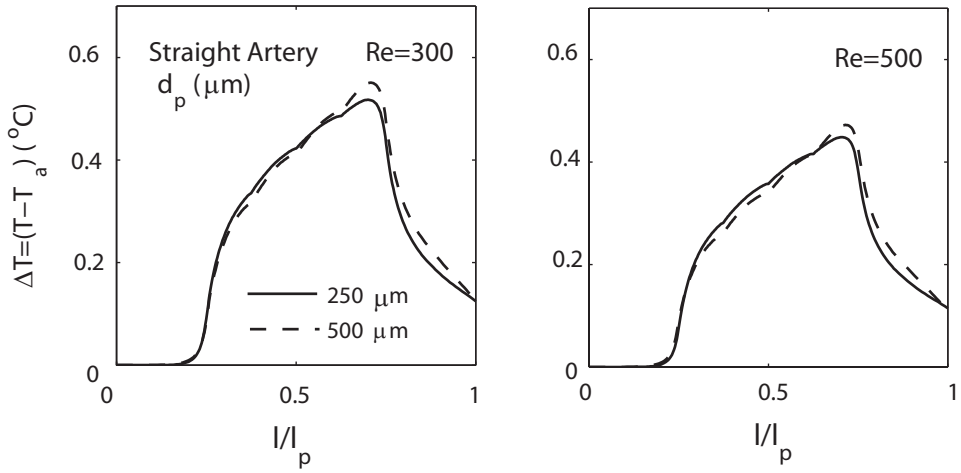

Fig. 21. Temperature change at the plaque/lumen interface produced by variations in the plaque thickness d_p for a straight artery. Results shown correspond to $\dot{q}_m = 0.1\ W/mm^3$, $l_{mp} = 3,335$, $d_{mp} = 25$, and $l_f = 50\ \mu m$ at $Re = 300$ and 500.

d. Variation of d_p

The effect of the plaque size is considered by varying plaque thickness d_p, which were 250 and 500 μm. In the straight artery, ΔT_{max} at $Re = 300$ is ranged between 0.52 and 0.55 ^oC for $d_p = 250$ and 500 μm, respectively (Table V and Figure 21). As the d_p is increased to 100%, the increases of ΔT_{max} are only 6 and 4% for $Re = 300$ and 500, which indicates that the size of the plaque does not considerably affect the temperature on the plaque/lumen interface. However, the significant increase of d_p implies that the vessel might be occluded to lead to blood flow reduction and considerably affect temperature variation, which is discussed in the section of *2-D Plaque Temperature during Blood Flow Reduction*. It is also observed that, as d_p is varied to 500 μm, ΔT slightly moves to the downstream of the plaque.

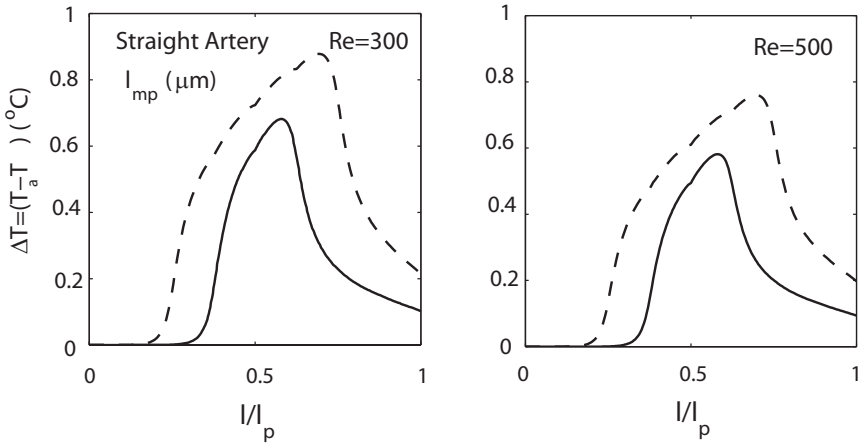

Fig. 22. Temperature change at the plaque/lumen interface produced by variations of the macrophage layer thickness $l_{mp} = 1,667$ and $3,335$ μm for a straight artery. Results shown correspond to $\dot{q}_m = 0.1$ W/mm^3, $d_p = 250$, $d_{mp} = 50$, $l_f = 100$ μm at $Re = 300$ and 500.

e. Variation of l_{mp}

The effect of the macrophage layer length is analyzed by the variations of l_{mp} in the straight artery. In Figure 22, ΔT_{max} at $Re = 300$ is between 0.68 and 0.88 ^oC, for $l_{mp} = 1,667$ and $3,335$ μm, respectively (Table V). As the length of the macrophage layer is reduced by half, ΔT_{max} is reduced from 0.88 to 0.68 ^oC at $Re = 300$, and from 0.76 to 0.58 ^oC at $Re = 500$.

f. Flow instabilities due to arterial geometries

Another important factor influencing over the AWT is the effect of flow instabilities because the temperature distribution is characterized by the blood flow pattern depending on the arterial geometries. Figure 23 describes the streamlines and temperature contours around atherosclerotic plaques at three different arteries. The flow instabilities presented by the streamlines affect the overall pattern of temperature

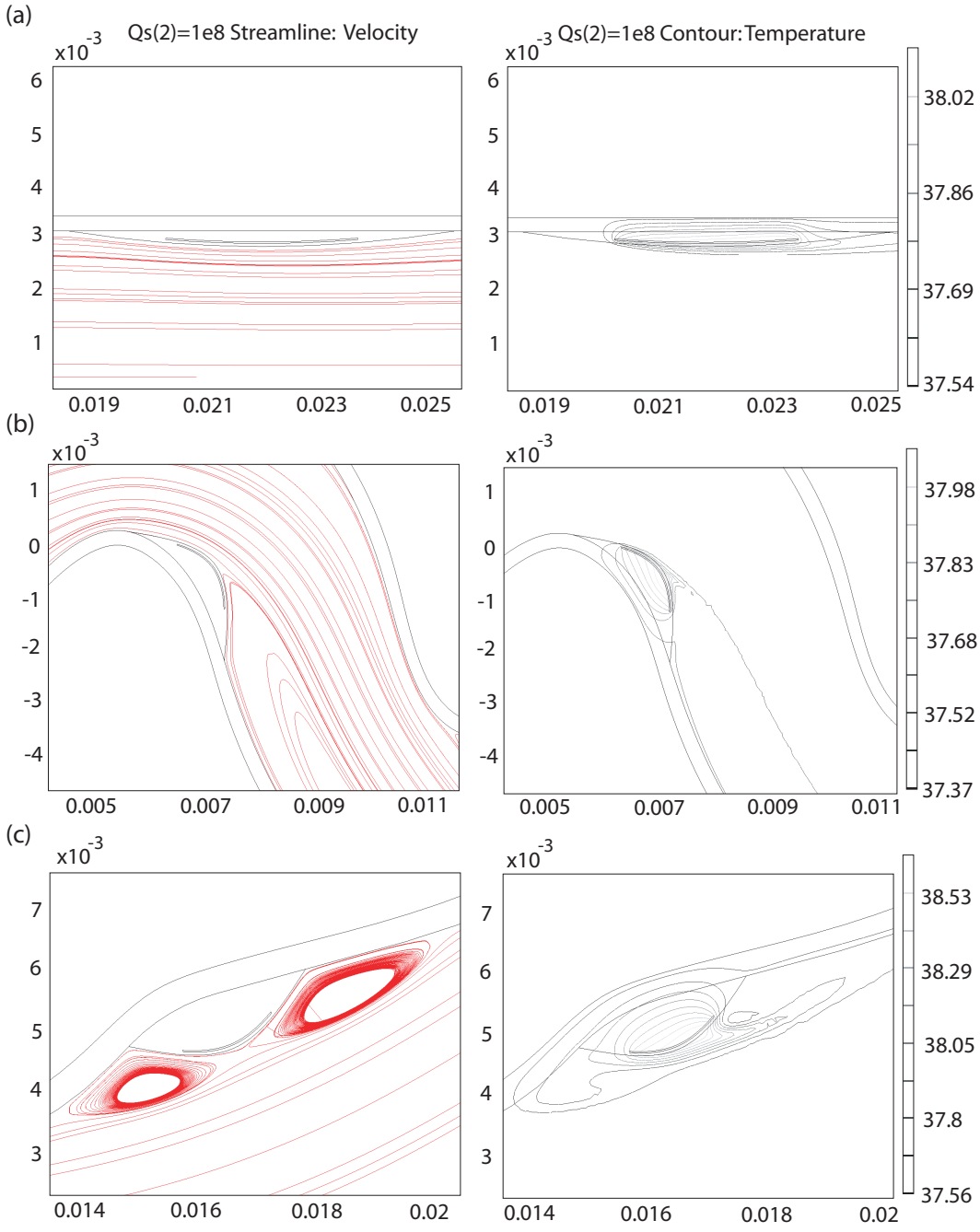

Fig. 23. Streamlines (left) and temperature contours (right) around atherosclerotic plaques at three different arteries: **(a)** straight, **(b)** bending and **(c)** arterial bifurcation. Results shown correspond to $Re = 500$ and $\dot{q}_m = 0.1\ W/mm^3$.

distribution at each artery: no flow instability at straight artery, flow separation at bending artery and flow circulation at arterial bifurcation. As shown in the streamlines of straight artery (Figure 23a), the blood smoothly flows from inlet to outlet without any flow instability. The temperature contours shows the convective cooling effect of blood flow. Meanwhile, bending artery (Figure 23b) presents the flow instabilities at the rear side of plaque where the boundary layer of blood flow encounters a separation point. Compared to the temperature change of straight arterial case, the temperature of bending artery is relatively higher at the rear of plaque where the convective cooling effect is weaken by the flow separation. In arterial bifurcation (Figure 23c), the streamlines shows two incompressible triangular cavity flows at the front and rear regions of the plaque, which are defined as flow circulations. The temperature distribution is directly affected by the presence of flow circulation. The thermal transport at the plaque surface is varied by the size of flow circulation resulting from velocity of blood flow. The details about quantifying the effect of flow circulation over the temperature variation is discussed in following section.

Effect of flow circulations

In the calculations of the arterial bifurcation (Figs. 16c, 17c and 19c), it is observed that the relation between ΔT_{max} and Reynolds number (Re = 300 and 500) is reversed to the cases of straight and bending arteries due to the flow instabilities around the plaque. Figure 24a illustrates that the streamlines present two flow circulations at the front and rear regions of the plaque. As the flow circulations become bigger along the increasing Reynolds number, the cooling effect of the blood flow reduces over plaque/lumen surface. It explains why the larger ΔT of the arterial bifurcation is occurred in Re = 500 (Figure 16c), which is contrary to the cases of bending and straight arteries (Figs. 16, 17 and 19).

To quantify the effect of flow circulation over the temperature variation of blood

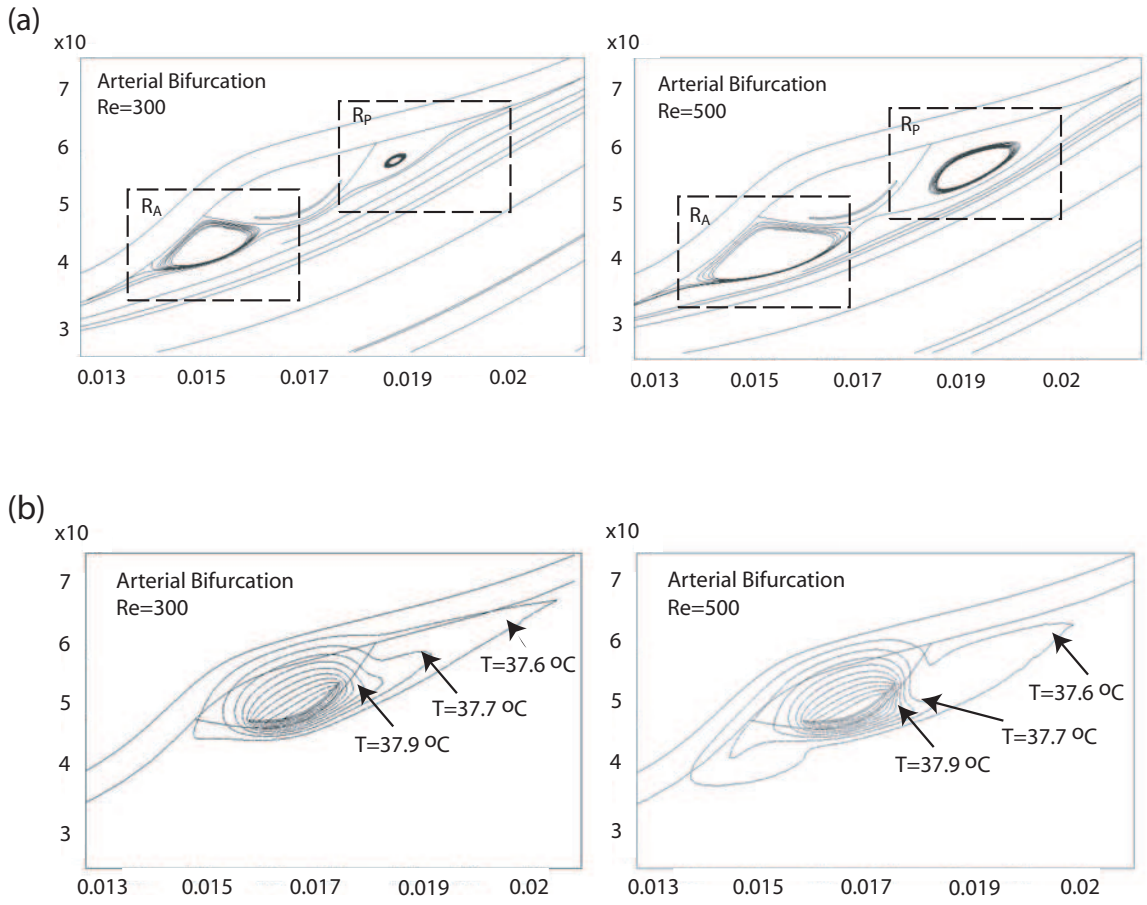

Fig. 24. **(a)** Flow circulation and **(b)** temperature contours observed around an inflamed plaque located in an arterial bifurcation. Results shown correspond to two different Reynolds Numbers ($Re = 300$ and $Re = 500$) and $\dot{q}_m = 0.1\ W/mm^3$, $d_p = 670$, $d_{mp} = 25$, $l_f = 100$ and $l_{mp} = 1500\ \mu m$.

flow surrounding the plaque, the absolute circulation is calculated in the anterior and posterior regions of the plaque as indicated in Figure 24a. These figures show the stream lines associated to the blood flow in the arterial lumen. The absolute circulation is calculated using the relationship based on the study [70],

$$\Gamma_{ABS}/A_{tot} = (\Sigma|\xi|\Delta A)/A_{tot}, \tag{3.12}$$

where A_{tot} is the total wetted area of the region of interest, ξ is the vorticity calculated by the curl of the velocity field, and ΔA represents the area of each mesh element inside the interest region. The values of the absolute or modified circulation (Γ_{ABS}/A_{tot}) are calculated for the different Reynolds numbers considered, and are given in Table VIII. These calculations are presented to quantify the flow structure near the plaque and relate such flow property to the temperature variation near the inflamed plaque. Figure 24b shows a series of temperature contours surrounding a plaque in an arterial bifurcation. As a result, the blood flow cooling effect decreases, as blood flow has the higher flow rate, because of the increase of flow circulation by the blood flow. Hence, the higher temperature is detected with higher Re in the plaque surface of arterial bifurcation.

g. The effect of metabolic heat generation

In a chemical reaction, the temperature (i.e., energy content of the system) is linearly correlated with the rate of product formation, which is called *Q10 law* [71]. It states that for every 10 ^oC increase in temperature, there are almost two times increase in the rate of the chemical reaction. According to the *Q10 law*, the rate of metabolic heat generation in atherosclerotic plaque can be promoted more quickly as temperature increases. The Metabolic heat production takes place because molecules such as

Table VIII. Average absolute circulation (Γ_{ABS}/A_{tot}) in the anterior (R_A) and posterior (R_P) regions of an atherosclerotic plaque in an arterial bifurcation. (unit: s^{-1})

Re. No.	R_A	R_P
300	87.1	101.5
400	105.2	120.2
500	122.9	139.5
600	140.0	159.2

The relationship for Γ_{ABS}/A_{tot} is obtained from [70], where Γ_{ABS} is the modified or absolute circulation parameter, and A_{tot} is the total wetted area over which Γ_{ABS} is calculated. The velocity profile is calculated considering the geometry indicated in Figure 15 and following parameters: $\dot{q}_m = 0.1\ W/mm^3$, $d_p = 500$, $d_{mp} = 50$, $l_f = 50$ and $l_{mp} = 1500\ \mu m$.

monocyte, macrophages, low-density lipoprotein (LDL) and oxygen (O_2) are moving and collide together to form the chemical bonds to hold them together in the plaque. The increased temperature due to the metabolic heat production provides the required energy to increase the moving speed of molecules. It is shown mathematically in the *Arrhenius equation* [71]; for a reaction between two substances A and B, the effect of changing the concentrations of the reactants is shown on the rate equation, $rate = k(A)^a(B)^b$, where superscripts of a and b present the order of reaction with respect to A and B. The rate constant, k, of *Arrhenius equation* is defined as

$$k = Ae^{-\frac{E_A}{RT}}, \tag{3.13}$$

where A is the frequency factor, taken as constant for a small temperature change of 10 ^oC, E_A denotes the minimum energy needed for the reaction to occur, R presents the gas constant, 8.32 $JK^{-1}mol^{-1}$, and T is the temperature in kelvin. If the temper-

ature in plaque is increased by 4 ^oC from 37.5 to 41.5 ^oC, the values of the fraction with an activation energy of 50 $kJmol^{-1}$ are varied from 3.84×10^{-9} to 4.91×10^{-9} in Eq. 3.13. We can see that the fraction of the molecules to react increases almost 28% by increasing the temperature by 4 ^oC. However, in this study, we did not consider *Q10 law*, the relationship between the temperature and the rate of metabolic reaction. Thus, the speed of the metabolic reaction is not governed by temperature increase in the plaque.

5. Conclusions of 2-D steady blood flow

According to the results of the parametric studies, the variation of ΔT was in proportion to metabolic heat generation q_m, macrophage layer thickness d_{mp} and plaque thickness d_p, whereas varied inversely with fibrous cap thickness l_f.

ΔT_{max} was located behind the apex of the plaque; the location of ΔT_{max} was governed by arterial geometry, distribution of macrophage layer, and flow instabilities such as flow separation and flow circulation. In this study, flow separation and circulation were observed in bending artery and arterial bifurcation, respectively. In bending artery, the thinner boundary layer before separation point enforced the convective cooling effect of blood flow at the upstream of the plaque. In arterial bifurcation, as blood velocity increased, the convective cooling effect at plaque/lumen surface was reduced with increasing the size of flow circulation over the plaque surface.

ten Have et al. have reported that the temperature difference at the lumen depends on heat source (macrophage layer) size, source geometry and heat source production, but no arterial geometry effect was mentioned for temperature distribution because the geometry used for a model was only a straight tube of a coronary artery [119]. In our study, however, it was also observed that the effect of arterial geometry was one of the significant factors affecting temperature distribution and

maximum temperature location because different geometries established the different blood flow profiles and the occurrence of flow instabilities resulting in the variation of local heat transfer at the plaque/lumen interface. For example, compared to the maximum temperature of straight artery case, those of the bending artery and the arterial bifurcation were approximately 20% lower and 60% higher, which was led by the effect of flow instabilities in terms of different arterial shape.

As the result, metabolic heat generation q_m accounting for macrophage population and macrophage layer thickness d_{mp} had more influence over the plaque temperature. Flow separation and circulation caused by arterial geometry also affected the AWT distribution. Furthermore, arterial wall temperatures were significantly influenced by the blood flow running through the vessel which was referred as the cooling effect of blood flow [16, 21]. In the presence of blood flow, the best spot to measure plaque temperature was between the middle and the far edge of the plaque where the point of maximum temperature could be located. It could be also postulated that direct measurements should be taken very close to the plaque/lumen surface.

B. 2-D Unsteady Blood Flow Calculations

1. Blood flow analysis

Transient calculations are carried out under the different physiological pulsatile flows of the arteries considered, as shown in Figure 25. The waveform functions consider a heart rate of approximately 60 beats per minute. The physiological flow profile of straight artery was obtained from the abdominal aorta illustrated by McDonald [72]. The waveform velocity function is characterized by a large forward flow during

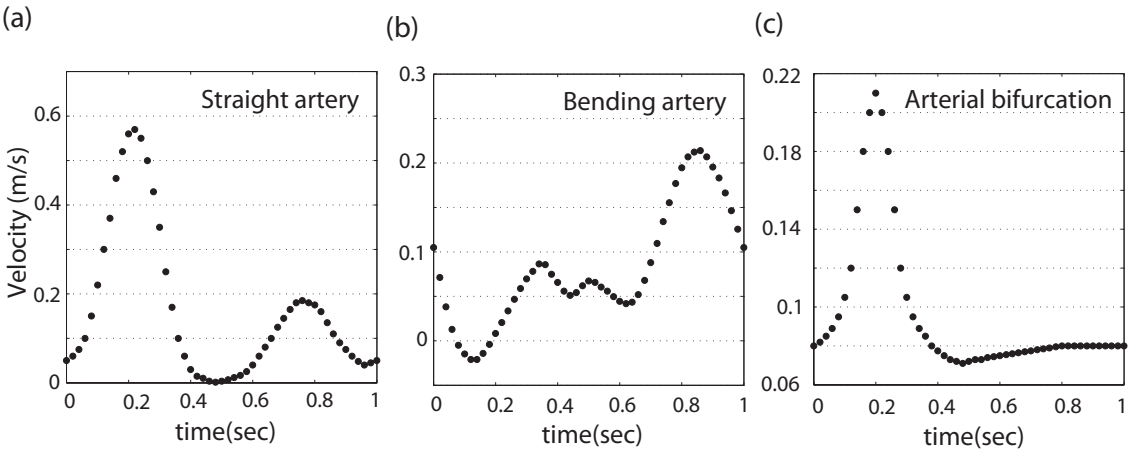

Fig. 25. Pulsatile flow waveform used at the inlet of **(a)** a straight artery [72], **(b)** a bending artery [59], and **(c)** an arterial bifurcation [73, 74].

a systole [2] and a slightly negative flow during a diastole [3]. The mean velocity is 0.154 m/s corresponding to the mean Reynolds number of 303, and the maximum and minimum velocities are 0.57 and -0.05 m/s, respectively. The pulsatile profile of bending artery was recorded in the right coronary artery of a normal 56-year-old female [59]. The velocity profile contains some periods of reverse flow as well as periods of rapid acceleration and deceleration. The waveform function was scaled to yield a mean inflow velocity of 0.08 m/s corresponding to the mean Reynolds number of 92, the maximum velocity is 0.21 m/s, and the minimum velocity is -0.021 m/s. The waveform of bifurcation artery was obtained experimentally by Gijsen et al. [73]. The Reynolds number corresponded by the mean velocity of 0.096 m/s is 92. The flow velocity shows a rapid acceleration and deceleration of systole (the maximum velocity is 0.0171 m/s) and then gradually adapt to the slower inlet velocity changes

[2]The contraction of the heart by which the blood is forced onward and the circulation kept up.

[3]The heart rests and no blood is ejected.

during a diastole.

Arterial blood flow is described by the time-dependent Navier-Stokes equations for incompressible, homogenous and Newtonian fluids:

$$\rho\left(\frac{\partial \mathbf{v}}{\partial t} + \mathbf{v}\cdot\nabla\mathbf{v}\right) = -\nabla P + \mu\nabla^2\mathbf{v}, \tag{3.14}$$

$$\nabla\cdot\mathbf{v} = \mathbf{0}, \tag{3.15}$$

where $\mathbf{v}$ is the velocity vector of the blood, t the time, P the pressure of blood, ρ the density of blood and μ the viscosity of blood. The velocity profile at the inlet ($\ell = 0$) is assumed to be uniform with a pulsatile waveform as a function of time as shown in Figure 25.

$$u = u(t), \quad v = 0 \quad \text{at} \quad \ell = 0, \tag{3.16}$$

where the lengths of inlets are extended to $10D$ for bending artery and to $5D$ for arterial bifurcation because more inlet distances are required for the velocity profile to become fully developed. The same boundary conditions used in the steady case are applied (Figure 9): no-slip conditions at the arterial walls, $u = 0$ and $v = 0$ at $r = R_i$, and a fully developed flow at the outlet, $P = 0$ at $\ell = L_o$. The initial condition of the unsteady case is obtained from the calculations of 2-D steady blood flow case where the time-averaged velocities u_o are applied with 0.154, 0.08 and 0.096 m/s for straight, bending and arterial bifurcation, respectively.

2. Thermal analysis

To determine the temperature of arterial wall and the inflamed plaque, time-dependent energy equation with heat generation term is solved. The transient energy equation

is

$$\rho_i C_{Pi} \left(\frac{\partial T_i}{\partial t} + (\mathbf{v} \cdot \nabla) T_i \right) - \nabla \cdot (k_i \nabla T_i) = \dot{q}_{mi} \tag{3.17}$$

where i refers to blood ($i = 1$), arterial wall ($i = 2$), plaque ($i = 3$) and macrophage layer ($i = 4$). T_i represents the temperature, $\mathbf{v}$ the velocity of blood in the lumen region, k_i the thermal conductivity, ρ_i the density, and C_{Pi} the specific heat. $\dot{q}_{mi}$ represents the metabolic heat produced by the macrophage layer ($i = 4$). The mechanical properties and applied assumptions for each domain such as blood flow, arterial wall and plaque structure, are the same as the case of steady blood flow (Table IV). Also, the boundary conditions considered for the energy equation (3.17) are the same as the case of 2-D steady flow (Figure 9): fixed temperature at the inlet and external vessel wall ($T = T_a$ at $\ell = 0$ and $r = R_o$), and no temperature gradient at the vessel outlet ($\frac{\partial T}{\partial \ell} = 0$ at $\ell = \mathrm{L_o}$).

3. Results of 2-D unsteady blood flow

In this section, the temperature variations during cardiac cycles are determined with varying $\dot{q}_m$, d_{mp} and l_f because $\dot{q}_m$ and d_{mp} have more influence over the plaque temperature, and l_f has the inverse relation on temperature. Flow instabilities due to blood flow momentum at different arterial geometries are observed, which present the effect of inlet pulsatile flow over the arterial wall temperature.

a. Variation of $\dot{q}_m$

During cardiac cycle, temperature distribution at plaque surface varies with three different heat generations, $\dot{q}_m = 0.05$, 0.1 and 0.2 W/mm^3. Figure 26 shows the snapshots of temperature distribution along the plaque/lumen surface at different

times through cardiac cycles; the times selected represent when the velocity profile (Figure 25) presents the maximum, the minimum or other meaningful behavior at the plaque region. The horizontal axis coincides with the plaque/lumen interface.

For straight artery (Figure 26a), the representative times were selected in terms of the characteristic of inlet pulsatile flow (Figure 25) as follows: **(a)** $t = 2.0$ & 3.0 are the times for beginning and ending of the cycle, **(b)** $t = 2.2$ shows the peak velocity **(c)** $t = 2.4$ presents the beginning and the ending of a reverse flow, **(d)** $t = 2.6$ is the returning to the small forward flow, and **(e)** $t = 2.8$ corresponds to the maximum point of the small forward flow. During a cardiac cycle, the temporal temperature change is varied between 0.3 and 1.1 ^oC for $\dot{q}_m = 0.05$ and 0.2 W/mm^3, respectively. The maximum spatial temperature ΔT_{max} occurs closer to the downstream edge of the plaque at l/l_p=0.7, which is almost identical to the steady-state solution. There is no flow instability during the cycle, and the location of maximum spatial temperature ΔT_{max} stay at almost constant location. After the maximum blood flow ($Re = 1,125$) occurs at $t = 2.2s$, the maximum convective effect at the plaque is shown around $t = 2.4s$ due to the time delay from the inlet flow. After passing a reverse flow, the temperature variation at $t = 2.6s$ is immediately recovered to the temperature pattern as the steady-state case.

In bending artery (Figures 26b and 25), the representative times were chosen as follows: **(a)** $t = 4.0$ and $5.0s$ represents the beginning and the ending of the cardiac cycle, **(b)** $t = 4.2$ is the maximum of a reverse flow, **(c)** $t = 4.4s$ is the peak of a small forward flow occurs, **(d)** $t = 4.6$ is the deceleration phase, and **(e)** $t = 4.8s$ is an approximately halfway through the rapid forward flow. It is shown that temporal temperature changes are varied between 0.2 and 1.1 ^oC for $q_m = 0.05$ and 0.2 W/mm^3, respectively. The location of maximum temperature varies to the characteristics of inlet blood flow, *i.e.* temporal ΔT_{max} is reduced

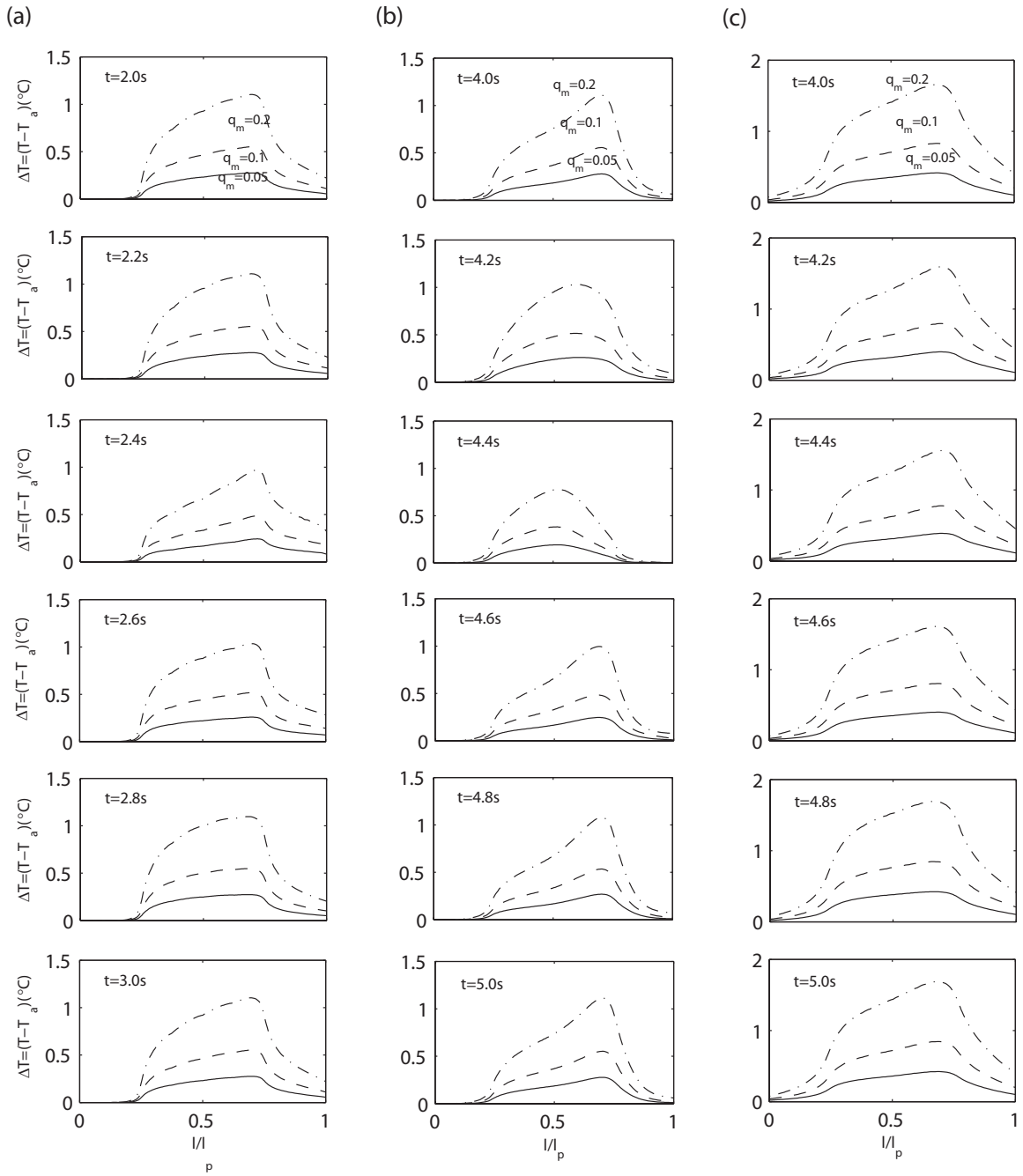

Fig. 26. Transient temperature distribution produced by variations of heat generation $\dot{q}_m$ (W/mm^3) for **(a)** straight artery (t = 2.0 to 3.0s), **(b)** bending artery (t = 4.0 to 5.0s), and **(c)** arterial bifurcation (t = 4.0 to 5.0s).

at $4.4s$, and increases after $t = 4.6s$. Spatial ΔT_{max} occurs closer to the center of the plaque when the blood velocity is reduced at $t = 4.4s$, and moves to the downstream edge of the plaque as blood flow increases in the last moment of the cardiac cycle from $t = 4.6s$. The variation of spatial maximum temperature ranges between $0.5 < l/l_p < 0.75$ during the cardiac cycle; ΔT_{max} is located between the vertical lines drawn in the figures (the solid line represents the location of ΔT_{max} at $t = 4.0$, 4.6, 4.8 and $5.0s$ and the dashed line indicates ΔT_{max} at $t = 4.2$ and $4.4s$). It is also observed that the temperature goes higher at the downstream edge of plaque (between $t = 4.8$ and $5.0s$) because the flow separation caused by a large forward flow prevent the transport of thermal energy from the plaque surface.

For arterial bifurcation in Figure 26c, the representative times are $t = 4.0$, 4.2, 4.4, 4.6 and $4.8s$. In Figure 25, the velocity waveform for the bifurcation does not present significant variation except the peak velocity at $t = 4.2s$. Therefore, the maximum temperature and temperature distribution do not spatially or temporally change during the cycle. The locations of the spatial maximum temperature are relatively constant at the downstream of the plaque between $0.6 < l/l_p < 0.7$. As the blood velocity increases between $t = 4.2$ and $4.4s$, the temperature at the plaque/lumen interface increases with the effect of flow circulation; it was previously discussed in the steady-state case where the presence of flow circulation reduces the cooling effect at the anterior and posterior of the plaque. These flow circulations produce incompressible triangular cavities which keep circular flow regions resulting in less transport thermal energy. Because of the effect of flow circulations, temperature distributions do not dramatically vary in spite of a significant peak of pulsatile flow at $t = 4.2s$.

b. Variation of d_{mp}

In Figure 27, the temperature distribution at different times are also shown with varying the macrophage layer thickness of $d_{mp} = 25$, 50 and 100 μm with the metabolic heat of $q_m = 0.1\ W/mm^3$.

Figure 27a presents that maximum temporal temperature ΔT_{max} is between 0.4 and 2.0 ^oC for $d_{mp} = 25$ and 100 μm, respectively, in straight artery. As d_{mp} increases, ΔT_{max} proportionally increases, which shows a good agreement with the steady-state calculations. During a cardiac cycle, the maximum spatial temperature ΔT_{max} constantly occurs at $l/l_p = 0.7$ on the right edge of the plaque.

For bending artery in Figure 27b, the maximum temporal temperature ΔT_{max} are ranged from 0.5 ^oC for $d_{mp} = 25$ to 2.0 ^oC for 100 μm. ΔT_{max} for $d_{mp} = 100\ \mu m$ decreases to 1.5 ^oC at $t = 4.4s$, and increases to 2.0 ^oC after $t = 4.8s$. During the cardiac cycle, the locations of the maximum spatial temperature ΔT_{max} move between $0.5 < l/l_p < 0.75$; the locations are closer to the center of the plaque under the lower blood velocity, and move to the downstream edge of the plaque as blood flow increases during a cycle.

Figure 27c shows that the maximum temperature in the arterial bifurcation are ranged from 0.5 to 3.0 ^oC for $d_{mp} = 25$ and 100 μm. The temperature distributions do not change a lot during the cycle, and the maximum temperature locations occur constantly at between $0.6 < l/l_p < 0.7$, which is associated with the presence of flow circulation near the plaque.

c. Variation of l_f

Figure 28 shows that the temperature variations are reversely related with the fibrous cap thickness ($l_f = 25$, 50 and 100 μm). For straight artery, Figure 28a presents that

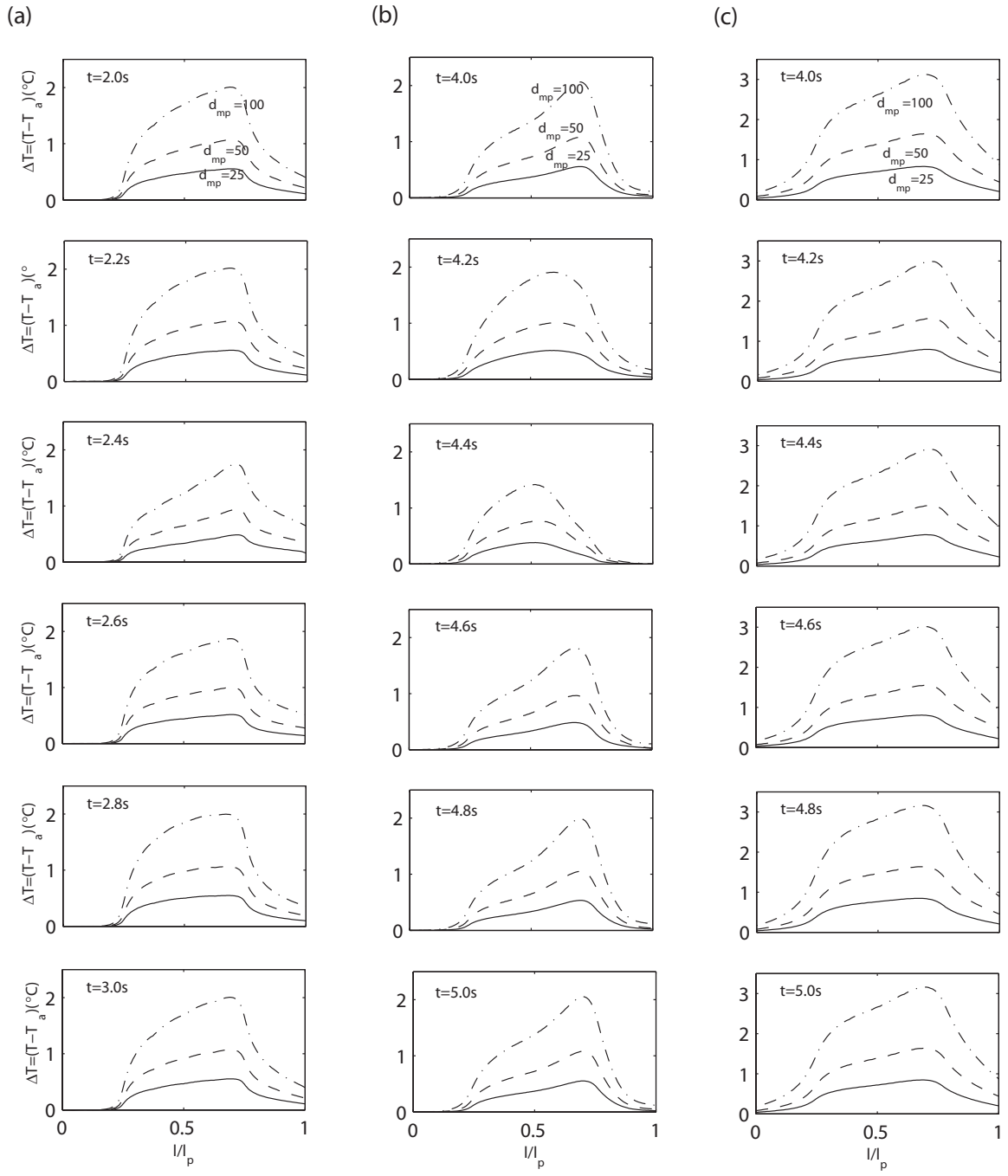

Fig. 27. Transient temperature distribution produced by variations of macrophage layer thickness d_{mp} for **(a)** straight artery (t = 2.0 to 3.0s), **(b)** bending artery (t = 4.0 to 5.0s), and **(c)** arterial bifurcation (t = 4.0 to 5.0s).

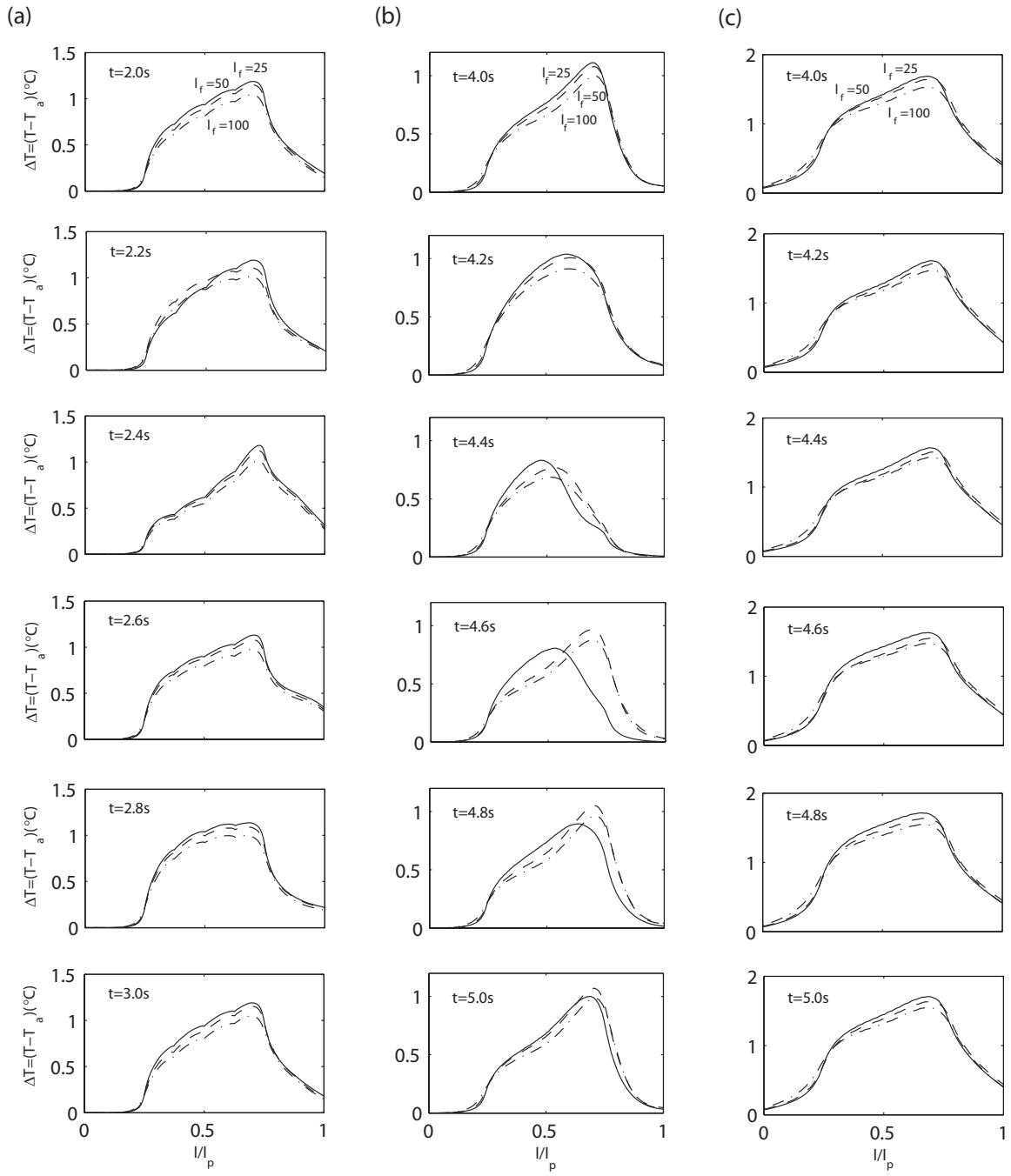

Fig. 28. Transient temperature distribution produced by variations of fibrous cap thickness l_f for **(a)** straight artery ($t = 2.0$ to $3.0s$), **(b)** bending artery ($t = 4.0$ to $5.0s$), and **(c)** arterial bifurcation ($t = 4.0$ to $5.0s$).

the maximum temporal temperature ΔT_{max} is between 0.8 and 1.2 ^oC for $l_f = 25$ and 100 μm, respectively. The maximum temperature is decreased as the magnitude of l_f is increased with an inverse relationship, but the temperature variation is relatively small, comparing to the other cases (q_m and d_{mp}). The locations of maximum spatial temperature ΔT_{max} are occurred at $l/l_p = 0.7$ on the right edge of the plaque. Figure 28b for bending artery shows that the maximum temporal temperature for $l_f = 100$ μm decreases to 0.7 ^oC at $t = 4.4s$, and increases to 1.0 ^oC at $t = 5.0s$. The maximum spatial temperature ΔT_{max} occurs closer to the center of the plaque, and moves to the downstream edge of the plaque, which is between $0.5 < l/l_p < 0.75$. For arterial bifurcation, Figure 28c presents that maximum temporal temperature ΔT_{max} varies with a range between 1.5 and 1.8 ^oC for $l_f = 25$ and 100 μm, respectively. During a cardiac cycle, the maximum spatial temperature constantly occurs at the rear side of the plaque between $0.6 < l/l_p < 0.7$.

As the fibrous cap thickness l_f increases, the maximum temperature ΔT_{max} decreases. Compared with the variation of $\dot{q}_m$ and d_{mp} during a cycle, the temporal variation of ΔT_{max} is considerably small because the metabolic heat from macrophage cell layer is not transferred well through the fibrous cap having the comparably lower thermal conductivity. It is observed that spatial and temporal ΔT_{max} in the transient case are affected by the characteristics of the inlet waveform function containing a forward and a reverse flow as well as the effect of the vessel geometry. As a result, the variation of temperature distribution is affected by the characteristics of the inlet blood flow, the flow instabilities due to the arterial geometry effect, and the arterial wall conductivity.

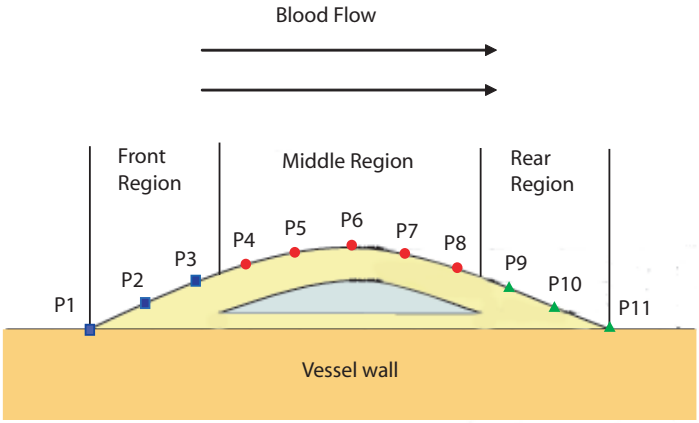

Fig. 29. Three thermal regions along the plaque/lumen surface designated by **(1)** a front region (P1, P2 and P3) which has no conduction and convection effect, **(2)** a middle region (P4 through P7) which has both of conduction and convection effects, and **(3)** a rear region (P9, P10 and P11) which has no conduction, but significant convection effect)

d. Thermal regions at the plaque surface

In order to trace the temperature history over the plaque/lumen interface during cardiac cycles, eleven representative points are selected in Figure 29. According to the temperature histories at the representative points, three thermal regions with the different patterns of temperature variations are observed in each arterial case. The regions are identified by: **(1)** a front region where temperature is not varied much because it is not affected by the presence of the macrophage layer but also by the pattern of blood flow (no conduction and no convection effect); **(2)** a middle region where temperature is directly affected by the macrophage layer dimensions and the blood flow (conduction and convection effect); and thirdly, **(3)** a rear region where

the convective heat transfer is dominant due to the blood flow over the presence of the macrophage layer (no conduction but convection effect). To study such regional variations of the plaque temperature in details, four points (**A**, **B** , **C** and **D**) are reselected out of the representative points. Point **A** corresponds to the center of the plaque (P6), point **B** presents the end of the mid region (P8), point **C** is the beginning of the rear region (P9), and point **D** is the end of the plaque (P11).

e. Variation of $\dot{q}_m$ at representative points

Figure 30 shows the temperature histories at the representative four points (**A**, **B**, **C** and **D**) with $\dot{q}_m = 0.05$, 0.1 and 0.2 W/mm^3 during three cardiac cycles.

For the straight artery, the temperatures at points **A**, **B** and **C** are changed from 0.15 to 0.27 ^oC at $\dot{q}_m = 0.05$ W/mm^3, 0.3 to 0.53 ^oC at $\dot{q}_m = 0.1$ W/mm^3, and 0.5 to 1.1 ^oC at $\dot{q}_m = 0.2$ W/mm^3 (Figure 30a). It is shown that the temperature variations are proportionally increased with increasing heat generation $\dot{q}_m$. The maximum temperature occurs at point **C**, the beginning of a rear region. The temperature changes of point **B** are almost overlapped by those at point **C**. Meanwhile, at points **A** and **B** on a middle region, the temperature changes follow the similar patterns corresponding to the waveform of inlet pulsatile flow. The temperature changes at point **D** remains relatively constant during the cycles. In the case of straight artery, ΔT at the middle regions (**A** and **B**) is varied depending more on the characteristics of an inlet velocity.

In Figure 30b for bending artery, the temperature changes at points **A**, **B** and **C** occurs at between 0.2 and 1.1 ^oC at $\dot{q}_m = 0.2$ W/mm^3. The temperature are proportionally increased with increasing heat generation $\dot{q}_m$. The maximum temperature is occurred at point **C**. Comparing to the case of straight artery in figure 30a, the temperature variations at points **B** and **C** show the similar pattern with more dras-

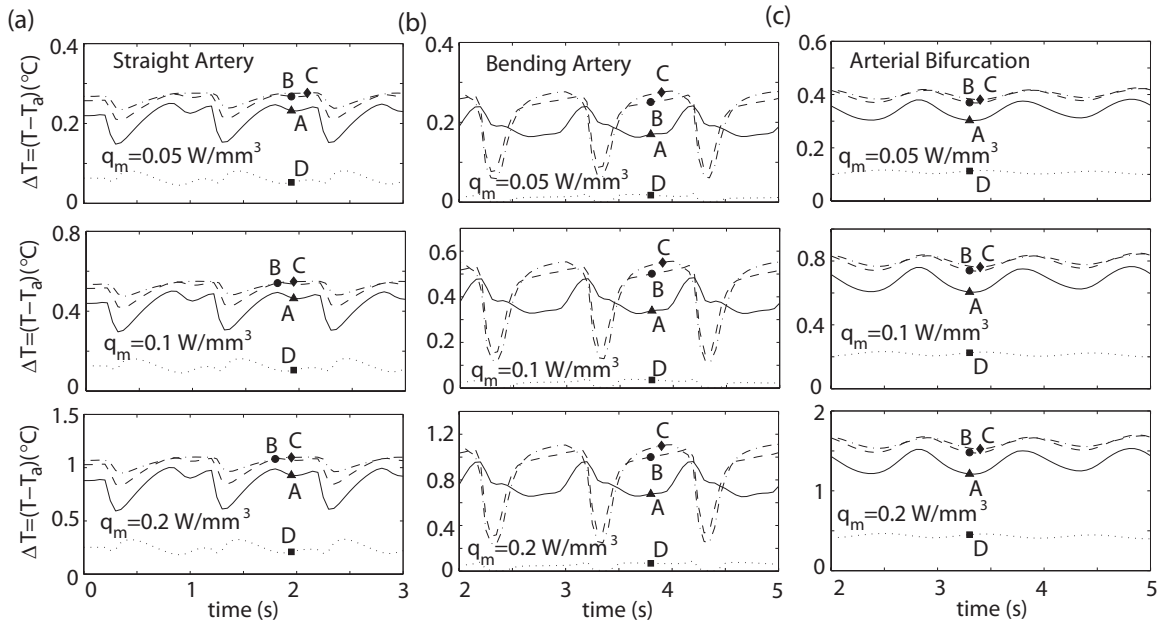

Fig. 30. Temperature history under the variation of heat generation, $\dot{q}_m = 0.05$, 0.1 and 0.2 W/mm^3, during 3 cardiac cycles. Temperature is recorded at the representative four points (**A**, **B**, **C** and **D**) at plaque surface of **(a)** straight artery ($d_p = 250$, $d_{mp} = 25$, $l_f = 50$ and $l_{mp} = 3,335\ \mu m$), **(b)** bending artery ($d_p = 540$, $d_{mp} = 25$, $l_f = 50$ and $l_{mp} = 1,500\ \mu m$) and **(c)** arterial bifurcation ($d_p = 670$, $d_{mp} = 25$, $l_f = 50$ and $l_{mp} = 1,500\ \mu m$). Temperature

.

tic changes due to flow separation. The characteristic of inlet blood flow combined with the geometry effect of bending artery causes the flow separation at particular seconds during cardiac cycles. At point **D**, the temperature change remains relatively constant because the flow separation at the rear region lessen thermal transport from the surface. Thus, flow momentum and instabilities occurred by inlet pulsatile flow and geometry effect seem to affect the characteristics of temperature variations.

Figure 30c presents that the temperature changes in arterial bifurcation are between 0.1 and 1.7 ^oC at points **A**, **B**, **C** and **D** with $\dot{q}_m = 0.05, 0.1$ and $0.2\ W/mm^3$. The temperature variations are proportionally increased with increasing heat generation $\dot{q}_m$. The maximum temperature is also occurred at points **C** and **B**, and the temperature variations at point **A**, **B** and **C** show the almost same patterns during cardiac cycles. Point **D** presents relatively constant but higher temperature value because of the flow circulation causing the lower convective effect.

f. Variation of d_{mp} at representative points

Transient temperature changes with the variation of macrophage layer thickness, $d_{mp} = 25$, 50 and $100\ \mu m$ at $\dot{q}_m = 0.1\ W/mm^3$, are calculated at points **A** through **D** during three cardiac cycles.

Figure 31a shows that the temperatures are changed between 0.1 and 2.0 ^oC at points **A** through **D** with varying d_{mp}. It can be seen that ΔTs are proportionally increased with increasing d_{mp} and the maximum temperature is occurred at point **C** during the cycles. At points **A**, **B** and **C**, the temperature changes follow the similar patterns as the case of varying $\dot{q}_m$. For the bending artery, the temperature for $d_{mp} =$ 25, 50 and $100\ \mu m$ changes between 0 and 2.0 ^oC. The temperature changes at points **B** and **C** follow the similar pattern. Figure 31c for the arterial bifurcation shows that the temperature varies between 0.2 and 3.2 ^oC with varying d_{mp}. The temperature

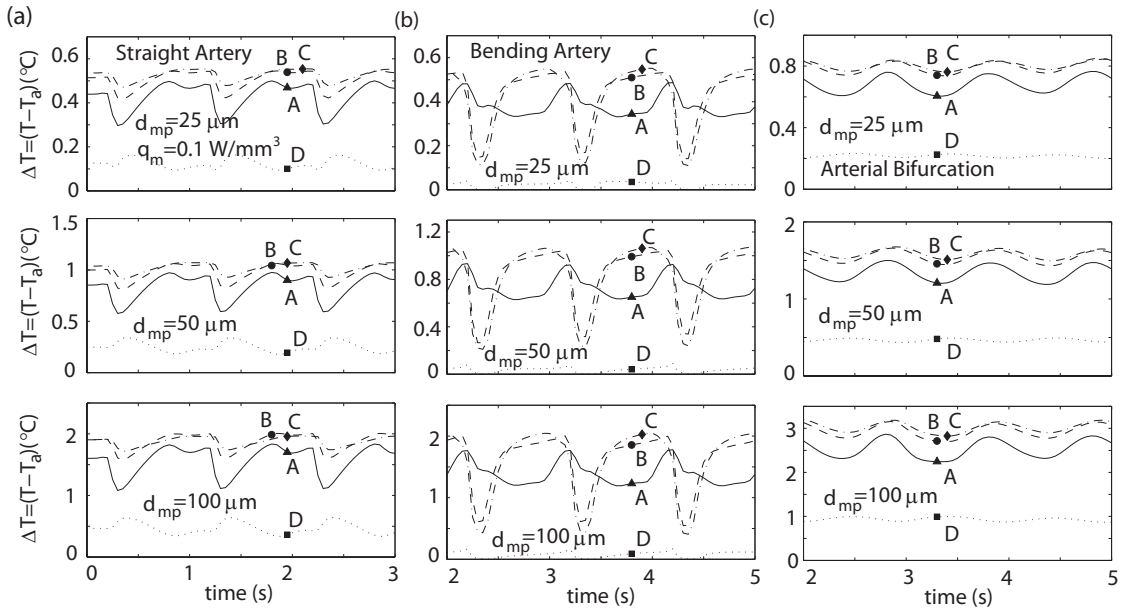

Fig. 31. Temperature history under the variation of macrophage layer thickness, $d_{mp} = 25$, 50 and 100 μm during 3 cardiac cycles. Temperature is recorded at the representative points (**A**, **B**, **C** and **D**) at the plaque surface of **(a)** straight ($d_p = 250$, $l_f = 50$ and $l_{mp} = 3,335$ μm), **(b)** bending ($d_p = 540$, $l_f = 50$ and $l_{mp} = 1,500$ μm) and **(c)** arterial bifurcation ($d_p = 670$, $l_f = 50$ and $l_{mp} = 1,500$ μm).

variations of arterial bifurcation shows negligibly small variations compared to other arterial cases under the effect of flow circulation. The temperature at point **D** also remains relatively constant and higher compared to other arterial cases due to the flow circulation causing the lower convective effect of blood flow.

g. Variation of l_f at representative points

This section shows the transient temperature changes at points **A** through **D** with the variation of fibrous cap thickness, $l_f = 25$, 50 and 100 μm at $\dot{q}_m = 0.1\ W/mm^3$.

For the straight artery in Figure 32a, the temperature is changed between 0.2 and 1.3 ^oC at four points with varying l_f. The temperature is decreased with an inverse relationship as the magnitude of l_f is increased leading to the conductive effect. However, the temperature variation is insignificant compared with the cases of q_m and d_{mp}. The maximum temperature is occurred at point **C** and the temperature changes at point **D** remains relatively constant during cardiac cycles. Figure 28b for bending artery shows that the temperature is changed between 0 and 1.1 ^oC at four points with varying l_f. Point **C** has the maximum temperature, and points **B** and **C** show the most drastic temperature variations due to blood flow momentum, and the point **D** remains relatively constant temperature. In arterial bifurcation in Figure 28c, the maximum temperature is between 0.4 and 1.7 ^oC for $l_f = 25$ and 100 μm, respectively. The temperatures at all selected points (**A** through **D**) show little variations during the cycles compared to those of other arteries.

As a result, as the fibrous cap thickness l_f is increased, the temperature is decreased. However, compared with the variations of $\dot{q}_m$ and d_{mp}, the temperature variation is considerably small.

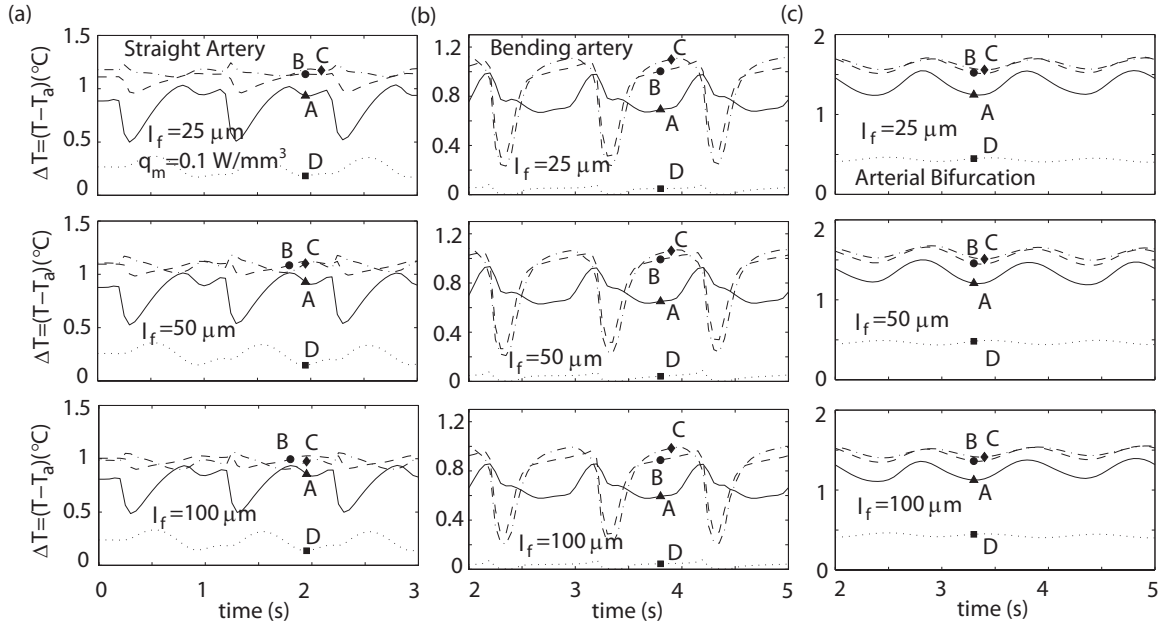

Fig. 32. Temperature history under the variation of fibrous cap thickness, l_f = 25, 50 and 100 μm during 3 cardiac cycles. Temperature is recorded at the representative four points (**A**, **B**, **C** and **D**) on the surface of plaque for **(a)** straight artery (d_p = 250 μm, d_{mp} = 25 and l_{mp} = 3,335), **(b)** bending artery (d_p = 540, d_{mp} = 25 and l_{mp} = 1,500) and **(c)** arterial bifurcation ($d_p = 670$, $d_{mp} = 25$ and $l_{mp} = 1,500$).

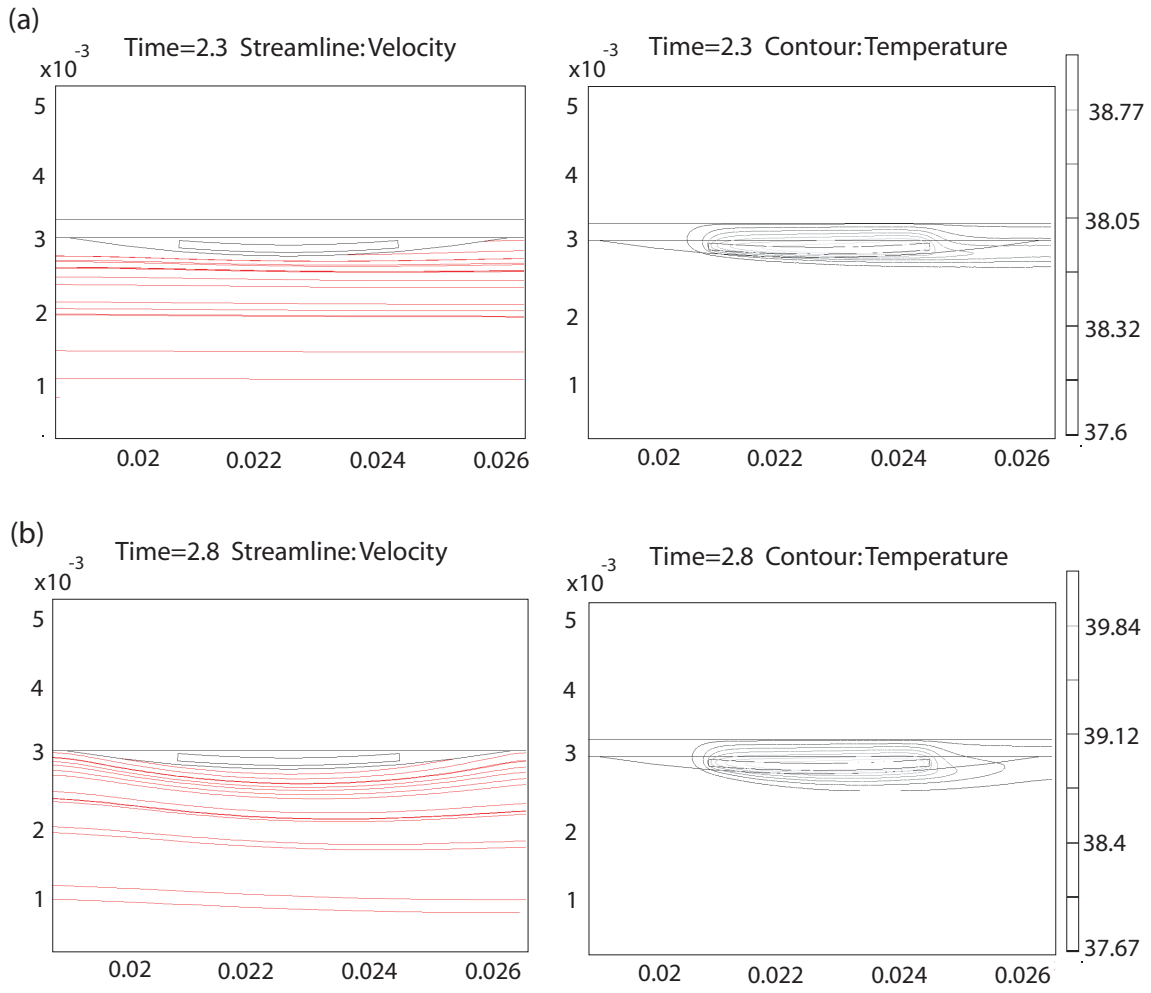

Fig. 33. Streamlines (left) and temperature contours (right) around an inflamed plaque in straight artery. Times **(a)** $t = 2.3$, and **(b)** $2.8s$ are selected during the cardiac cycle (Figure 25a). The dimensions of plaque are $l_{mp} = 3,335$, $d_{mp} = 100$, $d_p = 250$, and $l_f = 50\ \mu m$, and the metabolic heat production is $\dot{q}_m = 0.1\ W/mm^3$.

h. Flow instabilities due to inlet pulsatile flow

According to the results of steady flow calculation, the temperature distribution is strongly characterized by the flow instabilities depending on the arterial geometries. In the case of unsteady flow calculation, the different pulsatile functions are applied for the inlet flow at each artery (Figure 25). During cardiac cycles, the flow instabilities are repeatedly appeared and disappeared by the characteristics of inlet pulsatile flow as well as arterial geometries. In this section, two different times during one cycle are selected to compare the variations of temperature and streamlines.

For the straight artery, the snapshots of streamlines and temperature contours at different times are depicted in Figure 33. In order to present the effect of inlet pulsatile flow, $t = 2.3$ and $2.8s$ are selected during the cardiac cycle (Figure 25); $t = 2.3s$ is the time for the stronger forward flow during the cycle and $t = 2.8s$ is selected for the backward flow after small forward flow. During the entire cardiac cycle, the blood smoothly flows without flow instabilities and the convective cooling effect of the blood flow steadily affect the temperature distribution at plaque surface. The temporal temperature change at plaque surface is observed by the characteristics of the inlet pulsatile flow. Despite of the stronger forward flow at $t = 2.3s$, the plaque size is so small that the flow instabilities are not occurred. Therefore, the spatial temperature change is not presented at the plaque surface.

Figure 34 shows the temperature contours surrounding the atherosclerotic plaque in the bending artery at two different times ($t = 4.4$ and $4.8s$). According to the inlet velocity profile of Figure 25, $t = 4.4s$ is the time to begin the backward flow after small forward flow of pulsatile waveform. At $t = 4.4s$, the streamlines present that the blood flow is not temporarily moved at the plaque. At the same time, the convective cooling effect of blood flow is disappeared and the temperature distribution is almost

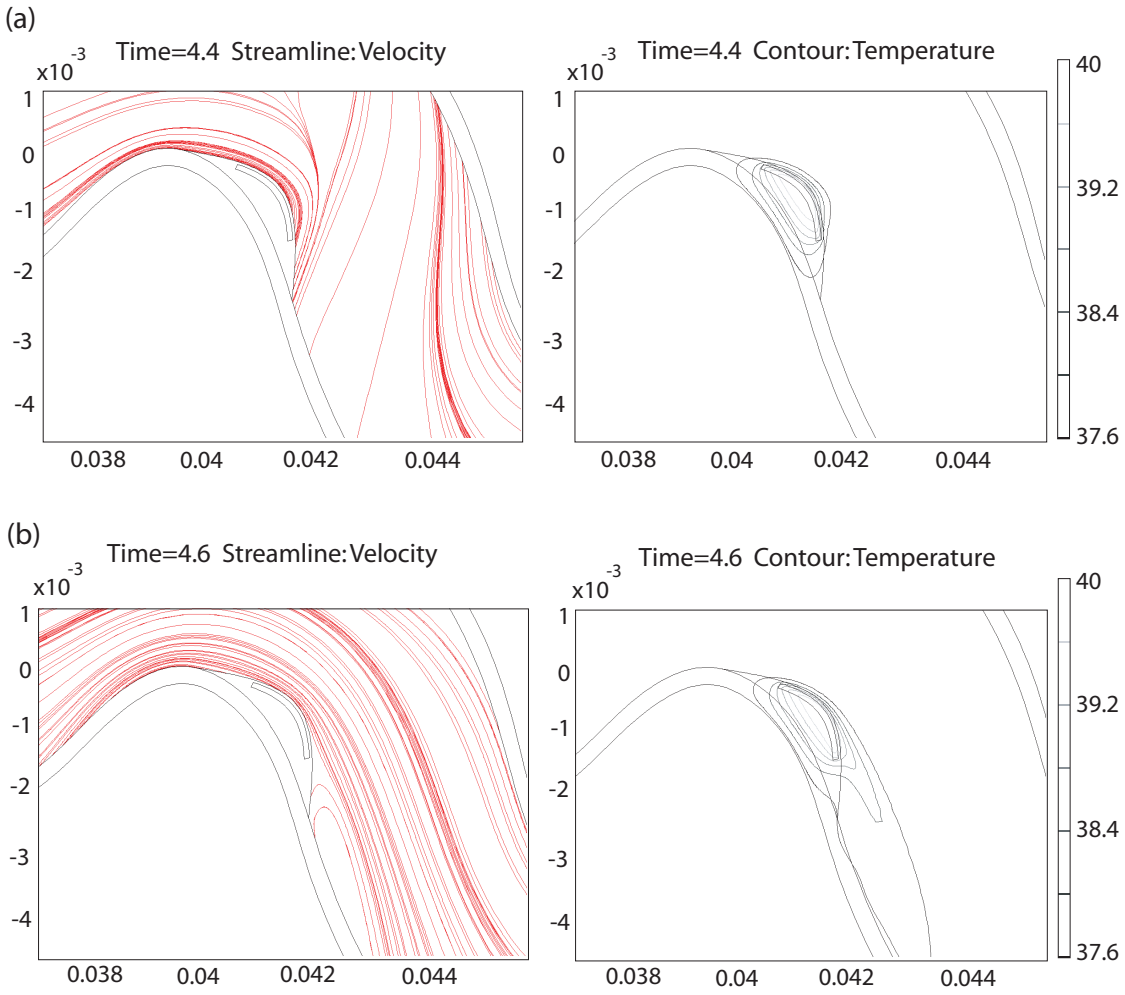

Fig. 34. Streamlines (left) and temperature contours (right) around an inflamed plaque in bending artery. Times **(a)** $t = 4.4$, and **(b)** $4.8s$ are selected during the cardiac cycle (Figure 25b). The dimensions of plaque are $l_{mp} = 1,500$, $d_{mp} = 100$, $d_p = 540$, and $l_f = 50\ \mu m$, and the metabolic heat production is $\dot{q}_m = 0.1\ W/mm^3$.

symmetric. Meanwhile, the streamlines at $t = 4.8s$ show the flow separation at the rear side of plaque and it makes a significant variation of temperature contours. At the plaque surface, the temporal and spatial temperature changes are observed, which are correlated with the occurrence of flow separation due to the characteristics of inlet pulsatile flow and arterial geometries. At $t = 4.4s$, the temperature of the blood surrounding the plaque only changes 0.1 ^oC in a small region that does not extend beyond the macrophage layer length and separates up to 0.16 mm from the plaque surface. Meanwhile, the temperature contour at $t = 4.6s$ show significant difference in the regions where the blood temperature surrounding the plaque is affected; such changes are correlated with the occurrence of flow separation. For $t = 4.6s$, the temperature contours for for $T = 37.6$ ^oC separates from the plaque surface 0.12 mm at the plaque center, and the blood temperature variations are observed 4.5 mm from the plaque center and until about 1 mm away from the plaque/lumen surface. The calculations are performed with the following dimensions of plaque; $l_{mp} = 1,500$, $d_{mp} = 100$, $d_p = 540$, and $l_f = 50$ μm, and a metabolic heat production of $\dot{q}_m = 0.1$ W/mm^3.

According to Figures 26 - 28, constant temperature region is observed between $l/l_p = 0.6$ and 0.7 during a cardiac cycle, where there is the effect of flow instabilities such as flow separation, transition (decreased flow separation) and no flow separation. At the presence of flow separation (at t=4.0, 4.6, 4.8 and 5.0s), the constant temperature region is located between separation point ($l/l_p = 0.61$ to 0.67) and the maximum temperature difference ($l/l_p = 0.74$). At the transition at $t = 4.2s$, the maximum temperature difference is moved between $l/l_p = 0.6$ and 0.7, where the temperature is decreased to keep the constant temperature. At that time, the flow separation is decreased for the separation point to be occurred at the very far edge of the plaque ($l/l_p = 0.83$). At $t = 4.4s$, the flow separation is disappeared, and the

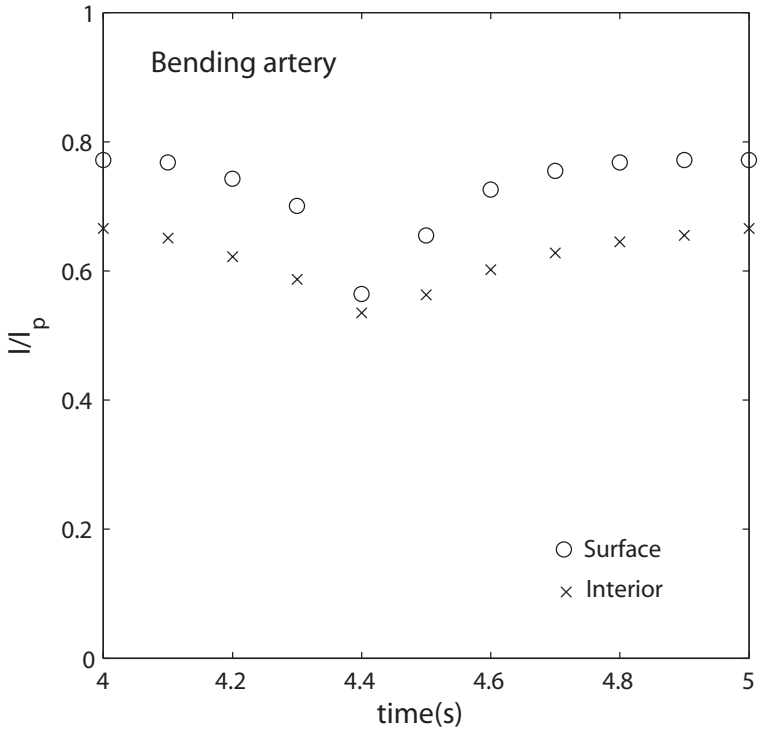

Fig. 35. Movement of maximum temperature points at plaque surface and interior of bending artery during a cardiac cycle. The dimensions of plaque are $l_{mp} = 1,500$, $d_{mp} = 25$, $d_p = 540$, and $l_f = 50$ μm, and the metabolic heat production is $\dot{q}_m = 0.1$ W/mm^3.

constant temperature region is observed right after the maximum temperature region ($l/l_p = 0.5$). Thus, it is observed that the constant temperature is occurred at the region between $l/l_p = 0.6$ and 0.7, regardless of the presence of flow separation.

Figure 35 shows the movement of maximum temperature points at the plaque surface and the interior of bending artery during a cardiac cycle. The maximum temperature difference in the plaque interior shows the characteristics of inlet pulsatile flow, as the temperature at the plaque surface is varied by the inlet pulsatile flow (Figures 26 - 28). The maximum temperature at the plaque surface are observed between $l/l_p = 0.56$ and 0.78. In the interior, the maximum temperature points are occurred inside the macrophage layer between $l/l_p = 0.52$ and 0.67. During a cardiac cycle, the maximum temperature points at the plaque surface are observed approximately $l/l_p = 0.1$ away from the points in plaque interior due to the effect of blood flow. Meanwhile, at $t = 4.4s$, the maximum temperature points at the plaque surface and interior are most closely located around the center of plaque (at $l/l_p = 0.56$ and 0.52) after disappearing of blood flow effect.

In Figure 36, the arterial bifurcation shows the streamlines and temperature contours at two different times during the cardiac cycle ($t = 4.4$ and $4.8s$). $t = 4.4s$ is selected to present the effect of the strongest forward flow during the cycle (Figure 25). In Figure 36a, the flow circulation at the anterior region of plaque is observed in the streamlines at $t = 4.4s$. The boundary layer of blood flow is slightly passed over the middle region of plaque and the convective cooling effect of blood flow influences over the region. Whereas, the front and rear regions of plaque are not affected by the convective blood flow, but by flow circulation due to the effect of arterial geometry. Regardless the change of inlet pulsatile flow, at $t = 4.8s$, the effect of flow circulation is remained at the front and rear regions of plaque. Also, the cooling effect of blood flow also affect the heat transfer at the middle region of plaque. It is observed that,

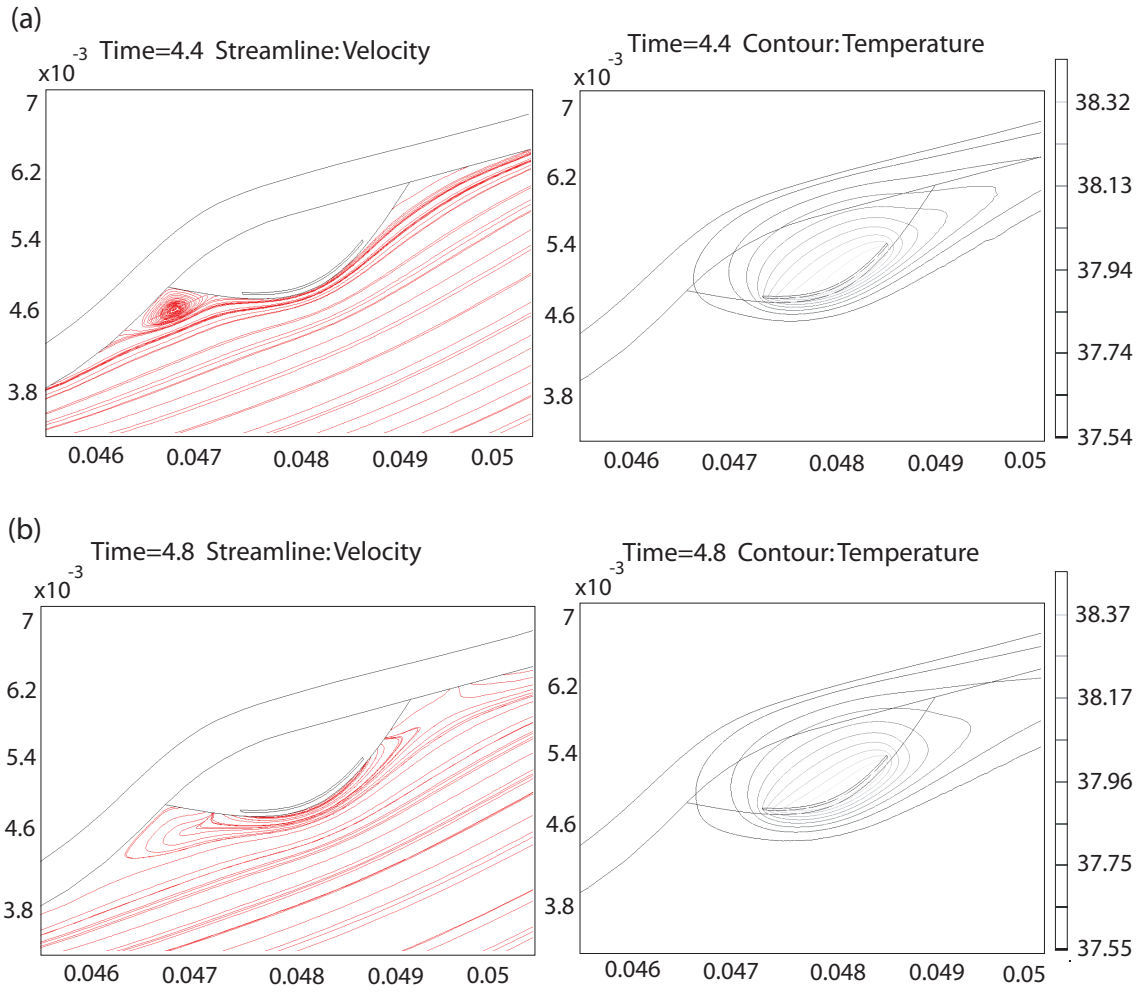

Fig. 36. Streamlines (left) and temperature contours (right) around an inflamed plaque in arterial bifurcation. Times **(a)** $t = 4.4$, and **(b)** $4.8s$ are selected during the cardiac cycle (Figure 25c). The dimensions of plaque are $l_{mp} = 1,500$, $d_{mp} = 25$, $d_p = 670$, and $l_f = 50$ μm, and the metabolic heat production is $\dot{q}_m = 0.1$ W/mm^3.

during the cardiac cycles, AWT of arterial bifurcation is not affected by the inlet pulsatile flow but by the arterial geometry.

4. Conclusions of 2-D unsteady blood flow

In 2-D unsteady calculations, AWT distribution was determined during a cardiac cycle, and the results of steady and transient temperature calculations were compared.

It was observed that **(1)** the parameters more influencing over the plaque temperature were the macrophage layer thickness d_{mp} and the metabolic heat q_m, and **(2)** the macrophage layer thickness d_{mp} and the maximum plaque temperature ΔT_{max} were linearly related, had already observed in the steady case as well as in the experimental studies.

The unsteady calculations also showed that the locations of the hot spot resulting from inflammation are dependent on the inlet pulsatile flow pattern, and ΔT_{max} were generally located behind the apex of the plaque. The exact locations and temperature magnitude depended on arterial geometry, flow velocity, presence of flow separation and recirculation, and the extension of the macrophage layer. The particular locations presenting larger temporal temperature variations were different from each artery because the particular conditions of arterial geometries and inlet blood flow contribute to the blood flow characteristics during the cycles.

From the results, the best location to measure plaque temperature in the presence of blood flow might be recommended between the middle and the far edge of the plaque with the reasons: **(1)** the maximum temperature would occur in that region and **(2)** the temperature at the plaque lumen interface would vary significantly less in such region. Based on this observation, the sampling rate and measuring distance of AWT measurements around the plaque region might be determined as follows: **(1)** temperature measurements performed to determine plaque temperature should

be performed in at least 2 locations including mid and rear regions during a couple of cardiac cycles, **(2)** direct measurements of AWT should be taken very close to the plaque/lumen surface, as blood temperature fell to normal body temperature within 100 μm away from the plaque surface.

As the result, it was said that transient temperature variation at the plaque/lumen interface was different depending on the arterial geometry and the velocity waveform, and that to have representative local temperature measurements, the temperature should be recorded in the same location over at least one cardiac cycle.

C. 2-D Plaque Temperature during Blood Flow Reduction

The transient temperature variation during blood flow reduction and blood flow interruption is studied to look at the thermal effect of a catheter introduction. These measurements using catheters are subjected to large errors due to the cooling effect of blood flow and imperfect contact between sensor and plaque surface. It was observed that the variations of temperature detected in vivo were less than in ex vivo studies [12, 13, 75], or the temperature in significant lesions was not detected or recorded with trivial changes [13].

Currently, the clinical research groups studying AWT [20, 21] have divergent opinions about the factors that affect the temperature measurement and other parameters that affect the temperature measurement. Stefanadis *et al* [21] showed that arterial wall temperature seems to vary linearly with blood flow velocity; particularly, in the range of 6 to 15 cm/s the temperature is inversely proportional to the average peak velocity ($p = 0.05$ and $R = 0.46$). On the other hand, Diamantopoulos *et al* [20] reported that flow velocity and arterial wall temperature show a logarithmic relationship where the maximum plaque temperature becomes independent of blood

velocity above 5 cm/s. Numerical study of the effect of flow reduction while measuring arterial wall temperature can help to clarify divergent opinions from experimental studies on the relationship between blood velocity and plaque temperature.

Previous sections of steady and unsteady blood flow calculations have indicated the relationship between arterial wall temperature and flow characteristics as well as plaque and arterial geometries. Numerical results showed that plaque temperature increase correlates positively to macrophage cell density and layer thickness, whereas plaque temperature varies inversely with the depth of macrophage cell layer as seen experimentally. In our studies published [76, 77, 78], it was observed that temperature measurement should be performed in the downstream edge of the plaque, and that the presence of recirculation near the plaque is followed by an increase in surface temperature. The models provide a way of estimating the location of maximum temperature, its displacement during the cardiac cycle and the local temperature variation.

The calculations presented in this section aim to provide information of alterations in the arterial wall temperature during different levels of vascular occlusion or blood flow reduction in the arteries under consideration. This study analyzes the transient temperature variation in the plaque surface when blood flow is reduced. The reduction in arterial blood flow is assumed to be the result of catheter introduction, as observed by the clinical research groups [16, 20, 21] using a balloon-thermography catheter to measure arterial wall temperature.

The present work extends previous sections by looking at the effect of transient blood flow reduction in addition to arterial geometry and plaque composition. These new calculations are important to the field of arterial wall thermography as they serve to understand the relationship between arterial wall temperature and flow reduction due to catheters used to measure local temperature.

1. Blood flow and thermal analysis

In this study, the reduction model of inlet blood flow is proposed; the blood flow is gradually reduced as a result of the introduction of catheter in the blood vessel, which was observed by the clinical research groups [16, 20, 21] using a balloon-thermography catheter to measure arterial wall temperature. The calculations serve to clarify observation and interpretation of temperature profiles during blood flow reduction. Two arteries, a straight stenotic and a bending artery, in Figure 9, are analyzed using the Navier-Stokes equations and the energy equation (3.7) with the same boundary conditions except the different inlet blood flows considering vascular occlusion. The same material parameters are applied from I.

At the vessel inlet ($\ell = 0$) as shown in Figure 9, a uniform velocity profile with a pulsatile waveform as a function of time (Figure 37) is used

$$u = u(t) \quad \text{at} \quad \ell = 0. \tag{3.18}$$

where the waveform function $u(t)$ shows the normal and reduction of the cardiac cycles for both arteries during *cycle 1* through 6. Figure 37 indicates the gradual reduction of blood flow, and shows three different flow stages during the period the calculations were performed. The stages correspond to: **(1)** a normal pulsatile blood flow using the waveforms described previously, **(2)** a rapid and moderate reduction of inlet velocity to 50%, and **(3)** a significant occlusion of blood flow up to 5%. *Cycle 1* through 3 present stage 1, *Cycle 4* shows the rapid reduction in blood flow during stage 2, and during *Cycles 5* and 6, the blood flow is occluded to 10 and 5%, respectively. Using such temporal reductions in blood flow, the plaque temperature is calculated to study the cooling effect of blood flow.

For the thermal model, $\dot{q}_m = 0.1\ W/mm^3$; the value selected for $\dot{q}_m$ is able to

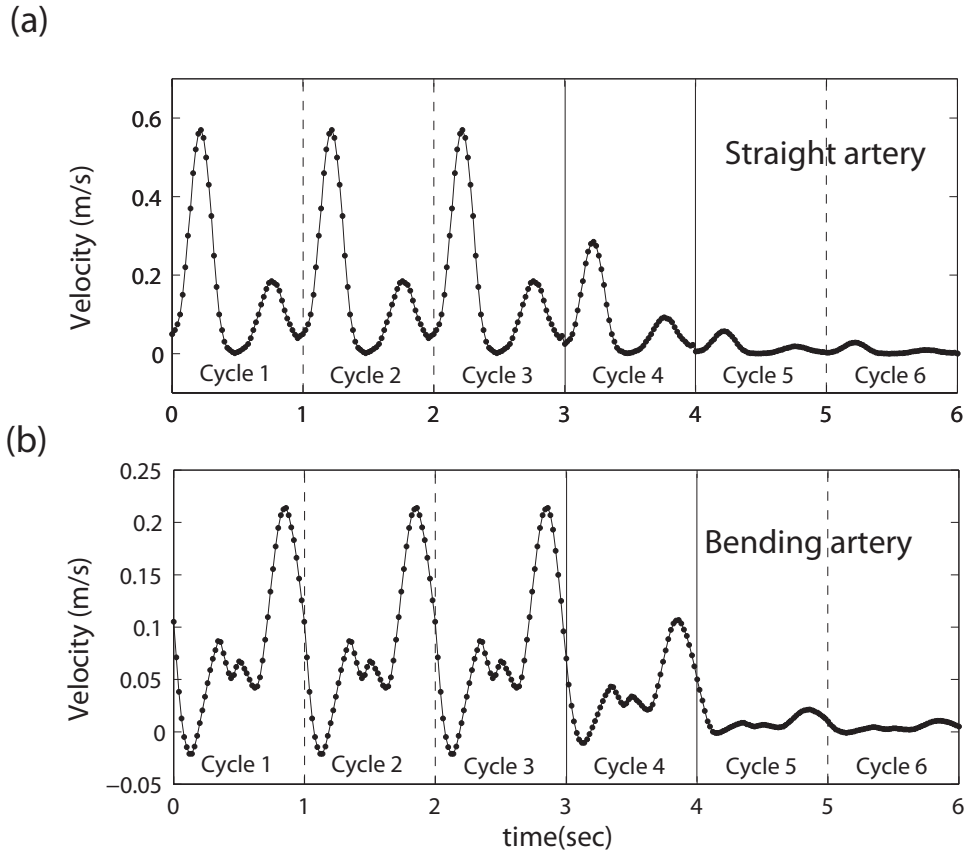

Fig. 37. Pulsatile flow waveform with vascular occlusion after *Cycle 3*. The normal cardiac cycles of **(a)** a straight stenotic artery [72] and **(b)** a bending artery [59] are modified for the occlusion of blood flow.

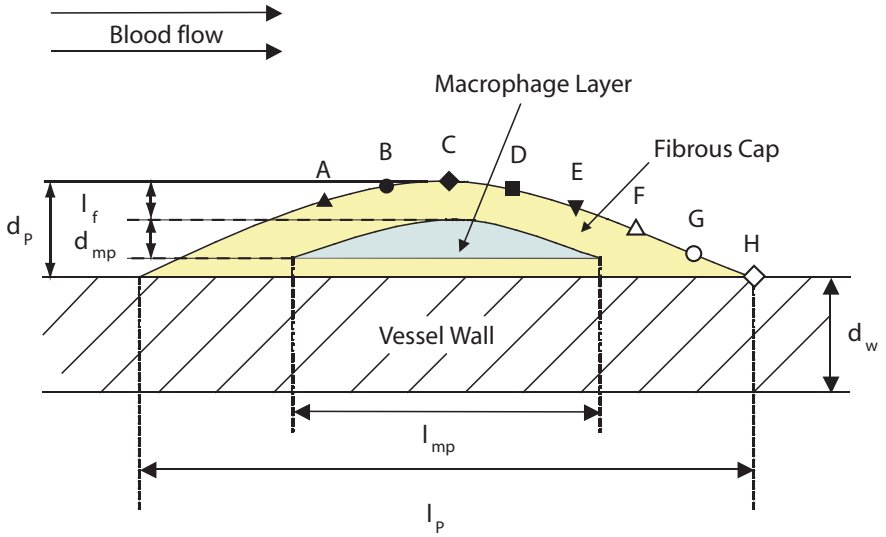

Fig. 38. The location $x_i = x/l_p$ of eight different observation points on the plaque surface. Point **A** corresponds to the front of the plaque ($x_A = 0.3$), point **C** presents the center ($x_C = 0.5$); point **E** is defined at $x_C = 0.7$; and point **H** is the ending point of the plaque ($x_H = 1$).

reproduce thermal inhomogeneities of 0.4 to 2.2 ^oC reported by direct measurement [12, 14, 15]. The details on the factors affecting $\dot{q}_m$, as well as the values observed in different active cells were discussed in the previous section of 2-D steady blood flow. The boundary conditions and material properties applied for energy equation (3.17) are the same as those of the unsteady blood flow case.

2. Results of blood flow reduction

As blood flow is reduced, the variations of temperature distributions are presented at the lumen surface. The cooling effect of blood flow is determined by calculating Nusselt number, and the temperature histories are presented at representative points A through H in Figure 38.

a. Effect of flow characteristics

This section introduces the change of flow characteristics and temperature distribution before and after the blood reduction. In order to compare the changes of flow and temperature, two representative times during the normal cycles (Figure 39a) and two times during the occlusion cycles (Figure 39b) are selected, respectively.

For the straight artery in Figure 39, $t = 2.3$, $2.8s$ and $t = 5.3$, $5.8s$ are selected for the normal and occlusion cardiac cycles, respectively, which are able to most distinctly present the characteristics of the inlet pulsatile flow. Compared between Figure 39a and Figure 39b, the streamlines show no difference of flow characteristics before (at $t = 2.3$ and $2.8s$) and after (at $t = 5.3$ and $5.8s$) the occlusion of blood flow. Before the blood occlusion, the temporal temperature changes during the normal cycles are occurred by the characteristics of inlet pulsatile flow. The temperature contours at $t = 2.3s$ shows more convective cooling effect led by the stronger blood flow. After the occlusion, the characteristics of inlet pulsatile flow is suddenly reduced and the temporal temperature change is disappeared at $t = 5.3$ and $5.8s$.

In bending artery (Figure 40), $t = 2.4$ and $2.8s$ for the normal cycle and $t = 5.4$ and $5.8s$ for the occlusion cycle are selected to present the characteristics of the inlet pulsatile flows. As shown in Figure 40a, at $t = 2.4s$, blood flow does not show the presence of a recirculation region in the downstream part of the plaque, which produced symmetric temperature contours near the plaque region. At $t = 2.8s$, on the other hand, one sees the appearance of recirculation due to the temporal increase of the inlet flow or the stronger forward blood flow. Appearance of the flow separation in the rear region of plaque increases the residence time of the blood in that region, reducing the cooling effect of blood, and producing asymmetric temperature contours. From the observation of Figure 40, it is concluded that during the normal

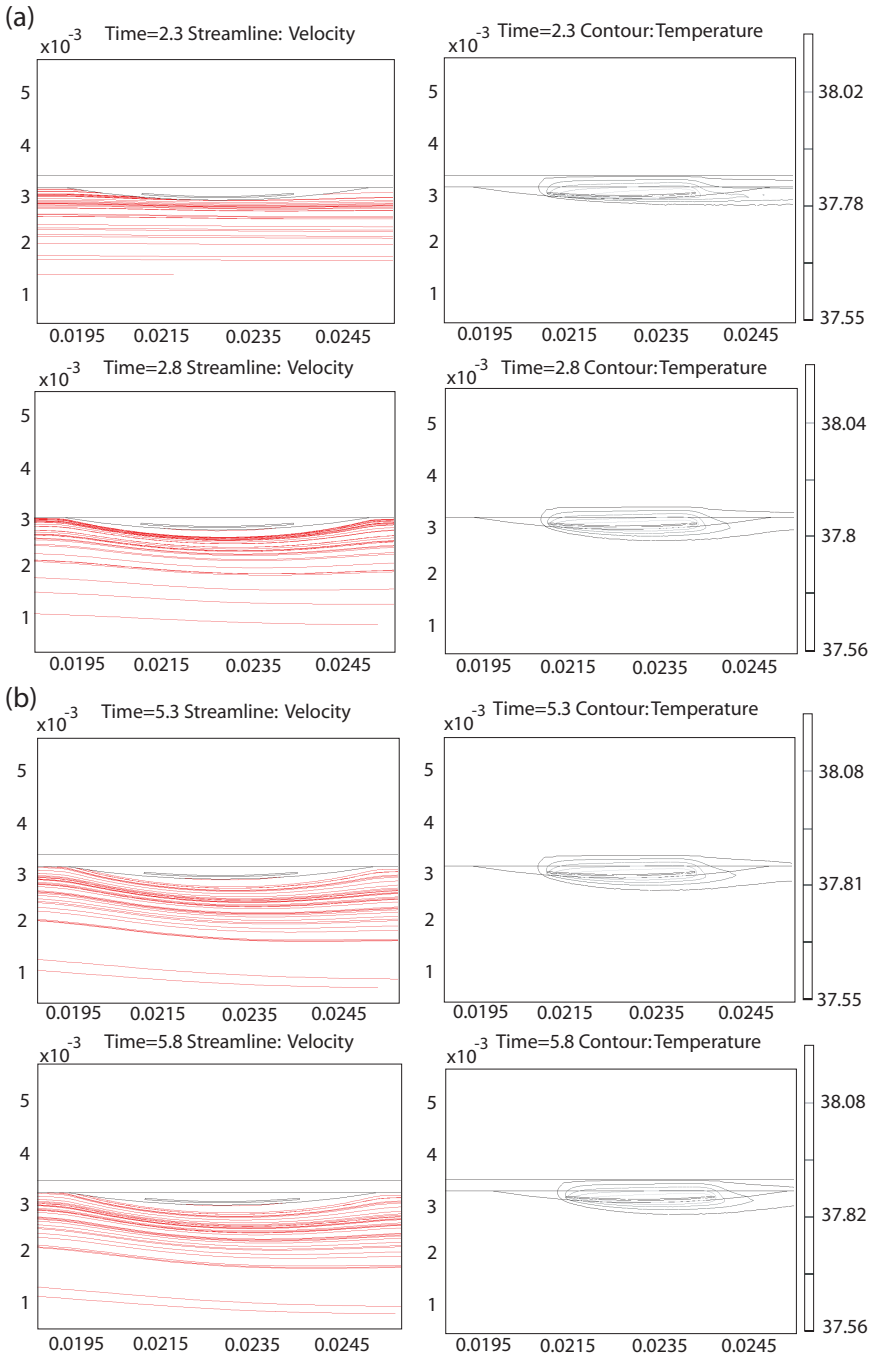

Fig. 39. Streamlines (left) and temperature contours (right) around a plaque in straight artery. The lines correspond to **(a)** $t = 2.3$ and $2.8s$ for normal cycles, and **(b)** $t = 5.3$ and $5.8s$ after blood reduction to 5% of normal cycles.

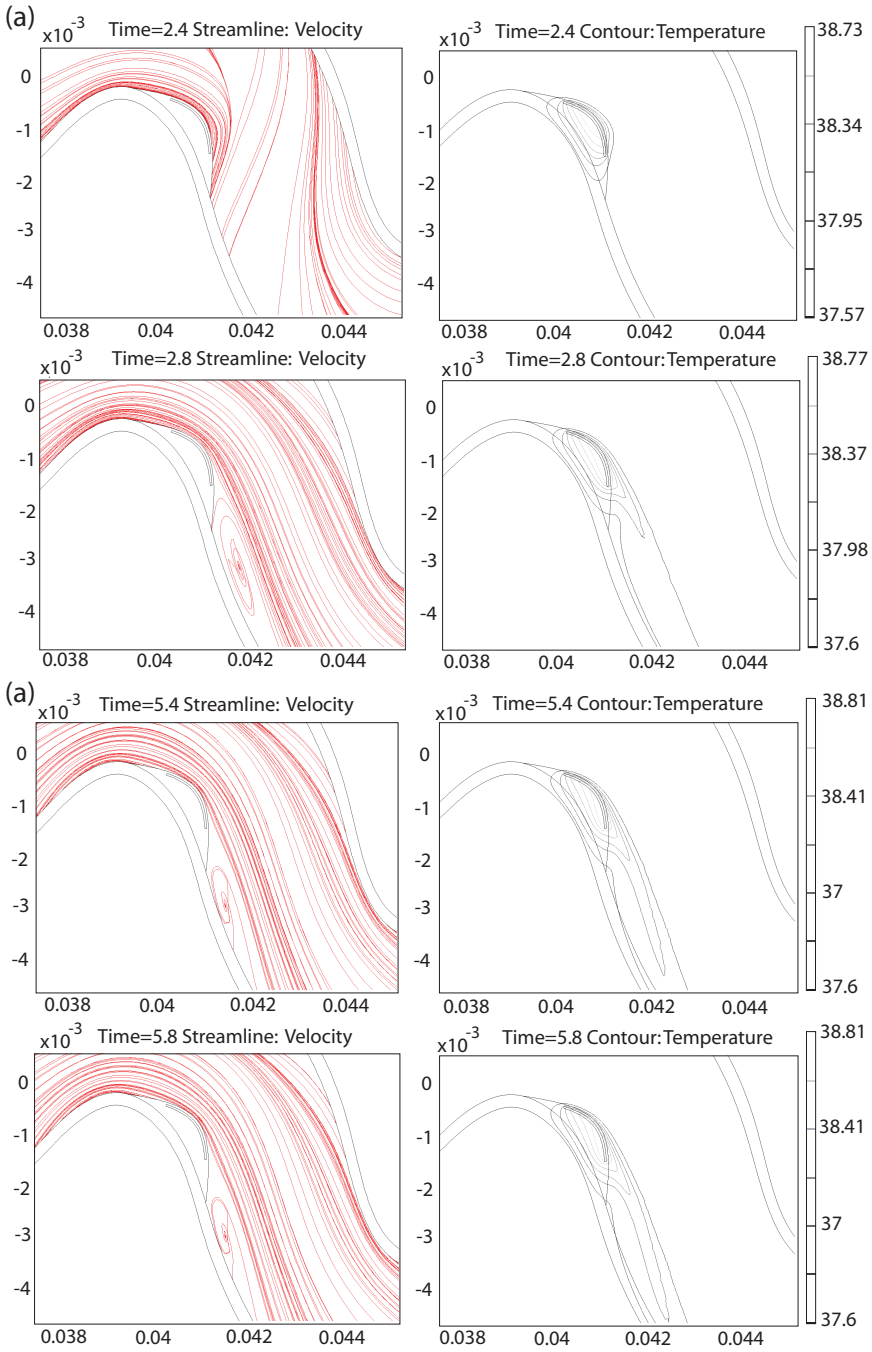

Fig. 40. Streamlines (left) and temperature contours (right) around a plaque in bending artery. The lines correspond to **(a)** $t = 2.4$ and $2.8s$ for normal cycles, and **(b)** $t = 5.4$, $5.8s$ after blood reduction to 5% of normal cycles.

cycles (*i.e.* when normal inlet velocity is considered), the temperature distribution strongly depends on the characteristics of the flow, and the rate of cooling by the blood flow is directly related to the characteristics of the inlet pulsatile flow. After the blood flow is substantially reduced (Figure 40b), the flow patterns at $t = 5.4$ and $5.8s$ do not change significantly. Due to the small volume of blood flow in the system, the recirculation observed is decreased compared to that observed during the normal cycle (at $t = 2.8s$ in Figure 40a). Because of the small volume of flow, the temperature contours show the same asymmetric pattern at both times $t = 5.4$ and $5.8s$. Compared with the temperature contours during normal cycles shown in Figure 40, temperature increases at the end of the plaque. The reduced blood flow during the occlusion cycles decreases the convective cooling effect from the surface to the luminal blood flow.

b. Temperature along the plaque surface

As observed previously, during normal pulsatile flow the magnitude and location of the hot spot indicated by $\Delta T_{max} = T(r,t)_{max} - T_a$ is directly affected by the characteristics of inlet flow as well as the vessel geometry. Looking at the temperature distribution at the plaque surface or plaque/lumen interface, it is seen that in the presence of pulsatile blood flow, three main thermal regions are observed: a front region, a middle region and a rear region. These regions are indicated by points **A** through **H** shown in Figure 38. Points **A** through **C** delimit the front region of the plaque, and point **C** corresponds to the center of the plaque, point **E** presents the ending point of the middle region, point **F** is the beginning point of the rear region, and point **H** is the ending point of the plaque.

Figure 41 indicate the snapshots of temperature change ΔT along the plaque/lumen interface for both arteries at different times ($t = 0.1$, 0.4, 0.6 and $0.8s$) into each cycle

(*Cycle 3* through *Cycle 6*). The vertical lines indicate the locations of the observation points **A** through **H**, as described in Figure 38. In these plots, the horizontal axis coincides with the base of the plaque, and the temperature at the plaque/lumen interface is plotted with respect to the horizontal location of the observation points. In order to compare the temperature distribution at the plaque/lumen interface of the two arteries, the horizontal position is divided by the plaque length (l_p).

For the stenotic straight case (Figure 41a), during normal blood flow (*Cycle 3*) the maximum temperature occurs at point **E** (near the rear region of the plaque); as the blood flow is reduced during *Cycle 4* through *Cycle 6*, the temperature at the plaque/lumen interface raises at every point, and point **E** still corresponds to the point showing the maximum temperature increase. During blood flow reduction from *Cycle 3* to *6*, the plaque region where the maximum temporal temperature variation is recorded during blood flow reduction is the front region of the plaque between points **A** and **E**. After reducing the blood flow, the temperature rise produces a symmetric temperature distribution with respect to the macrophage layer location compared to the distribution observed during normal blood flow (*Cycle 3*). Figure 41b shows the plaque/lumen temperature increases at the far edge (point **E** to **H**) of the plaque, but decreases at the middle edge between points **A** and **C** as blood flow is reduced, which is distinctly shown at $t = 0.4$. After blood flow reduction, the temperature at the plaque/lumen surface develops a maximum at the end of the macrophage layer and the temperature distributions keep the constant shape regardless of any second of cycle. It is observed that flow instabilities such as flow separation are removed at the rear region as the blood flow decreases.

To analyze the convective heat transfer at the plaque surface, the local Nusselt number Nu_x is calculated along the plaque/lumen interface and is shown in Figs. 42 for the straight and bending artery, respectively. The Nusselt number is calculated

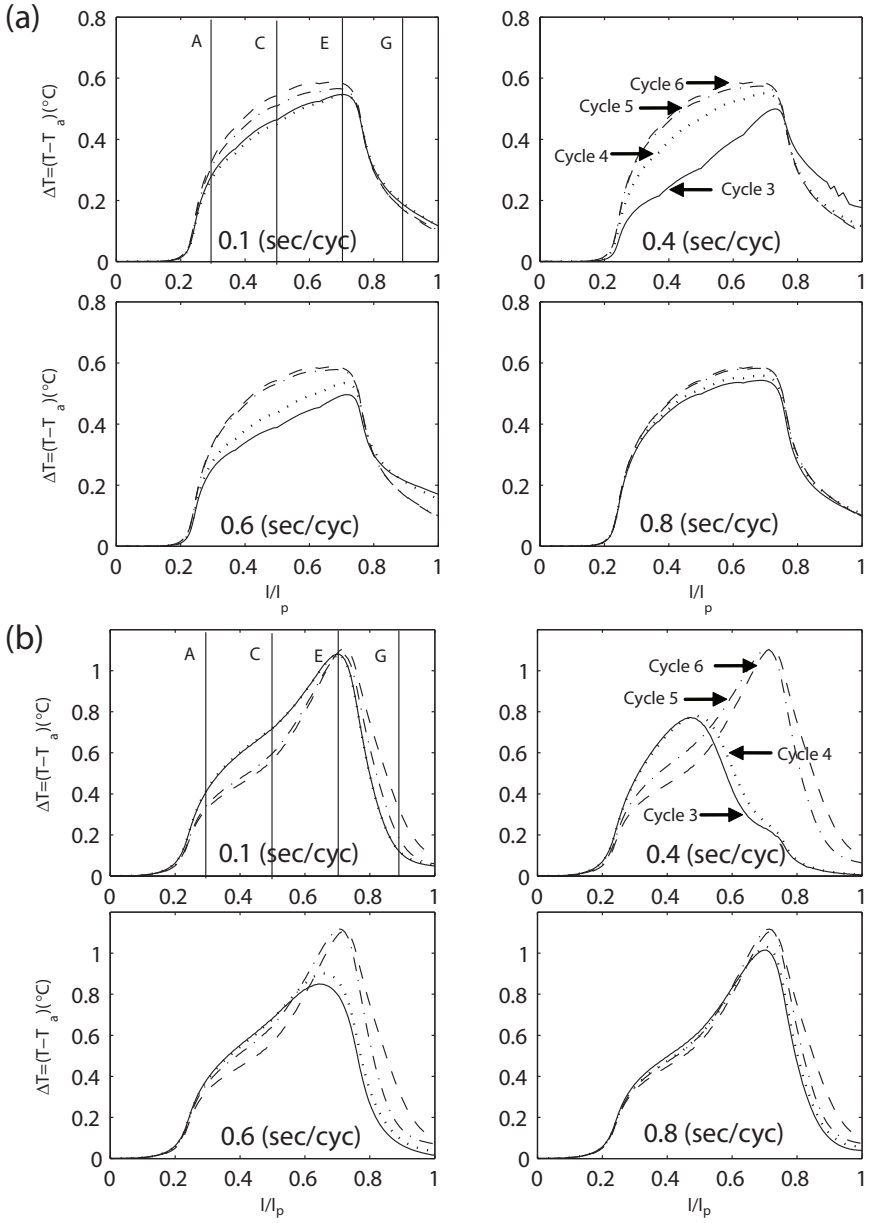

Fig. 41. Transient temperature distribution at the plaque/lumen interface for **(a)** straight artery and **(b)** bending artery at different cycles. The temperature variation is produced by reduction in blood flow velocity as indicated in Figure 37. The times are 0.1 to 0.8s offset into each cycle, which correspond to $t = C.1$, C.4, C.6 and $C.8$s, where C is the cardiac cycles (C =3, 4, 5 and 6).

for different times ($t = 0.4$ and $0.8s$ in each cycle) during *Cycle 3* through *Cycle 6*. During normal blood flow, the Nusselt number presents significant variation along the plaque surface. In both vessels, the Nusselt number is reduced in magnitude after blood flow reduction as expected.

In the straight artery (Figure 42a), Nu_x is maximum at the front edge of the plaque, which explains the lower temperature observed at that region due to the stronger cooling effect. For the bending artery (Figure 42b), Nu_x presents drastic variations during *Cycle 3* and *Cycle 4* because the behavior of the inlet flow characteristics forms the flow instabilities such as flow separation combined with geometry effect. The instabilities lead to a strongly disturbed flow which contributes to the local convective heat transfer in the plaque region. After blood flow reduction (*Cycle 5* and *Cycle 6*), the local Nusselt number gradually increases at the regions between $l/l_p = 0$ and 0.5 producing the temperature drop registered at the front region.

The stationary Nu_x values obtained after *Cycle 4* present two peaks (at $l/l_p = 0.25$ and 0.75) that correlate with the boundaries of the macrophage layer; a maximum is observed at the front edge (point **A**), and a minimum occurs at the rear edge (point **F**).

c. Temperature history at representative points

Figure 43 shows the temperature history of points **A** through **H** indicated in Figure 38; these figures indicate how the temperature at the representative points of the plaque surface changes after blood flow is reduced (*Cycle 4*). The plaque surface temperature of each point becomes stable after 3 cardiac cycles. The temporal temperature changes registered during the cardiac cycle are between 0.1 and 0.2 ^oC for the straight artery and between 0.1 and 0.6 ^oC for the bending artery, as seen during *Cycle 2* and *Cycle 3*. It is observed that blood flow reduction has different effects on the front, middle

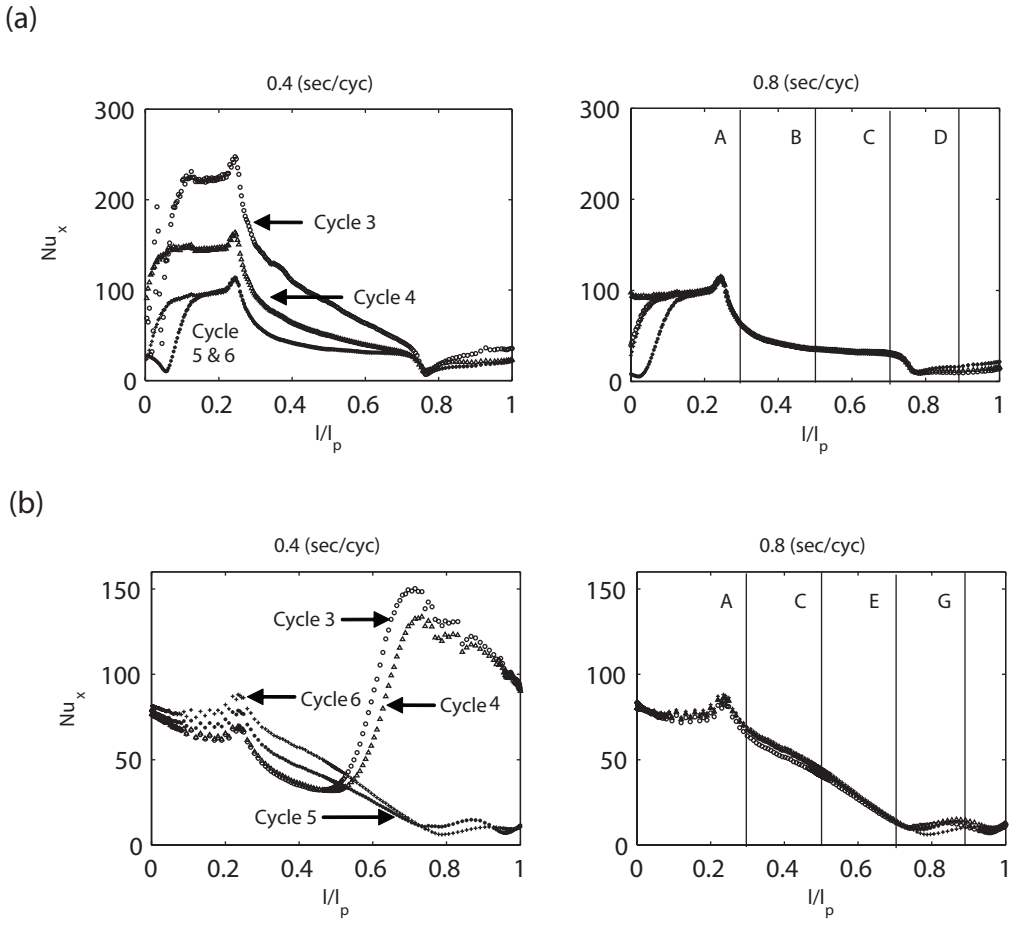

Fig. 42. Nusselt number variation along the plaque/lumen interface for **(a)** a stenotic straight artery and **(b)** a bending artery calculated during *Cycle 3* through *6*.

and rear regions of the plaque; those effects are combined with the arterial geometry.

d. Comparison of temperature calculations and AWT measurements

The calculations presented here were designed to verify if the relationship between maximum temperature and blood velocity followed a logarithmic trend as observed by Diamantopoulos *et al* [20], or a linear trend as reported by Stefanadis *et al* [21].

Figure 44 shows the relationship between the average peak velocity and the maximum temperature difference experienced at the plaque/lumen interface of the straight artery and bending artery during gradual flow reduction. The calculations were performed at steady blood flow in each artery. The dimensions of plaque are $l_{mp} = 3,335$, $d_{mp} = 50$, $d_p = 500$ and $l_f = 25\ \mu m$ for a straight artery, and $l_{mp} = 1,500$, $d_{mp} = 50$, $d_p = 540$ and $l_f = 50\ \mu m$ for a bending artery, respectively. For the straight artery in Figure 44a, the blood flow was reduced from 15 to 0.001 cm/s by the variation of inlet flow. The maximum temperature difference was steadily increased to 2.1 ^oC as blood flow was reduced to 2 cm/s. The temperature was rapidly increased to 4.8 ^oC until the inlet velocity reached for 0.01 cm/s after 2 cm/s, where the cooling effect of blood flow seemed to be disappeared. In the bending artery (Figure 44b), the maximum temperature increases with the same pattern as the case of a straight artery. The velocity of an inlet blood flow was decreased from 10 to 0.001 cm/s. As blood flow was reduced to 2 cm/s, the maximum temperature difference was steadily increased to 1.23 ^oC. After that, the temperature was rapidly increased to 3.2 ^oC at 0.01 cm/s.

A regression analysis shows that the relationship between maximum temperature change and average blood velocity satisfies closely a logarithmic trend of the form $\Delta T_{max} = A \ln(V) + B$. Using the calculated ΔT_{max} for a range of velocities, the

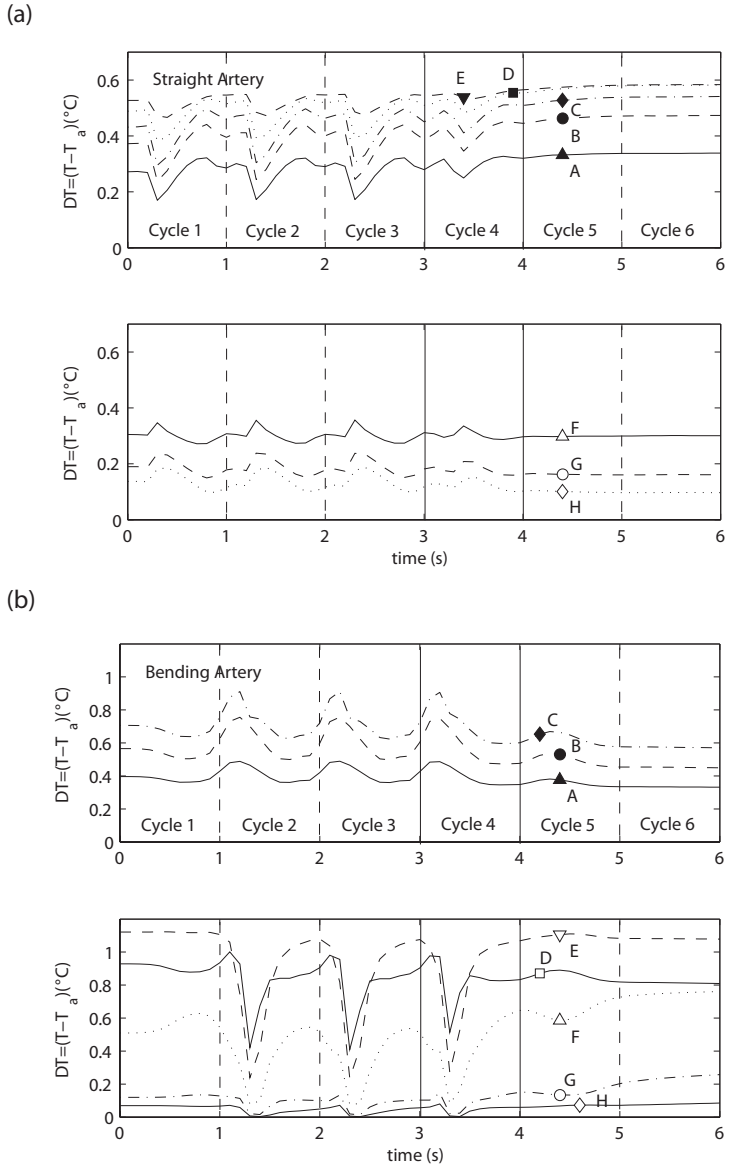

Fig. 43. Time variation of temperature calculated at different points along the plaque/lumen interface for **(a)** a stenotic straight artery and **(b)** bending artery. The inlet velocity profiles are given in Figure 37, and the points where the temperature is recorded correspond to points **A** through **H** indicated in Figure 38.

fit generates the following values of the coefficients: $A = -0.5022$, $B = 0.1774$ and $R^2_{\ln(V)} = 0.999$ for the straight artery, and $A = -0.2889$, $B = 0.2498$ and $R^2_{\ln(V)} = 0.9496$ for the bending artery, respectively. According to [20], the maximum plaque temperature is not affected when V is larger than 5 cm/s, and our calculations reproduce that trend.

The mathematical model is able to predict qualitatively the temperature response and its relationships with velocity as indicated by experimental studies. A complete validation cannot be performed because, the experimental arterial wall temperature studies [20, 21] do not provide details about plaque and vessels size or the locations where temperature sensors were placed; quantities that are proven to affect the plaque temperature value significantly [77, 78].

3. Conclusions of 2-D blood flow reduction

The calculations presented herein aimed to provide information of alterations in the arterial wall temperature during different levels of vascular occlusion or blood flow reduction in the arteries under consideration. Using the numerical model, this section presented plaque temperature calculations to determine the cooling effect of blood flow during arterial blood flow reduction.

During normal pulsatile flow, the characteristics of the inlet flow dominated the convective cooling effect on the plaque/lumen surface and caused considerable variation of temperature along the plaque surface in space and time. The strong forward flow motion of each artery was able to increase the rate of heat transfer between the plaque/lumen surface and the blood flow. In particular, for bending artery, the momentum effect of blood flow was combined with the geometry effect of bending artery as well as the inlet flow waveform function, which caused the flow instability such as recirculation and flow separation. The calculations presented here indicated that

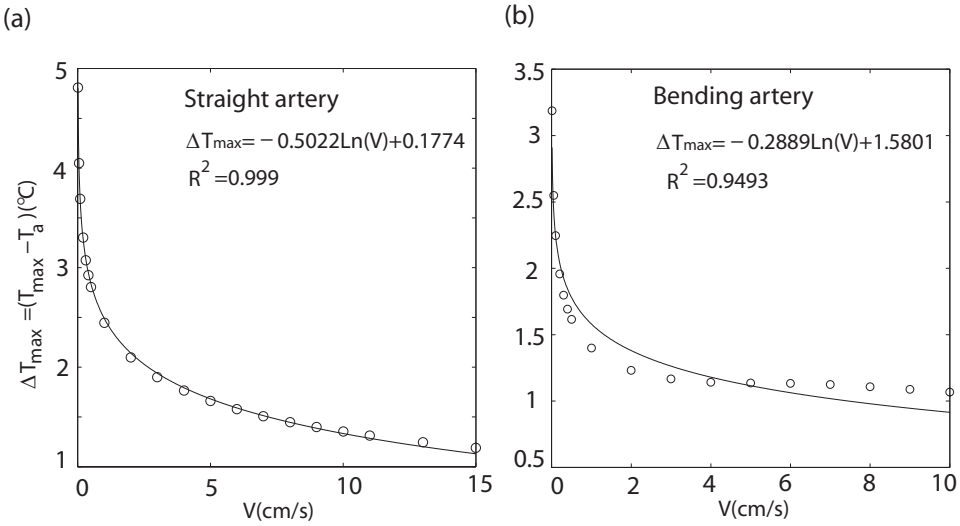

Fig. 44. Relationship between average velocity and maximum temperature difference at the plaque/lumen interface in **(a)** the straight artery and **(b)** the bending artery. The dimensions of plaque used are $l_{mp} = 3,335$, $d_{mp} = 50$, $d_p = 500$ and $l_f = 25\ \mu m$ for a straight artery, and $l_{mp} = 1,500$, $d_{mp} = 50$, $d_p = 540$ and $l_f = 50\ \mu m$ for a bending artery, respectively. For the metabolic heat generation, $\dot{q}_m$ of 0.1 W/mm^3 is applied in steady flow. The solid line corresponds to filled curve using linear least squares procedure.

blood flow effectively transported thermal energy by virtue of its unstable nature. The convective heat transfer by the cooling effect of blood flow was more actively registered at the rear region of plaque.

As the blood flow was reduced, the convective cooling effect decreased on the plaque/lumen surface and the plaque temperature increased. The temperature distribution became dependent of arterial geometry only. It should be considered that blood flow reduction provided different effects on the front, middle and rear regions of the plaque; those effects varied with the arterial geometry. The reduction in Nusselt number indicated that the cooling effect of blood flow was decreased and the variation of non-uniform temperature increase, which ranged from 0.1 to 0.25 ^oC for the geometries considered. Consequently, blood flow reduction contributed to the increase of plaque surface temperature and the minimum required reduction time needed to observe local temperature increase in the presence of an active plaque was at least 6 seconds.

The present section extended the previous sections by looking at the effect of transient blood flow reduction in addition to arterial geometry and plaque composition. These new calculations were important to the field of arterial wall thermography as they served to understand the relationship between arterial wall temperature and flow reduction due to catheters used to measure local temperature.

D. Analysis of Thermal Stress in 3-D Unsteady Model

This study intends to analyze thermal stress based on the local temperature increase produced by the inflammatory process in atherosclerotic plaques, which contributes to identification of plaque instability and disruption. For the study, 3-D geometrical models of a human artery are used. The arterial geometries present multi-component

plaque structure consisting of lumen, arterial wall and plaque composed of lipid core. The modeling in finite element analysis is performed under non-isothermal conditions considering thermal heterogeneity.

Thermal stress is calculated at the plaque and arterial wall by using structural analysis and incorporating the spatial temperature change as thermal load. Thermal analysis investigates the relations between temperature heterogeneity and thermal stress of plaque, and between the stress distribution and the inlet pulsatile blood flow. This is done to investigate and quantify plaque vulnerability and how plaque temperature contributes to plaque stability. The goal of this section is twofold: **(1)** to demonstrate the investigation of thermal stress in 3-D realistic model of atherosclerotic plaque and **(2)** to improve accuracy of complex plaque vulnerability assessment.

In this section, we calculate thermal stress distributions produced by AWT heterogeneity observed at the plaque/lumen interface when atherosclerotic plaques experience an inflammatory cascade. Thermal stress is calculated performing fluid analysis, heat transfer analysis and structural analysis assuming linear elastic material properties. The procedure consists of two basic steps: (**1**) calculation of velocity profiles and temperature distribution at the domains by solving the Navier-Stokes and energy equations using initial conditions produced by steady calculations and approximated inlet velocity profiles; and (**2**) determination of thermal stress and displacement using the calculated temperature distribution as input thermal loads in structural analysis.

1. Blood flow and thermal analysis

For the blood flow analysis, the incompressible Navier-Stokes equations are used as the governing equations. No slip conditions and natural traction equilibrium conditions are assumed at all interfaces. The velocity profile at the inlet ($\ell = 0$) is assumed

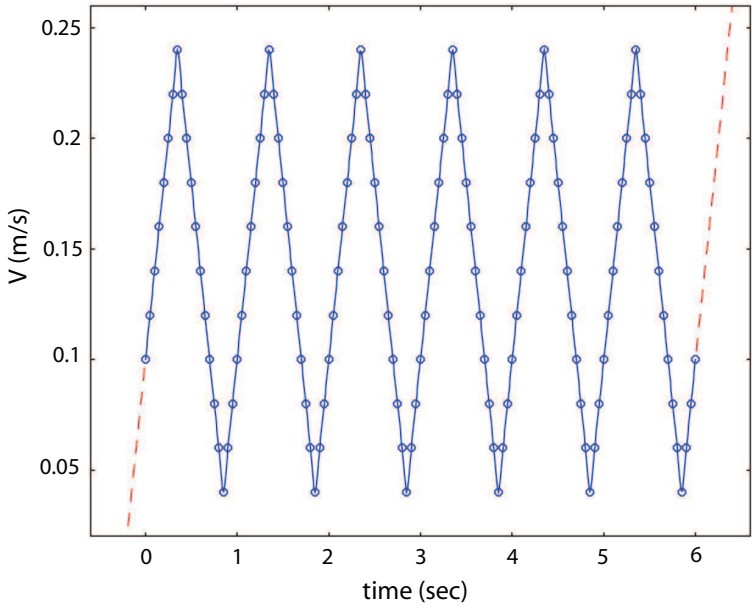

Fig. 45. Simplified pulsatile flow waveform used at the inlet of 3-D realistic model.

to be uniform, $u = u(t)$, with a pulsatile waveform as a function of time. For the simplified model in Figure 10, the inlet pulsatile function used in 2-D straight artery is applied as shown in Figure 25a [72]. Meanwhile, the realistic model (Figure 11) uses the simplified inlet waveform function to perform the efficient calculations in restricted memory, as shown in Figure 45. The velocity profile also contains the periods of rapid acceleration and deceleration to present reverse flow. The waveform function was scaled to yield the mean velocity of 0.15 m/s, the maximum velocity of 0.24 m/s, and the minimum velocity of 0.04 m/s.

For the thermal model, the Energy equation with heat generation term ($\dot{q}_m$) is solved applying the same boundary conditions of 2-D calculations: constant temperature ($T = T_o$) at the external vessel wall ($r = R_o$) due to perfusion at the *vasavasorum*, a fixed blood and tissue temperature ($T = T_o$) at the vessel inlet

($\ell = 0$), and no temperature gradient ($\frac{\partial T}{\partial n} = 0$) at the vessel outlet ($\ell = L$). In the simplified model, the heat generations ($\dot{q}_m$) of 0.1 and 0.05 W/mm^3 are applied to find out the appropriate values to reproduce the temperature variation calculated in 2-D cases. In the realistic model, 0.005 W/mm^3 is selected for the heat generation ($\dot{q}_m$) with the following reasons: **(a)** the size of lipid core is much larger compared to those of 2-D and 3-D simplified models; the length (24 mm)in longitudinal direction is fifteen times longer than 1.6 mm in 3-D simplified model, and **(b)** as the population of macrophage cells increases in such large lipid core, the ability of metabolic activation decreases due to the high competition between the macrophage cells for restricted amount of sources such as oxygen, lipoprotein and debris.

2. Structural analysis

a. Elastic material properties

Arterial wall is structurally divided into three layers: intima, media and adventitia surrounded by the different connective tissues and smooth muscles [79]. This morphological feature of the arterial wall suggests locally anisotropy [1, 79]. On the microscopic level, the arterial wall is heterogeneous because it is comprised of cells, elastin, and collagen, and the distribution of these elements varies from the inner to the outer wall. [79, 91, 92]. However, according to several research groups [80, 81, 82, 83, 84], arterial wall might be considered to be isotropic within the physiological range of deformation. Commonly in the engineering and biomechanics literatures, however, it has been assumed that the global response is orthotropic in the radial, circumferential and axial directions [85, 86, 87, 88], where Young's modulus values are cylindrically different. In this study, arterial wall is assumed to exhibit the cylindrical orthotropic material properties in the directions. We also assumed that the arterial wall is a

linearly elastic homogeneous material (i.e. one Young's modulus) [36, 37, 83, 89, 90].

Atherosclerotic plaques are characterized by the subintimal accumulations of extracellular lipids, fibrous tissue, smooth muscle cells, and calcium [83]; several researches have assumed these layers to be homogeneous at each accumulation [36, 37, 83, 89, 93, 94]. In this study, the plaque is assumed to contain only lipid core, which may have a homogeneous property with one Young's modulus. Plaques also present highly variable process with lesion composition and distribution varying in the different locations [83]. In order to describe such plaque deformation, many research groups have used that plaque constituents are assumed to exhibit linear elasticity [36, 37, 82, 93, 95, 96] and isotropy [36, 82, 89, 95, 96, 97]. In addition, some studies [5, 81, 98] propose that vulnerable plaques may be considered incompressible in the range 0.45 - 0.499 99 of Poisson's ratio variations, which means nearly incompressible. Hence, in this study, the plaque containing only lipid core is also assumed to be linear elastic, (nearly) incompressible, isotropic and homogeneous material.

As shown in Table IX [36, 37, 99, 100], the mechanical properties are described by E_r, E_θ and E_ℓ (Young's modulus in the r, θ and ℓ directions, respectively), $\nu_{r\theta}$, $\nu_{r\ell}$ and $\nu_{\theta\ell}$ (Poisson's ratios in the $r\theta$, $r\ell$ and $\theta\ell$ planes, respectively), and $G_{r\theta}$, $G_{r\ell}$ and $G_{\theta\ell}$ (shear modulus in the $r\theta$, $r\ell$ and $\theta\ell$ planes, respectively). We assumed that the general structure of arterial wall has identical mechanical properties in the radial (r) and circumferential (θ) directions. The values of E_r ($= E_\theta$) and E_ℓ for plaque and artery were taken from previous study of Cheng et al. [36, 37]. The poisson's ratios for plaque and artery, $\nu_{\theta\ell} = \nu_{r\ell} = 0.45$ and 0.27, were based on the previous studies [36, 37, 98]. $\nu_{r\theta}$ was calculated to satisfy the requirements for a positive-definite stiffness matrix [101]. The shear moduli for arterial wall were taken from the previous studies [36, 37, 98], and the values for lipid core in plaque domain were calculated with $G = E/2(1 + \nu)$ for isotropic material [101, 102].

Table IX. Elastic material parameters of arterial wall and lipid core

Mechanical Properties		Arterial wall	Lipid core
Young's modulus (kPa)	E_r	10	1,000
	E_θ	10	1,000
	E_ℓ	100	1,000
Poisson's ratio	$\nu_{r\theta}$	0.01	0.45
	$\nu_{\theta\ell}$	0.27	0.45
	$\nu_{r\ell}$	0.27	0.45
Shear modulus (kPa)	$G_{r\theta}$	10	344.8
	$G_{r\ell}$	50	344.8
	$G_{\theta\ell}$	50	344.8
Thermal expansion coefficient ($\times 10^5 {}^oC^{-1}$)	β_i	7.4695	30

These parameters where taken from [36, 37, 98, 99, 100, 103, 104].

If a body having a temperature change ΔT is allowed to expand freely, a line element of length ds in the body is elongated to a length $(1+\beta\Delta T)ds$, where β is defined as the coefficient of thermal expansion. The coefficient β in the bodies of arterial wall and plaque may be a constant because **(1)** the temperature heterogeneity in hot spot of plaques occur within around 2 ${}^oC$, and **(2)** the coefficient β for a number of structural materials remains fairly constant for a wide range of temperature [102]. In this study, the temperature dependent arterial thermal expansion coefficient is used for that of arterial wall at 37.5 ${}^oC$ [100], and the soft tissue thermal expansion coefficient is applied for that of lipid core [104]. As presented in Table IX, the arterial wall and lipid core were assumed to be thermally isotropic bodies, where β is independent of the direction of ds [100].

b. Thermal stress analysis

Thermal stress is generally caused by thermal expansion or contraction of the material when the thermal deformation is constrained. Temperature changes in plaque containing inflammatory cells can cause thermal stress effects. The thermal stress acting over endothelial cells can affect endothelium permeability to macromolecules and consequently speed up plaque growth or rupture process as indicated in Figure 7. In this section, the governing equations to estimate the thermal stress distributions observed under pulsatile flow condition are presented. The temperature changes are directly input as loads in a structural analysis to determine the thermal stress and displacement caused by the temperature loads.

The governing equations expressed in terms of equilibrium equation (3.19), constitutive equation (3.20), and compatibility condition (3.21) for linear functions are given by

$$\nabla \cdot \sigma = -\mathbf{F}, \tag{3.19}$$

$$\sigma = \mathbf{D}(\epsilon_\sigma + \epsilon_{\mathbf{th}}), \tag{3.20}$$

$$\epsilon = \frac{1}{2}(\nabla \mathbf{U} + (\nabla \mathbf{U}^t)), \tag{3.21}$$

where σ represents the stress tensor, and ϵ is the total strain expressed as the sum of mechanical ϵ_σ and thermal ϵ_{th} strain: ϵ_σ denotes the strain components due to the forces exerted by the blood flow, ϵ_{th} is the thermal strain due to the temperature change, and it is presented in terms of $\mathbf{U}$ the displacement component in the elastic body. In equation 3.20, $\mathbf{D}$ is the 6×6 elasticity matrix, which is defined differently

for isotropic (plaque) and orthotropic (arterial wall) materials [105]. For this study, the arterial wall follows the behavior of orthotropic material and the elasticity matrix **D** looks like

$$\mathbf{D} = \begin{pmatrix} \frac{1-\nu_{\theta\ell}\nu_{\ell\theta}}{E_\theta E_\ell \Delta} & \frac{\nu_{\theta r}+\nu_{\ell r}\nu_{\theta\ell}}{E_\theta E_\ell \Delta} & \frac{\nu_{\ell r}+\nu_{\theta r}\nu_{\ell\theta}}{E_\theta E_\ell \Delta} & 0 & 0 & 0 \\ \frac{\nu_{r\theta}+\nu_{r\ell}\nu_{\ell\theta}}{E_\ell E_r \Delta} & \frac{1-\nu_{\ell r}\nu_{r\ell}}{E_\ell E_r \Delta} & \frac{\nu_{\ell\theta}+\nu_{\ell r}\nu_{r\theta}}{E_\ell E_r \Delta} & 0 & 0 & 0 \\ \frac{\nu_{r\ell}+\nu_{r\theta}\nu_{\theta\ell}}{E_r E_\theta \Delta} & \frac{\nu_{\theta\ell}+\nu_{r\ell}\nu_{\theta r}}{E_r E_\theta \Delta} & \frac{1-\nu_{r\theta}\nu_{\theta r}}{E_r E_\theta \Delta} & 0 & 0 & 0 \\ 0 & 0 & 0 & 2G_{\theta\ell} & 0 & 0 \\ 0 & 0 & 0 & 0 & 2G_{\ell r} & 0 \\ 0 & 0 & 0 & 0 & 0 & 2G_{r\theta} \end{pmatrix}$$

where $\Delta = \frac{1-\nu_{r\theta}\nu_{\theta r}-\nu_{\theta\ell}\nu_{\ell\theta}-\nu_{\ell r}\nu_{r\ell}-2\nu_{r\theta}\nu_{\theta\ell}\nu_{\ell r}}{E_r E_\theta E_\ell}$. E_i is the $Young's\ modulus$ in i direction. ν_{ij} is the $Poisson's\ ratios$ in the $i-j$ plane. G_{ij} is the values of shear modulus in the $i-j$ plane, which is the ratio of shear stress divided by the corresponding shear strain in a linear elastic material. The material properties for the structural analysis are presented in the Table IX.

The lipid core of plaque domain is defined as an isotropic material, which is the following definition of elasticity matrix **D**:

$$\mathbf{D} = \frac{\mathbf{E}}{(\mathbf{1}+\nu)(\mathbf{1}-\mathbf{2}\nu)} \begin{pmatrix} 1-\nu & \nu & \nu & 0 & 0 & 0 \\ \nu & 1-\nu & \nu & 0 & 0 & 0 \\ \nu & \nu & 1-\nu & 0 & 0 & 0 \\ 0 & 0 & 0 & \frac{1-2\nu}{2} & 0 & 0 \\ 0 & 0 & 0 & 0 & \frac{1-2\nu}{2} & 0 \\ 0 & 0 & 0 & 0 & 0 & \frac{1-2\nu}{2} \end{pmatrix}$$

In this study, additional structural loads such as flow pressures and body force were neglected in the equations; this way is that the effect of temperature over the stability of the plaque will be estimated. Fluid-Structure interaction will be consid-

ered in future work. For the displacement boundary conditions, the constraints are specified by fully fixing at the inlet, outlet and outer wall surfaces of the arterial wall, which are defined as $\mathbf{u} = \mathbf{0}$ at $\ell = 0$, $\ell = L$ and $r = R$.

3. Calculation of temperature maps and thermal stress in 3-D arterial models

This section presents calculations of arterial wall temperature for the 3-D arterial models described previously in Chapter II and section 1, that correspond to a simplified straight artery and a realistic artery. The calculations for 3-D geometries are compared to those of the idealized 2-D arterial geometries presented previously (Figure 9). Finally, the temperature profiles calculated in 3-D realistic vessel anatomy (Figure 11) are used to determine thermal stress distributions.

a. Streamlines and temperature contours in 3-D simplified geometry

Figure 46 shows the streamlines along the longitudinal-direction in a plane crossing at the center of the vessel ($x = 0\ mm$). Two different times ($t = 5.3$ and $5.6s$) are selected to present the effect of inlet pulsatile flow during a cardiac cycle; $t = 5.3s$ is the time for the stronger forward flow, and $t = 5.6s$ is selected to present the backward flow during the cycle (Figure 25a). As observed in the calculations for 2-D straight artery, during the cycle, the blood flows smoothly from inlet to outlet without flow instabilities such as flow separation. However, due to the differences in the sizes of plaques used in 2-D and 3-D models, the characteristics of the flow vary, as well as its cooling effect, which will be discussed latter in this section. Particularly, the plaque of 3-D simplified geometry has thicker and shorter dimensions (Figure 10) than those of the 2-D geometry (Figure 12). In Figure 46, the variation of the streamlines at two different times during the cardiac cycle is observed only at the rear region of plaque. The streamlines follow closely the surface when the velocity is minimal ($t = 5.6s$),

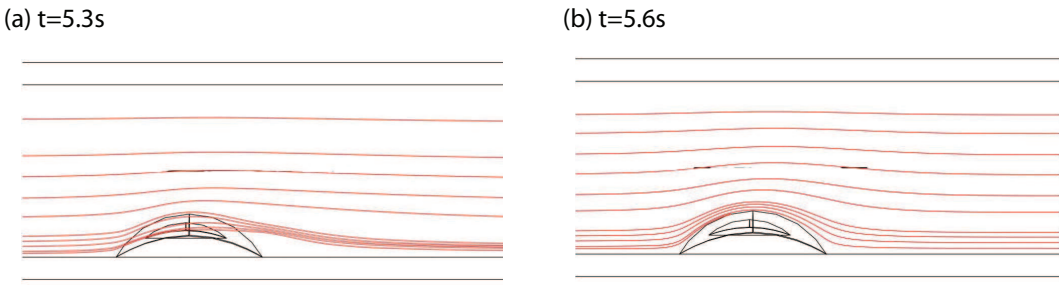

Fig. 46. Streamlines along the axial directional slice at the center of x-axis in 3-D simplified straight artery. The times **(a)** $t = 5.3$ and **(b)** $5.6s$ are selected to present the maximum and minimum velocity during the cardiac cycle (Figure 25a).

and they are not deflected at time $t = 5.3s$, when the velocity is maximal.

Figure 47 shows the temperature contours at longitudinal slices (axial-direction) at $t = 5.3s$ during a cardiac cycle for $\dot{q}_m = 0.1$ and $0.05\ W/mm^3$. The cuts are taken at the center of the vessel ($x = 0\ mm$) and the right side ($x = 0.75\ mm$) as indicated in Figure 47a. At the center ($x = 0\ mm$), temperature is increased to $53.5\ ^oC$, and temperature contours are clearly extended to downstream of the plaque due to the blood flow, and explains that the blood flow close to the plaque surface is heated as it moves downstream. On the other hand, the contours at the right side ($x = 0.75\ mm$) show the lower temperature variation. It is observed that the temperature variations between the center ($x = 0\ mm$) and right side ($x = 0.75\ mm$) shows a significant difference. This is due to the distribution of macrophage layer, where low conductivity of arterial wall prevents the conductive heat transfer from the macrophage layer. This observation suggests that a thermal detector, such as thermocouples or thermistors, should be used to measure several points along the longitudinal-direction to obtain the maximum temperature increase. At the center plane ($x = 0\ mm$), the temperature variations range between 37.5 and $53.5\ ^oC$,

and between 37.5 and 45.4 ^oC for $\dot{q}_m = 0.1$ and 0.05 W/mm^3, respectively. In 2-D calculations (Figure 33), the temperature variation for straight artery is between 37.5 and 40.1 ^oC for $\dot{q}_m = 0.1$ W/mm^3, which is less than the values of 3-D calculations.

Figure 48 shows snapshots for temperature distribution along the plaque surface in the longitudinal direction at different times through a cardiac cycle. The representative times, $t = 5.0$, 5.3, 5.6, 5.8 and $6.0s$, are selected in terms of characteristics of inlet velocity profile. During a cycle, the maximum temperature location changes spatially between $\ell/\ell_p = 0.5$ and 0.7; in comparison, the results of 2-D straight case show that the maximum temperature is constantly located at the downstream edge of the plaque ($\ell/\ell_p = 0.7$) as shown in Figure 26. The temperature distribution varies to the characteristics of inlet blood flow, which is referred as the convective cooling effect of blood flow. For $\dot{q}_m = 0.1$ W/mm^3, the temperature change ΔT at $t = 5.3s$ is reduced to 1.2 ^oC, and the temperature change ΔT immediately increases to 2.7 ^oC at $t = 5.6$. During the cycle, the least temperature variation occurs at $\ell/\ell_p = 0.75$, where may be a good place to measure the relatively constant temperature in the presence of pulsatile blood flow. During a cardiac cycle, the maximum temperature changes ΔT_{max} are to 2.7 and 1.5 ^oC for $\dot{q}_m = 0.1$ and 0.05 W/mm^3, respectively.

Figure 49 shows the temperature contours surrounding the atherosclerotic plaque at cross-sectional slices for $\dot{q}_m = 0.1$ and 0.05 W/mm^3 at $t = 5.3s$ during a cardiac cycle. As shown in Figure 49a, the slices are separated by 1 mm, and located at the center of the plaque ($\ell = 25$ mm) and 1 mm before and after the plaque center ($\ell = 24$ and 26 mm), respectively. These points correspond to the front, middle and rear region of plaque as used in 2-D models (Figure 29). Regardless of the values of metabolic heat generation, the higher temperatures are contoured at the middle region ($\ell = 25$ mm) due to plaque symmetry. Compared with the lower temperature increase at the front region ($\ell = 24$ mm), the rear region ($\ell = 26$ mm) has the

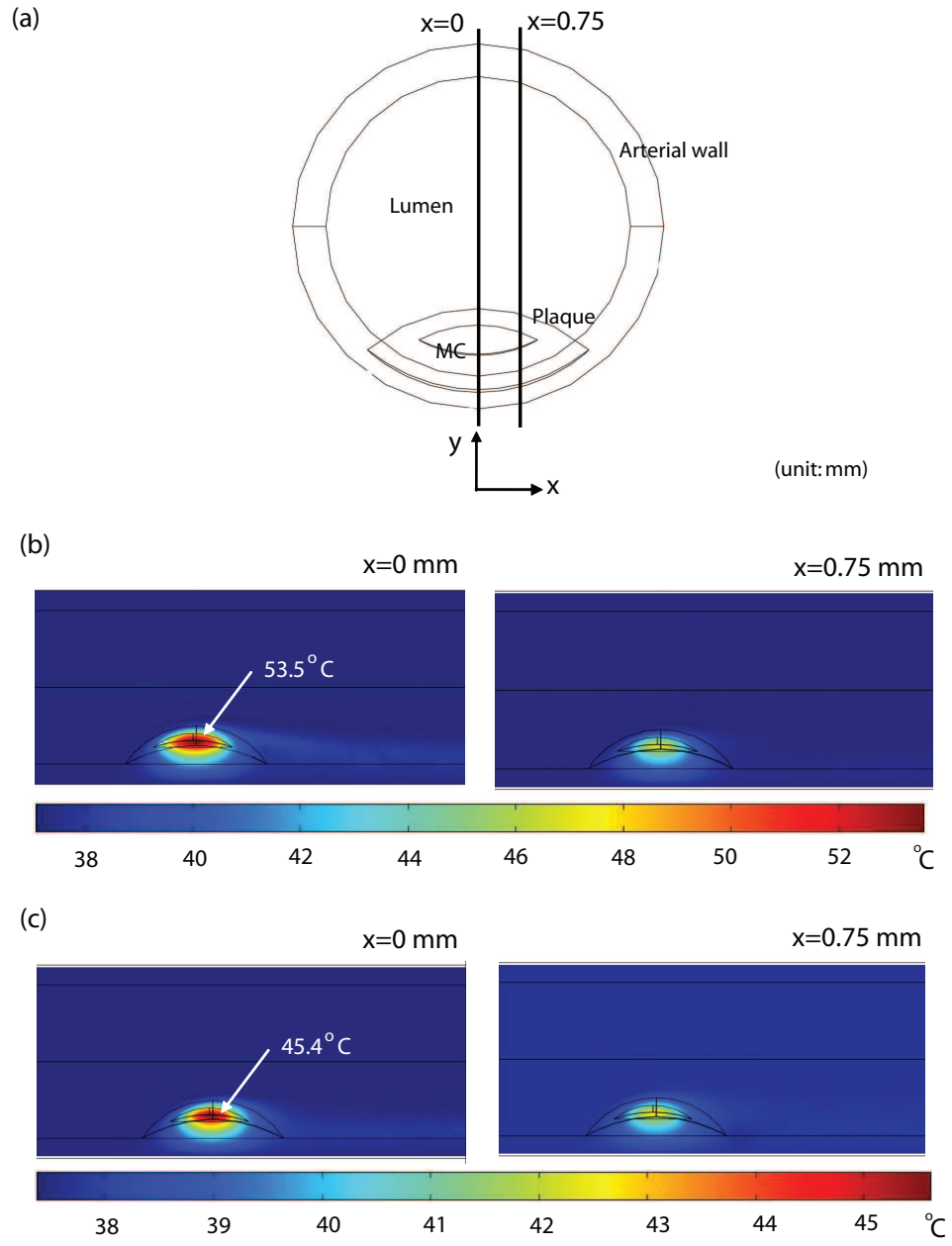

Fig. 47. Temperature contours at two axial-directional slices. **(a)** Longitudinal slices in the direction of blood vessel (center ($x = 0\ mm$) and right side ($x = 0.75\ mm$)). Two heat generation of **(b)** 0.1 and **(c)** 0.05 W/mm^3 are considered to reproduce the thermal heterogeneity observed in 2-D cases. Times $t = 5.3s$ is selected during the cardiac cycle (Figure 25a).

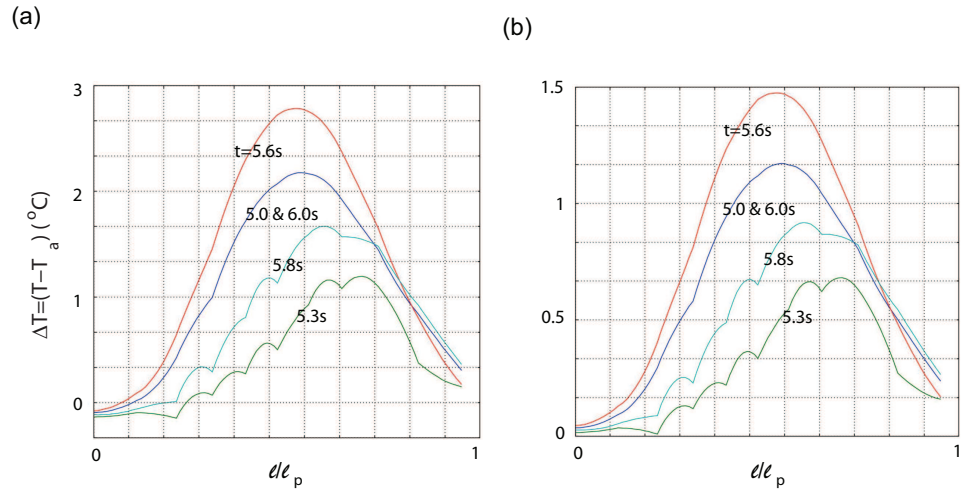

Fig. 48. Transient temperature distribution along the centerline of plaque surface at the axial-direction in 3-D simplified straight artery. For local heat generation, $\dot{q}_m$ of **(a)** 0.1 and **(b)** 0.05 W/mm^3 are applied during cardiac cycles (Figure 25a).

higher temperature due to the fact that blood has higher temperature at the region, as observed in Figure 48.

b. Temperature history at points in 3-D simplified geometry

This section shows how plaque surface temperature responds to blood flow and its transient alterations. Five representative points at the plaque/lumen interface are selected to investigate the local temperature variations during cardiac cycles. The points are distributed over the plaque surface, as indicated in Figure 50. Particulary, three points are located in the longitudinal direction and two points are located in the cross-sectional direction.

According to 2-D unsteady calculations, the temperature variations have different patterns in three thermal regions: front, middle and rear region, which is observed in

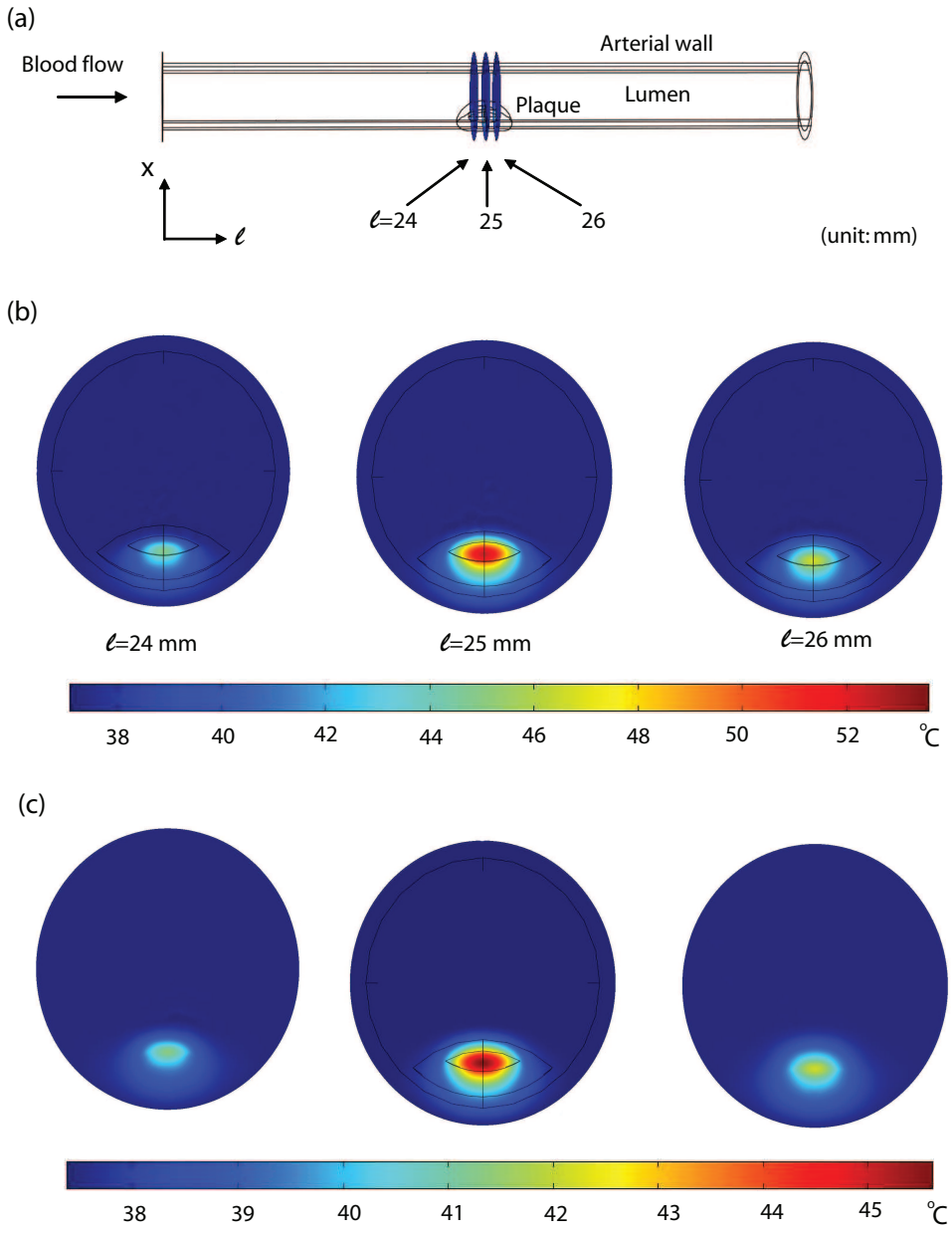

Fig. 49. Temperature contours at three cross-sectional slices. **(a)** Cross-sectional slices are at 24, 25 and 26 mm of axial-axis (ℓ), which correspond to the front, middle and rear region of plaque. Two different metabolic heat productions are considered: **(b)** $\dot{q}_m = 0.1$ and **(c)** 0.05 W/mm^3. The times $t = 5.3$ is selected during the cardiac cycle (Figure 25a).

Figures 29 to 32. In 3-D simplified model, temperature history is traced at five points over the plaque/lumen interface during the cardiac cycle; three representative points, **A**, **B** and **C**, correspond to the front region, the center of the middle region, and the end of the rear plaque. Two representative points, **D** and **E**, present the right and left side of the middle region in cross-sectional direction.

Figure 50 shows the temperature history at five representative points (**A**, **B**, **C**, **D**, and **E**) for $\dot{q}_m = 0.1$ and $0.05\ W/mm^3$. In this figure, the calculations are extended for five cardiac cycles. For the case of $\dot{q}_m = 0.1\ W/mm^3$, the temperatures at the representative points changed approximately between 0 and 2.7 ^oC. During the cycle, the maximum temperature occurs at point **B**; the temperature variation observed at this point directly corresponds to the characteristics of inlet pulsatile flow. Meanwhile, the temperature changes at point **A** remains relatively constant and equal to body temperature (37.5 ^oC). The temperature at point **C** is around 0.5 degree higher than that of point **A** due to the cooling effect of blood flow. In the cross-sectional points, the temperature changes at points **D** and **E** are little affected by both the concentration of inflammatory cells as well as blood flow pattern; these points almost overlaps due to the symmetry of the plaque geometry. For $\dot{q}_m = 0.05\ W/mm^3$, the temperature at the representative points are varied between 0 and 1.4 ^oC, which show the similar characteristics with the case of $\dot{q}_m = 0.1\ W/mm^3$.

c. Streamlines and temperature contours in 3-D realistic geometry

In 3-D realistic model, $0.005\ W/mm^3$ is used for $\dot{q}_m$ to reproduce the temperature variations observed in 2-D calculations because the lipid core as a macrophage layer in the 3-D realistic model has the larger volume than those of 2-D and 3-D simplified models. The representative times of $t = 5.3$ and $5.6s$ are chosen to consider the maximum and minimum velocity from the idealized inlet pulsatile flow (Figure 45).

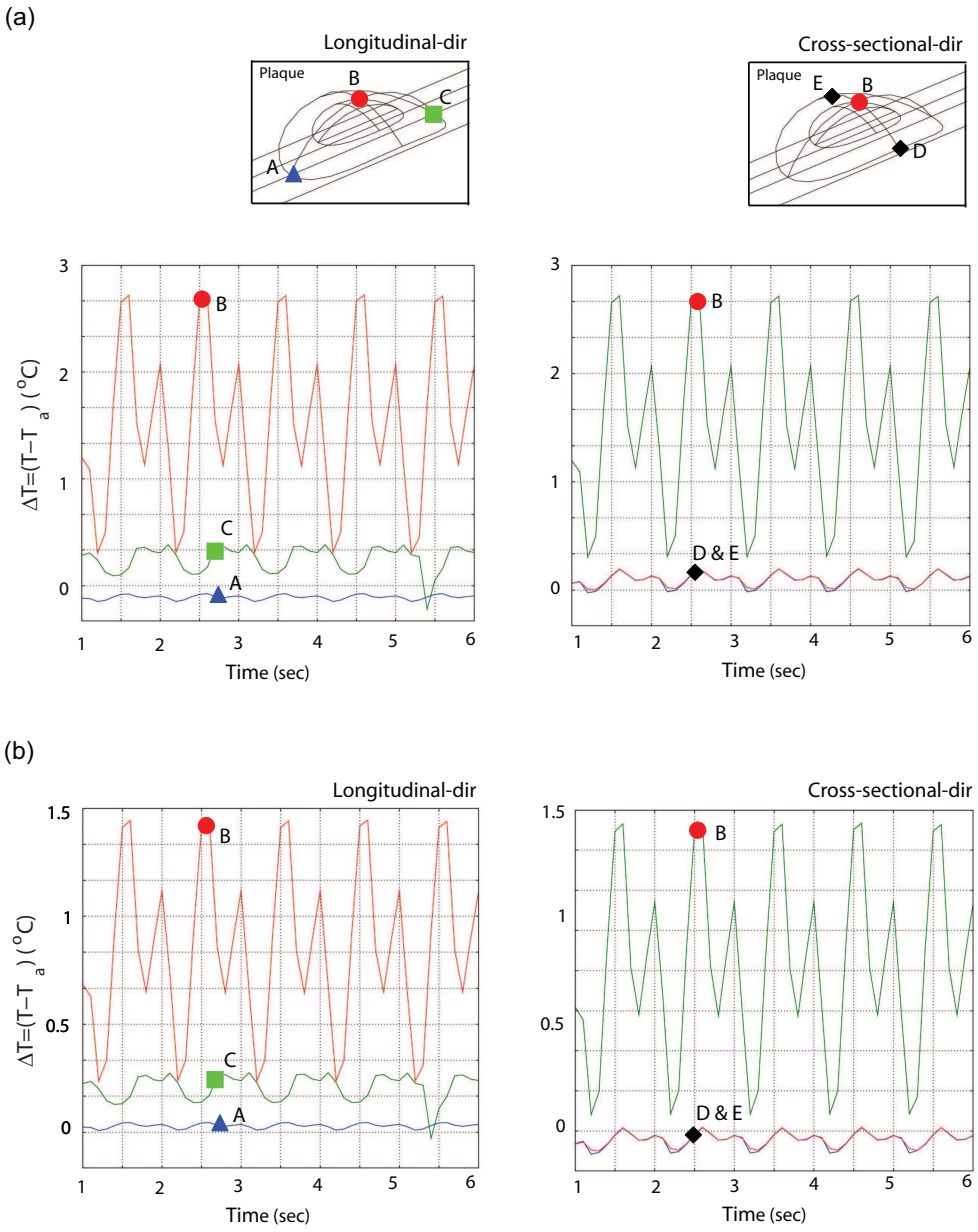

Fig. 50. Temperature history at the representative five points (**A**, **B**, **C**, **D**, and **E**) at plaque surface. Temperature under the heat generation of **(a)** $\dot{q}_m = 0.1$ and **(b)** 0.05 W/mm^3 is recorded during five cardiac cycles (Figure 25a).

Figure 51 shows the streamlines along the longitudinal-direction in a plane crossing at the center ($x = 0$) of the vessel. As observed in 3-D simplified model, the blood flows smoothly from inlet to outlet without flow instabilities during the cycle. Approximately 45% stenosis is considered in this model; such constriction corresponds to a threefold increase ($V_{max} = 0.46\ m/s$) in velocity at the peak region of plaque, which leads to the different characteristics of blood flow between at $t = 5.3$ and $5.6s$. The streamlines at $t = 5.3s$ pass the plaque directly without turning the direction around the rear region, but those at $t = 5.6s$ surround the rear region of plaque, which is observed in the simplified model.

In Figure 52, temperature contours are described at the longitudinal slices at $t = 5.3s$ during a cycle. Two slices are chosen at the center ($x = 0\ mm$) and right side ($x = 1.3\ mm$) of the vessel. At the center ($x = 0\ mm$), temperature varies between 37.5 and 42.7 ^oC, and temperature contours are comparably extended longer toward the outlet of the vessel. At the side ($x = 1.3\ mm$), maximum temperature recorded at the plaque decreases to 41 ^oC in comparison to 42.7 ^oC in the center ($x = 0\ mm$) because of the variation of macrophage layer distribution and the lower conductivity of arterial wall. Such difference of temperature variations at two locations ($x = 0$ and $1.3\ mm$) suggests multiple measuring points within short distance as 1 or 2 mm, because a significant difference in temperature is observed along the axis.

Figure 53 presents the temperature contours at three cross-sectional slices at $t = 5.3s$. The slices are separated by 9 and 8 mm, and are located at the center of the plaque ($\ell = 25\ mm$) and 9 before and 8 mm after the plaque center ($\ell = 20$ and $37\ mm$), respectively. These points also present the front, middle and rear region of plaque as used in 2-D model (Figure 29). The maximum temperature increase recorded is 42.5 ^oC, and occurs at the middle of the lipid core. The temperature contours surrounding plaque at the front ($\ell = 20\ mm$) are described in a smaller

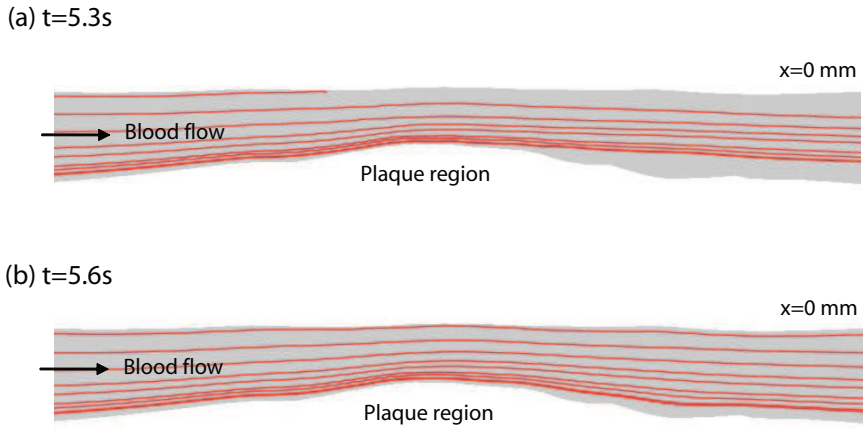

Fig. 51. Streamlines along the axial-directional slice at the center ($x = 0\ mm$) of x-axis in 3-D realistic straight artery. The times $t = 5.3$ and $5.6s$ are selected during the cardiac cycle (Figure 45).

region than those at the rear ($\ell = 37\ mm$) because the convective effect of blood flow drags the thermal energy from the front to the rear region, which was also observed by 2-D temperature contours in Figure 23.

d. Temperature history at points in 3-D realistic geometry

Figure 54 shows the temperature history at the representative points during three cardiac cycles. The representative points (**A** through **G**) are located along the centerline in the longitudinal-direction at the plaque/lumen interface as indicated in Figure 54. Through the cycles, the calculated temperatures changes (ΔT) varied from 0.08 to 0.7 ^oC. The temperature at point **A** is almost constant and close to body temperature (inlet blood temperature). The maximum temperature occurs at point **E**, located at the downstream of the middle region. The temperature variations at points **B** through **E** follow almost the same pattern, which strongly depends on the characteristics of inlet pulsatile flow (Figure 45). The fluctuation of temperature dur-

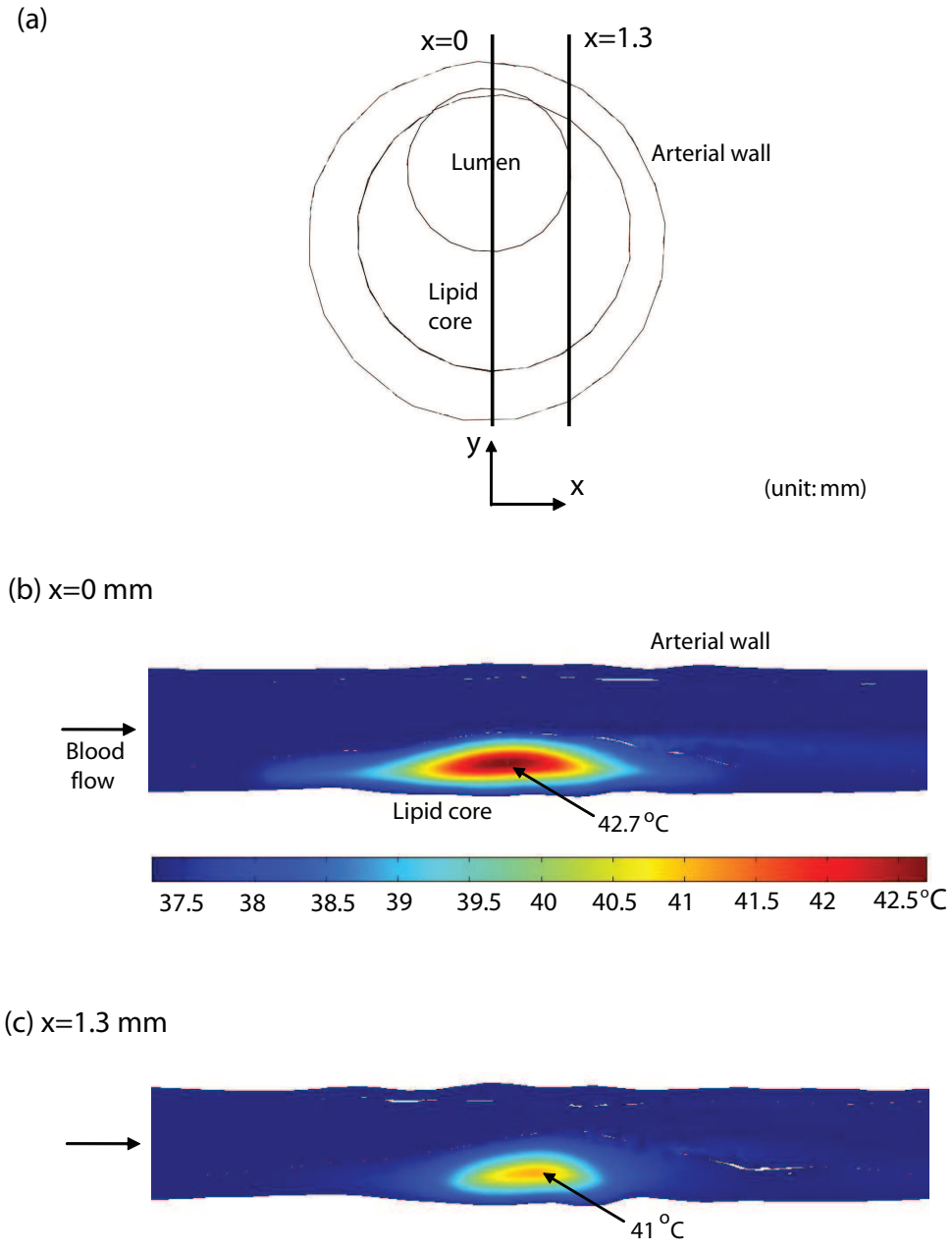

Fig. 52. Temperature contours at axial-directional slices at $t = 5.3s$. **(a)** Two longitudinal slices are considered **(b)** at the center ($x = 0\ mm$) and **(c)** side ($x = 1.3\ mm$) along x-axis. The heat generation of $\dot{q}_m = 0.005\ W/mm^3$ is considered to reproduce the thermal heterogeneity observed in 2-D cases.

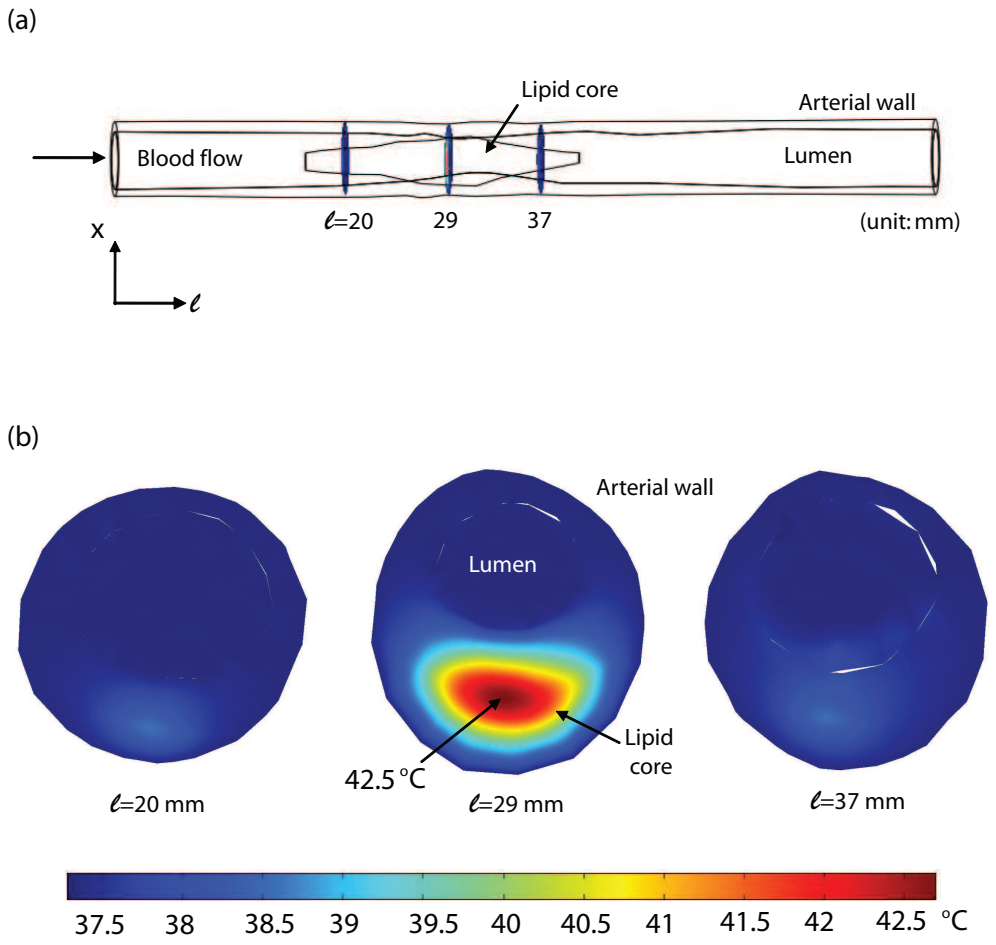

Fig. 53. Temperature contours at **(a)** three cross-sectional slices located at $\ell = 20$, 29 and 37 mm of axial-axis, which represent the front, middle and rear region of plaque. $\dot{q}_m = 0.005\ W/mm^3$ is considered for metabolic heat generation. The times $t = 5.3s$ is selected during the cardiac cycle (Figure 45).

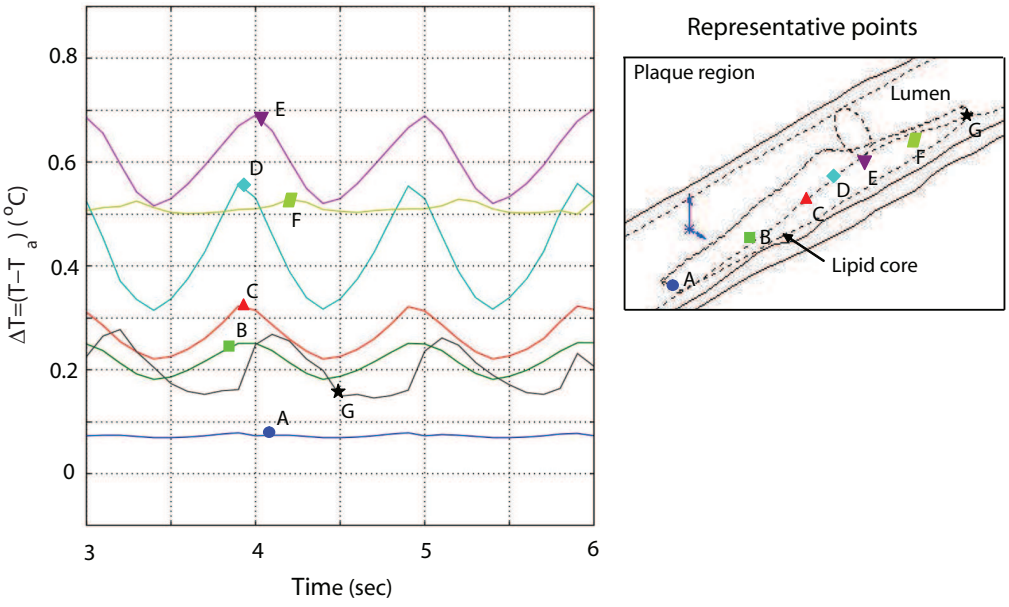

Fig. 54. Temperature history at the representative seven points (**A** through **G**) at axial direction of plaque/lumen interface. Temperature under the heat generation of $\dot{q}_m = 0.005\ W/mm^3$ is recorded during three cardiac cycles.

ing the cardiac cycles seems to disappear at point **F**, where the temperature change remains at 0.5 ^oC. In 2-D unsteady calculations, such a constant temperature region was observed between $l/l_p = 0.6$ and 0.7 during a cardiac cycle. The temperature change at point **G** varies following a different pattern from that of points **B** through **E**, where varied between 0.15 and 0.27 ^oC. Considering the 2-D calculations as shown in Figure 30, temperature at the end point (**G**) shows usually constant value, which do not reflect the characteristics of inlet pulsatile flow. However, in the 3-D realistic geometry used, point **G** seems to show temperature change that follows an inlet pulsatile flow pattern. This might be the result of the complicated geometry.

e. Thermal stress analysis in 3-D realistic geometry

In this section, thermal stress calculations at inflammatory process are conducted to determine how the arterial wall and plaque surface are influenced by thermal stress. Thermal stress distribution in arterial wall containing vulnerable plaque is characterized, and highly thermal stressed regions are investigated during cardiac cycles. In this calculations, shear stress of blood flow at arterial wall is ignored to consider purely thermal stress impact.

Figure 55 shows thermal stress fields produced by the temperature maps described in Figure 52; Figure 55 shows thermal stress at $t = 5.3s$ during a cycle. Two longitudinal slices are chosen at the center ($x = 0\ mm$) and right side ($x = 1.3\ mm$) of the vessel as shown in Figure 52a. At the center ($x = 0\ mm$) plane, the most highly stressed region is the plaque/lumen interface above the lipid core, where von Mises stress of 1.45 Pa is obtained by temperature variation between 37.5 and 42.7 ^oC. At the side ($x = 1.3\ mm$) plane, the maximum stress is occurred at the edges of lipid core. The von Mises stress obtained by the temperature variation between 37.5 and 41 ^oC are varied between 0.02 and 1.15 Pa. The maximum thermal stress regions almost coincide with the regions of stress-concentration already observed in autopsy specimens [6, 36, 37, 38] that correspond to the plaque cap over the the lipid pool or the luminal wall near the thinnest plaque section.

Figure 56 presents the stress contours at three cross-sectional slices at $t = 5.3s$. The slices are also located at the center of the plaque ($\ell = 29\ mm$) and 9 mm before and 8 mm after the plaque center ($\ell = 20$ and 37 mm), respectively, as shown in Figure 53a. The maximum thermal stress of 1.45 Pa is obtained at the center ($\ell = 29\ mm$) of the plaque, where the most highly stressed regions lie at the plaque/lumen interface over the lipid core and both edges of lipid core. At the front ($\ell = 20\ mm$)

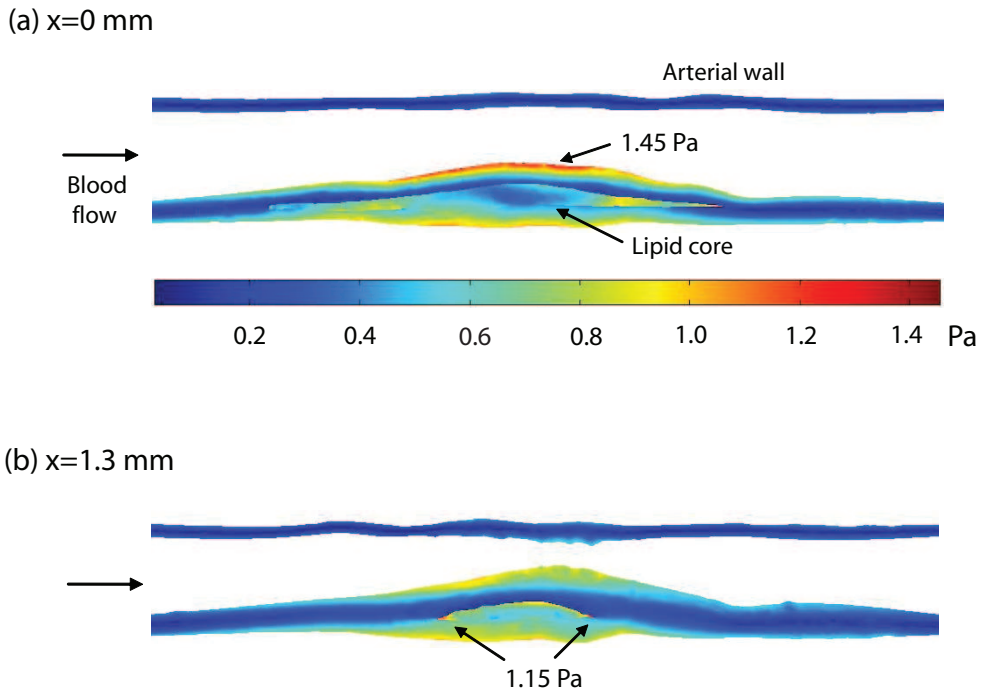

Fig. 55. Distribution of Von Mises stress at axial-directional slices of at $t = 5.3s$. **(a)** Two longitudinal slices considered **(b)** at the center ($x = 0\ mm$) and **(c)** right side ($x = 1.3\ mm$) along x-axis. $\dot{q}_m = 0.005\ W/mm^3$ is considered for metabolic heat generation.

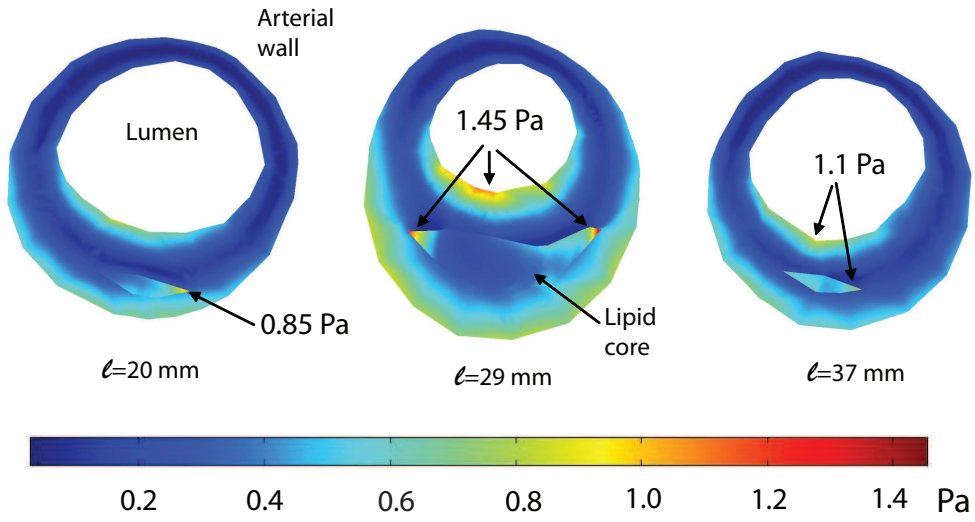

Fig. 56. Temperature contours at **(a)** three cross-sectional slices located at $\ell = 20$, 29 and 37 mm of axial-axis, which represent the front, middle and rear region of plaque. $\dot{q}_m = 0.005\ W/mm^3$ is considered for metabolic heat generation. The times $t = 5.3s$ is selected during the cardiac cycle (Figure 45).

and rear ($\ell = 37\ mm$) regions, the maximum thermal stresses are 0.85 and 1.1 Pa, respectively, and the highly stressed region in each plane also appears at the corners of lipid core; these edge areas of lipid core are tightly connected with arterial wall having different tissue material properties. It is observed that plaque structural feature such as fibrous cap thickness and the lipid core size (or macrophage layer size) may be critical in determining thermal stress and consequentially evaluating overall plaque stability. In addition, the thermal stresses at the rear are higher than those at the front because higher temperature due to the reduced convective effect of blood flow is observed at the downstream region of plaque, as explained in Figures 52 and 53.

f. Stress history at points in 3-D realistic geometry

In Figure 57, thermal stress history is shown at the representative points (**A** through **G**) during three cardiac cycles. The representative points are located along the centerline in the longitudinal-direction as indicated in Figure 54. Through the cycles, thermal stresses calculated seems to be constant without any variation at every point (Figure 57a). However, thermal stress obtained by temperature rise should vary corresponding to the flow pattern as temperature variation follows the characteristics of inlet pulsatile flow in Figure 54. In order to show the variation of thermal stress during cardiac cycles, the history of thermal stress at point **C** is presented with the magnified scale in Figure 57b, where von Mises stress are varied between 0.8756 and 0.8759 Pa.

As shown in Figure 57a, thermal stresses at point **A** through **G** are distributed between 0.6 to 1.0 Pa; the values are increased at from point **A** to **D**. After the peak thermal stress at point **D**, the values are gradually decreased from **E** to the most end point **G**. Such pattern of thermal stress is dominated by the temperature distribution in Figure 54. It is observed that increasing temperature due to inflammatory process increases thermal stress influencing over plaque stability. Thermal stress calculated in our study are relatively lower than shear stress produced by blood flow in the study of Tang et al., where it has been reported that the maximal shear stress at plaque cap thickness of 0.4 mm is varied to 40 KPa [6]. Although the effect of thermal stress may be too small to directly weakening of the plaque structure, thermal stress can be more important because it steadily affects the endothelial permeability of plaque surface to promote molecule transport such as macrophage infiltration and may cause fatigue of the plaque surface during repetitive cardiac cycles. The quantitative difference between our calculations and Tang's study [6] can be caused by

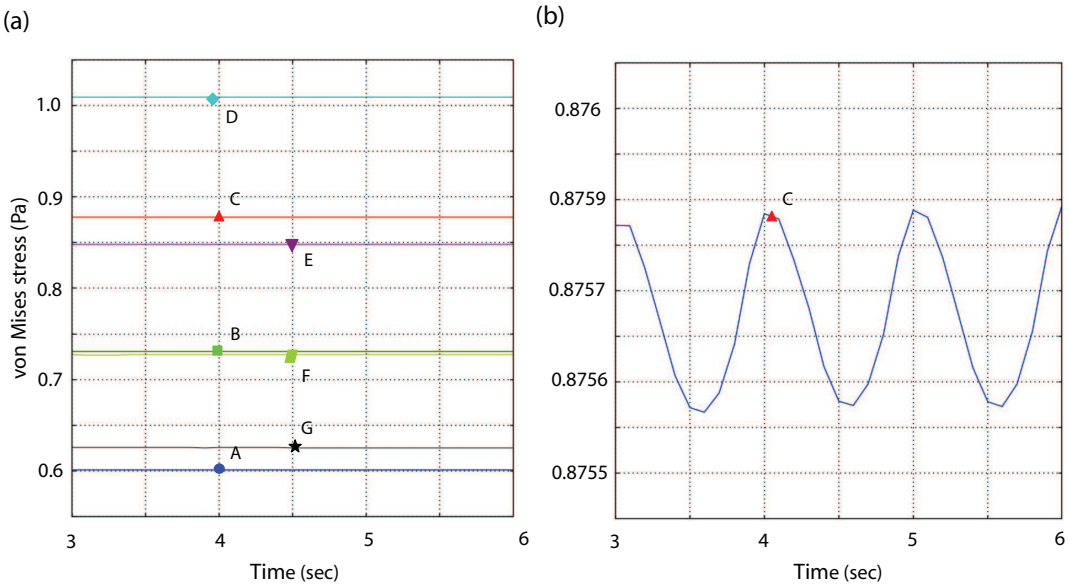

Fig. 57. Stress history at the representative seven points (**A** through **G**) at axial direction of plaque/lumen interface. $\dot{q}_m = 0.005\ W/mm^3$ is applied for metabolic heat generation during three cardiac cycles (Figure 45).

somewhat different conditions such as different length of outer boundary constrained and material properties used in structural analysis.

4. Conclusions of thermal stress in 3-D model

In 3-D model, the temperature distributions changed with an inlet pulsatile flow were determined to observe the convective cooling effect over AWT. Thermal stresses produced by temperature heterogeneity were calculated to understand the relation between the thermal stress and inlet pulsatile flow characteristics, and to reveal the contribution of thermal stress to plaque evolution and rupture.

In simplified model, the maximum temperature point was spatially varied downstream of the plaque; In contrast, the maximum point calculated for 2-D straight artery was occurred at almost constant location. This was explained by the differ-

ent geometry (thicker in height and shorter in length) from 2-D plaque, which might cause the stronger momentum of blood flow at the rear region of the plaque. It was observed that the temperature was spatially varied in a sensitive way to arterial geometry. It was also observed that a constant temperature region is occurred at $\ell = 0.7$ during a cardiac cycle, where could be a good spot to obtain the relatively constant temperature during cardiac cycles.

It was observed that the temperature variations between the center and the side of plaque were significantly different even if two points were not far from each other. In realistic model, the temperature variation at the side region 1.3 mm away from the centerline of lipid core was between 37.5 and 41 ^oC, which was significantly lower than the temperature variation (37.5 to 42.7 ^oC) at the center in spite of the short distance between two points. This might have occurred by the variation of macrophage layer distribution and the low conductivity of arterial wall, which prevented the conductive heat transfer from the lipid core. Therefore, the multiple measuring points must be considered to decrease the potential error in temperature measurement even within 1 or 2 mm at centerline region of plaque measured.

The realistic model also showed the cooling effect over temperature distribution surrounding plaque. The specific point remaining the relatively constant temperature was observed at the downstream of the plaque, which could be the best spot to measure AWT. Meanwhile, at the most end point of the plaque, the significant temperature variation was unexpectedly observed depending on an inlet flow pattern although temperature at the most end point in 2-D straight model showed usually constant value without any inlet blood flow effect. Therefore, to remove the potential error of measurement, the denser measuring points were recommended even at the rear region of the plaque.

In realistic model, thermal stress calculations were conducted to determine how

atherosclerotic arterial wall and plaque surface were affected by thermal stress. As temperature increase of 42.7 ^oC was taken as the maximum temperature, thermal stress could be increased to 1.45 Pa without considering shear stress related to blood flow. During cardiac cycles, thermal stress variation did not differ significantly due to the thermal expansion behaviors of the arterial wall and lipid core. However, the most highly thermal stressed region in each plane appeared at the corners of lipid core, and another high stressed region was the plaque/lumen interface above the lipid core; these regions similarly corresponded to the high stress-concentration regions observed in other studies [6, 36, 37, 38]. This calculations of thermal stress, which has never considered in other studies, would produce more realistic observations in stress analysis and enhanced the reliability of predicting potential failure locations in plaque/lumen surface.

CHAPTER IV

CONCLUSIONS

This study presented a mathematical model that can be used as a tool to improve treatment modalities involving direct arterial wall temperature measurements, and detection of vulnerable plaque. In this study, thermal inhomogeneity of an atherosclerotic plaque was characterized by the structure of the vulnerable plaque, such as the size of lipid core, thickness of fibrous cap, and population of macrophages in the fibrous cap.

In 2-D steady and unsteady calculations, parametric studies were performed to analyze the contribution of plaque geometry over the arterial wall temperature. The geometric parameters studied to characterize plaque were plaque thickness (d_p), macrophage rich layer thickness (d_{mp}), fibrous cap thickness (l_f), plaque extension (l_p), macrophage extension (l_{mp}), wall thickness (d_w). In 2-D unsteady calculations, the gradual reduction of inlet blood flow is proposed to look at the cooling effect of blood flow as a result of the introduction of a catheter in the blood vessel. This study was performed to better understand contradictory experimental results. In 3-D arterial model, arterial wall temperature variation and thermal stress was investigated with the objective to evaluate how thermal inhomogeneity affects plaque stability.

This mathematical study would contribute to elucidate the relationship between inflammation and plaque rupture/evolution using temperature as the monitoring variable parameter, and also suggested a better way to understand the arterial wall temperature measurements obtained with novel catheters

A. 2-D Steady Blood Flow Calculations

Arterial wall temperature variation was in proportion to metabolic heat generation q_m, macrophage layer thickness d_{mp} and plaque thickness d_p, whereas varies inversely with fibrous cap thickness l_f. Especially, metabolic heat generation q_m and macrophage layer thickness d_{mp} had more influence over the plaque temperature. Temperature distribution along plaque/lumen surface was significantly influenced by the blood flow running through the vessel which is referred as the cooling effect of blood flow [16, 21]. Temperature distributions at bending and bifurcation artery were affected by flow separation and circulation caused by arterial geometry effect. In the presence of blood flow, maximum temperature change was located behind the apex of the plaque, which was governed by arterial geometry, distribution of macrophage layer, and flow instabilities such as flow separation and flow circulation. Hence, the best spot to measure plaque temperature was between the middle and the far edge of the plaque where the point of maximum temperature can be located. It could be also postulated that direct measurements should be taken very close to the plaque/lumen surface.

B. 2-D Unsteady Blood Flow Calculations

It was observed that the locations of the hot spot were strongly dependent on the inlet pulsatile flow pattern, and maximum temperature changes were generally located behind the apex of the plaque. During cardiac cycles, transient temperature variations were different from each artery because the effect of different arterial geometries and inlet pulsatile flow patterns contributed to the characteristics of blood flow at plaque/lumen surface.

It was recommended that the best location to measure plaque temperature in the

presence of blood flow might be between the middle and the far edge of the plaque because the maximum temperature occurred in that region and the temperature at the plaque/lumen interface would vary significantly less in such region. For sampling rate and measuring distance of plaque temperature, temperature measurements should be performed in at least 2 locations including mid and rear regions during a couple of cardiac cycles. In addition, direct measurements of plaque temperature should be taken very close to the plaque/lumen surface within 100 μm away from the plaque surface.

C. Plaque Temperature during Blood Flow Reduction

The calculations aimed to understand the relationship between arterial wall temperature and flow reduction due to catheters used to measure local temperature. During normal pulsatile flow, the characteristics of the inlet flow dominated the convective cooling effect on the plaque/lumen surface and caused considerable variation of temperature along the plaque surface in space and time. As blood flow was reduced, the convective cooling effect decreased on the plaque/lumen surface and the plaque temperature increased. The blood flow reduction provided different effects on the front, middle and rear regions of the plaque, which were different from each arterial geometry. Consequently, blood flow reduction contributed to the increase of plaque surface temperature and the minimum required reduction time needed to observe local temperature increase in the presence of an active plaque was at least 6 seconds.

D. Thermal Stress in 3-D Model

The temperature variations between at the center and at the side of plaque in cross-sectional direction had a significant difference in spite of the short distance between

two measuring points. This might be occurred by the variation of macrophage layer distribution and the low conductivity of arterial wall. Therefore, the multiple measuring points must be considered to decrease the potential error in temperature measurement even within 1 or 2 mm at centerline region of plaque measured.

In thermal stress calculations, during cardiac cycles, the most highly thermal stressed regions were observed at the corners of lipid core and the plaque/lumen interface above the lipid core. In the calculations, thermal stress variation did not differ significantly due to the thermal expansion behaviors of the arterial wall and lipid core. However, thermal stress steadily affected the endothelial permeability of plaque surface to promote molecule transport such as macrophage infiltration and caused fatigue of the plaque surface during repetitive cardiac cycles. Thus, it was expected that the distribution of thermal stress might contribute to reliability of determining overall plaque stability.

CHAPTER V

FUTURE WORK - PLAQUE EVOLUTION

A. Background

A variety of physical factors have been proposed to determine overall plaque stability; these include mechanical shear stress in blood vessels [32, 33, 34, 35], circumferential stress distribution [6, 36, 37, 38, 39], and transport and accumulation of macromolecules [40, 42]. These studies have been performed in isothermal conditions without considering any thermal stress introduced by plaque inflammation. Recently, atherosclerosis has been recognized as an inflammatory disease, as there is significant correlation observed between plaque temperature and rupture likelihood [3, 13, 14, 15, 16, 18, 19, 20]. Activated inflammatory cells embedded in plaques release heat; it is a hypothesis that such residual heat affects transport of macromolecules and plaque growth. We want to use our thermal analysis of the plaque to estimate how the temperature heterogeneity of plaque contribute to thermal stress that may further weaken the sensitive plaque surface and directly affect endothelium permeability. This dissertation has shown the factors controlling the thermal inhomogeneity of the plaque and the thermal stress produced in the hot spot; however the effect of temperature on plaque growth and evolution needs to be studies for the further understanding of vulnerable plaque. This chapter represent a simplified model that is proposed to study the plaque evolution.

In order to explain the growth of atherosclerotic plaque and how it is affected by temperature or inflammatory response, previous work on stress-modulated growth and remodeling of soft tissues will be employed with some modifications [106, 107, 108, 109]. Skalak has found that a cell in tissue grows independently of its neighbors

that is not compatible and residual stress resulting from locally incompatible growth deforms soft tissues [106, 107, 108]. Rodrigez et al. have proposed that the shape change of an unloaded tissue during growth is described by a mapping analogous to deformation gradient tensor [109]. To address the concept of volumetric growth, Rodrigez et al. introduced the multiplicative decomposition of the total deformation gradient into its elastic and growth parts [109, 110]. In this work, such theory will be used for modeling the evolution of atherosclerotic plaques under non-isothermal process; it consider thermal stress.

In this study, the growing plaque through mass transport will be explained with the basic assumptions: **(1)** material properties of plaque are changed under thermal effect (i.e. thermal stress) and **(2)** the plaque with the material properties is linearly growing under non-isothermal process. Under these assumptions, constitutive relations are necessary to describe the material's deformation related to the plaque growth [79, 111]. To formulate of constitutive relations, the governing equations such as the balances of mass, momentum, energy and entropy are derived; the equations are based on the general continuum formulation for finite volumetric growth in soft elastic tissues [109, 110]. The constitutive equations restricted by the Clausius-Duhem (CD) inequality [79, 112] are developed for the volumetric growth of plaque under non-isothermal process. Helmholtz free energy function for elastic materials is suggested for thermal process of atherosclerotic plaque assumed [113]. Finally, the growth and remodeling of the atherosclerotic plaque is simply described with the concept of the multiplicative decomposition of the deformation gradient into its elastic and growth parts [106, 107, 108, 109, 110].

B. Material Characteristics of Plaque

As the first step, the general characteristics of the material should be classified with its composition and behavior to formulate a constitutive relation. Atherosclerotic plaque is highly progressive and materially heterogeneous due to the accumulation of the lipids, cells, connective tissue and calcium in intima of arterial wall. The composition of plaque is primarily defined by dense and cellular fibrous tissue as collagen fibers, and the small percentage of plaque is occupied by pultaceous debris, foam cells and calcific deposits [79, 91]. Although the composition of plaque suggests that atherosclerotic plaque exhibits the general behavior of soft tissue, we must more briefly determine the material characteristics of plaque used herein.

In this growth model, the plaque has been assumed to have a linear relation regardless of the highly nonlinear relation for the stress-strain of soft tissues. Also, our model is assumed to follow hyperelastic [1] behavior although hydrated and perfused tissues are usually modeled as viscoelastic [2]. The plaque remains incompressible during the mass growth (ρ (locally) = ρ_o (globally)) as most tissues consist largely of water. Although arteries exhibit cylindrical orthotropy [3] and plaque consists of different structural constituents with material heterogeneity, the material of plaque in the model exhibits materially homogeneous [4] and isotropic [5] behavior for simplicity. More importantly, the plaque has thermal heterogeneity due to metabolic heat generation of inflammatory cells, and the plaque grows under non-isothermal process.

---

[1] The elastic behavior is quantified in terms of a strain energy function W, that is, the recoverable energy stored in the material as it deforms.

[2] which accounts for a combined viscous (fluid like) and elastic (solid like) behavior

[3] The responses in radial, circumferential, and axial directions are distinct.

[4] The response to applied loads is independent of position within the body.

[5] The responses of the material to an applied load is independent of the direction of loading.

As a result, the plaque material will be considered to follow elastic, incompressible and isotropic behaviors, and it will be assumed to be materially homogeneous, and thermally heterogeneous (non-isothermal). Such definitions of material behaviors allow plaque model to be simpler structure over finite strains than those of soft tissues generally defined [79, 109].

C. Kinematics of Motion

The governing equations are developed for an elastic material undergoing a continuous growth process. This section is concerned with the kinematics to describe growth of incompressible elastic materials. After the introduction of the concepts of deformation gradient, the transformation of volume elements induced by a deformation is discussed.

In a simplification, the plaque growth is described by the volumetric production due to mass transfer in incompressible behavior through plaque domain. A growing material body, B, occupies a reference configuration $\beta_o(B)$ at time $t = 0$ and a configuration $\beta_t(B)$ at time t (Figure 58). A material particle of plaque body B occupies position $\mathbf{X}^o$ and $\mathbf{X}$ in these two configuration, respectively. The motion measured from a reference configuration β_o is given as

$$\mathbf{X} = \chi\left(\mathbf{X}^o, t\right),$$

with deformation gradient

$$\mathbf{F} = \frac{\partial \mathbf{X}}{\partial \mathbf{X}^o} = \frac{\partial \chi\left(\mathbf{X}^o, t\right)}{\partial \mathbf{X}^o}$$

where $\mathbf{F}$ is a second order tensor of deformation gradient. It is also invertible as

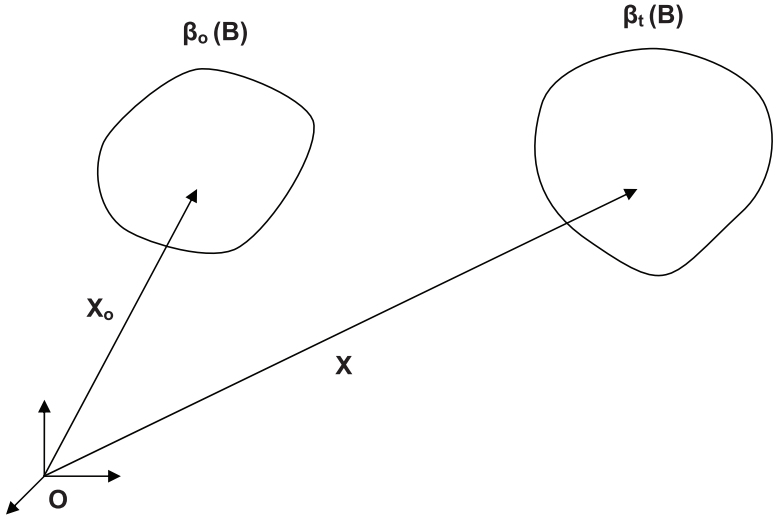

Fig. 58. Schematic of a material body in two configurations: **(1)** an initial reference configuration at time t=0 (β_o), and **(2)** a current configuration at time t=t (β_t). The position of a material body is given by X_o and X in each configuration, respectively.

$$\mathbf{F}^{-1} = \frac{\partial \mathbf{X}^o}{\partial \chi\left(\mathbf{X}^o, t\right)}$$

Position vector $d\mathbf{X}$ can be mapped from $d\mathbf{X}^o$ via a rigid body motion and deformation. If dV^o is a material element of volume at $\mathbf{X}^o$ and dV denotes its image under the mapping $\mathbf{X} = \chi\left(\mathbf{X}^o, t\right)$, we have

$$\begin{aligned} dV &= d\mathbf{X} \cdot (d\mathbf{X} \times d\mathbf{X}) \\ &= \mathbf{F} \cdot d\mathbf{X}^o \cdot (\mathbf{F} \cdot d\mathbf{X}^o \times \mathbf{F} \cdot d\mathbf{X}^o) \\ &= (det\mathbf{F})\, d\mathbf{X}^o \cdot (d\mathbf{X}^o \times d\mathbf{X}^o) \\ &= (det\mathbf{F})\, dV^o, \end{aligned}$$

where $det\mathbf{F}$ maps original differential volumes into current ones and is denoted by J; $J = det\mathbf{F}$. If the volume remains preserved throughout the deformation and growth ($dV = dV^o$), it is isochoric and densification ($J = 1$). In this study, as the deformation is assumed to have a volumetric growth in incompressible behavior ($\rho = \rho^o$), the volume is increased ($J > 1$).

Next, a differential area dS^o in a reference configuration β_o is mapped to area dS in current configuration β_t. Using the deformation gradient $\mathbf{F}$, the volume element dV is expressed by two ways as

$$dV = d\mathbf{X} \cdot (\mathbf{n}ds) = d\mathbf{X}^o \cdot \mathbf{F}^T \cdot (\mathbf{n}dS)\,, \tag{5.1}$$

$$dV = JdV^o = J\left(d\mathbf{X}^o \cdot (\mathbf{N}dS^o)\right). \tag{5.2}$$

Comparing Eq. 5.1 and Eq. 5.2, we find the following relation known as Nanson's relations.

$$\mathbf{N}dS^o = \frac{1}{J}\mathbf{n}dS \cdot \mathbf{F}, \tag{5.3}$$

where $\mathbf{N}$ and $\mathbf{n}$ are outward unit normal vector in area dS^o and dS. Nanson's relation is used to define stress acting over oriented areas. We define Cauchy stress σ [6] as presented by Truesdell and Noll [114].

$$\mathbf{T} = \sigma\mathbf{n}, \quad T_i = \sigma_{ij}n_j, \tag{5.4}$$

where σ is the stress tensor and $\mathbf{T}$ is the traction vector [7] that acts on that area. In

[6] Cauchy stress σ transforms the orientation $\mathbf{n}$ of area da of deformed solid (β_t) into the traction vector

[7] Traction vector $\mathbf{T}$ at the point P on the plane surface S is defined as $\mathbf{T} =$

the reference configuration β_o, the first Piola-Kirchhoff stress tensor $\mathbf{P}$ is defined by a new traction vector [8] $\mathbf{T}_o$ as

$$\mathbf{T}_o = \mathbf{P}\mathbf{N}, \tag{5.5}$$

where $\mathbf{N}$ is the unit normal vector in the reference configuration. Using Nanson's relation (Eq. 5.3) and the definitions of stress in Eqs. 5.4 and 5.5, we find that Cauchy stress is related to the first Piola-Kirchhoff stress $\mathbf{P}$, deformation gradient $\mathbf{F}$ and its determinant J as

$$\mathbf{n}dS \cdot \sigma = \mathbf{n}dS \cdot \frac{1}{J}\mathbf{F} \cdot \mathbf{P} \rightarrow \sigma = \frac{1}{J}\mathbf{F} \cdot \mathbf{P}. \tag{5.6}$$

Next, the velocity vector $\mathbf{v}$ and the velocity gradient tensor $\mathbf{L}$ are defined, respectively, as

$$\mathbf{v} = \frac{\partial \mathbf{X}}{\partial t} = \frac{\partial \chi\left(\mathbf{X}^o, t\right)}{\partial t} \quad \text{and} \quad \mathbf{L} = \frac{\partial \mathbf{v}}{\partial \mathrm{X}}$$

where $\mathbf{L}$ is rewritten by stretching tensor $\mathbf{D}$, symmetric part, and rotation tensor $\mathbf{W}$, antisymmetric part, as $\mathbf{L} = \mathbf{D} + \mathbf{W}$. If it is assumed that the plaque growth shows only stretching deformation as $\mathbf{L} = \mathbf{D}$, the material time derivative of $\mathbf{F}$ is expressed by

$$\frac{d\mathbf{F}}{dt} = \frac{\partial \mathbf{v}}{\partial \mathbf{X}} \cdot \frac{\partial \mathbf{X}}{\partial \mathbf{X}^o} = \nabla \mathbf{v} \cdot \mathbf{F} = (\mathbf{D} + \mathbf{W}) \cdot \mathbf{F} = \mathbf{D} \cdot \mathbf{F}. \tag{5.7}$$

where the stretching tensor is defined as $\mathbf{D} = \frac{d\mathbf{F}}{dt} \cdot \mathbf{F}^{-1}$. The time rate of J $(=det\mathbf{F})$ is evaluated with Eq. 5.7 (see [79], p. 78), which will be used in the fundamental

$\lim_{\Delta S \rightarrow 0} \frac{\Delta \mathbf{F}}{\Delta S}$ where $\Delta \mathbf{F}$ is the resultant force on a small area Δs on the surface s.

[8] New traction vector $\mathbf{T}_o$ in the reference configuration is defined by the actual force df and the reference area dS^o as $\mathbf{T}_o = \frac{df}{dS^o}$.

balance equations (e.g., mass, momentum, and energy),

$$\frac{dJ}{dt} = \frac{d(det\mathbf{F})}{dt} = \frac{\partial(det\mathbf{F})}{\partial\mathbf{F}} : \frac{d\mathbf{F}}{dt} = (det\mathbf{F}\mathbf{F}^{-T}) : (\mathbf{D}\cdot\mathbf{F}). \tag{5.8}$$

where the double dot (scalar) products between two second-order tensor are defined as $\mathbf{T}:\mathbf{S} = T_{ij}S_{ij}$. In this study, the alternate representation with different notations (see [79], p. 50) is used as $\mathbf{T}:\mathbf{S} = tr(\mathbf{T}\cdot\mathbf{S}^T) = tr(\mathbf{T}^T\cdot\mathbf{S})$. Thus, Eq. 5.8 becomes

$$\frac{dJ}{dt} = (det\mathbf{F})tr(\mathbf{F}^{-T}\cdot\mathbf{F}^T\cdot\mathbf{D}^T) = Jtr\mathbf{D}. \tag{5.9}$$

D. Mechanics of Solid with Growing Mass

This section introduces the fundamental relations of the balance of mass, momentum, and energy. The entropy inequality is presented, and it is utilized to derive the thermodynamic restrictions for the constitutive relations concerning the growth of atherosclerotic plaque due to mass transfer. These fundamental relations under isothermal processes obtained by many authors [79, 110, 115] are modified to describe the plaque growth under non-isothermal process. We mainly follow the forms proposed by Lubarda and Hoger [110], which uses the simpler formulations for tissue growth. The relations derived use the reference description [9] and the spatial description [10]. Energy equation is expressed in referential form.

[9] When a continuum is in motion, the change of specific particles (temperature θ, velocity $\mathbf{v}$, etc.) with time is described as functions of the particles (identified by the reference coordinates X_1^o, X_2^o, X_3^o) and time t. It is also known as **material description** and **Lagrangian description**.

[10] When a continuum is in motion, the change of specific particles (temperature θ, velocity $\mathbf{v}$, etc.) with time is described as functions of fixed position (identified by the spatial coordinates X_1, X_2, X_3) and time t. It is also known as **Eulerian description**.

1. Balance of mass

The balance of mass for the continuum with a growing mass considers the mass transport across the boundary and the mass creation by the internal sources in a fixed control volume. In the plaque domain, atherosclerotic plaque grows by the transfer of molecules through the boundary of plaque domain. The procedure to derive the mass balance follows Lubarda and Hoger's study [110]. A time rate of the mass growth per unit current volume r_g is defined in

$$\frac{d\,(dm)}{dt} = r_g dV. \tag{5.10}$$

where the subscript s presents the mass growth of plaque. The mass growth occurs when $r_g > 0$, and the mass is resorbed when $r_g < 0$. Plugging the mass density $\rho = dm/dV$ into Eq. 5.10, we obtain

$$\frac{d\rho}{dt} dV + \rho \frac{d\,(dV)}{dt} = r_g dV. \tag{5.11}$$

where the volume rate is the proportional to the divergence of velocity field as $\frac{d(dV)}{dt} = (\nabla \cdot \mathbf{v})\, dV$. Therefore, the balance of mass for the continuum with a growing mass is following

$$\frac{d\rho}{dt} + \rho \nabla \cdot \mathbf{v} = r_g. \tag{5.12}$$

Without the growing mass r_g, the standard balance of mass is derived. In this study, the plaque growth has a volumetric growth with incompressible materials as

$$\frac{d\rho}{dt} = 0, \quad \nabla \cdot \mathbf{v} = \frac{1}{\rho} r_g. \tag{5.13}$$

where the mass density ρ remains the initial density ρ_o as an atherosclerotic plaque

is growing.

a. Material form of growing mass

Determinant of deformation gradient $J = det\mathbf{F}$ was defined by dimensionless specific volume $J = \frac{dV}{dV^o}$ where dV is the initial volume element. The time rate of mass supply in Eq. 5.10 is expressed in referential form as

$$\frac{d\,(dm)}{dt} = \frac{d\,(\rho dV)}{dt} = \frac{d\,(\rho J dV^o)}{dt} = r_g J dV^o, \tag{5.14}$$

where the rate of mass growth per unit initial r_g^o is related with that of unit current volume r_g by the determinant of deformation gradient $r_g^o = r_g J$. Eq. 5.14 is rewritten in

$$\frac{d\,(\rho J)}{dt} = r_g^o. \tag{5.15}$$

Integrating on the time gives

$$\rho J = \rho^o J^o + \int_0^t r_g^o d\tau = \rho^o + \alpha, \tag{5.16}$$

where α denotes $\int_0^t r_g^o d\tau$ and J^o is omitted because $J^o = 1$. If the volume is preserved during the mass growth ($dV = dV^o$), $J = \frac{dV}{dV^o} = 1$. The densification is defined as

$$\rho = \rho^o + \alpha. \tag{5.17}$$

For simplicity, this study assumes that atherosclerotic plaque has a volumetric growth with incompressible behavior as $\rho = \rho^o$. The determinant of deformation gradient J for an incompressible material gives

$$J = 1 + \frac{\alpha}{\rho^o}, \tag{5.18}$$

2. Balance of momentum

The balance of momentum with a growing mass states that the rate of linear momentum of the material part is equal to the total force (surface and body forces) acting on the body plus the momentum rate associated with a growing mass. The first Euler's law of motion for the continuum with a growing mass is expressed in spatial form as [110]

$$\frac{d}{dt}\int_V \rho \mathbf{v} dV = \int_S \mathbf{T} dS + \int_V \rho \mathbf{b} dV + \int_V r_g \mathbf{v}_g dV, \tag{5.19}$$

where $\mathbf{v}$ is velocity vector of plaque body, $\mathbf{T}$ stress vector of surface force, $\mathbf{b}$ body force acting on the body in the current configuration (β_t), and $\mathbf{v}_g$ the velocity of molecules occurring the plaque growth. According to Reynolds transport theorem [11] for continuum with a growing mass (see [110]), the left-hand side in Eq. 5.19 is given in

$$\frac{d}{dt}\int_V \rho \mathbf{v} dV = \int_V \left(\rho \frac{d\mathbf{v}}{dt} + r_g \mathbf{v}\right) dV. \tag{5.20}$$

Using the definition of Cauchy stress (Eq. 5.4) and the divergence theorem [12], the

[11] Reynolds transport theorem states that the rate of change of any extensive property N of a system occupying a control volume C.V. at time t is equal to the sum of the rate of change of N within C.V. and the net flux of N through the control surface C.S. that surrounds the C.V.. The formula of Reynolds transport theorem for continuum with a growing mass in C.V. is $\frac{d}{dt}\int_V \rho A dV = \int_V \left(\rho \frac{dA}{dt} + r_g A\right) dV$ yielded in Lubarda and Hoger's study [110]

[12] The divergence theorem states that the flux of a vector field on a surface is equal to the triple integral of the triple integral of the divergence on the region inside the surface. The theorem is defined in $\int_S \mathbf{v} \cdot \mathbf{n} dS = \int_R div \mathbf{v} dV$

first term on the right-hand side in Eq. 5.19 is rewritten as a volume integral [116] by

$$\int_S \mathbf{T} dS = \int_S \sigma \mathbf{n} dS = \int_V (div\sigma)\, dV = \int_V (\nabla \cdot \sigma)\, dV. \tag{5.21}$$

Substitution of Eqs. 5.20 and 5.21 into Eq. 5.19 yields the balance of momentum for the growing mass as

$$\nabla \cdot \sigma + \rho \left(\mathbf{b} - \frac{d\mathbf{v}}{dt} \right) = r_g \left(\mathbf{v} - \mathbf{v}_g \right), \tag{5.22}$$

where $\mathbf{v}_g$ is the velocity of molecules in plaque domain, and $\mathbf{v}$ present the body velocity of plaque. If the molecules are moved with the velocity of plaque body ($\mathbf{v} = \mathbf{v}_g$), the familiar form of the linear momentum is obtained by

$$\nabla \cdot \sigma + \rho \mathbf{b} = \rho \frac{d\mathbf{v}}{dt}. \tag{5.23}$$

3. Balance of energy

Classically, the balance of energy (or the first law of thermodynamics) states that the time rate of the total energy (kinetic ($\frac{1}{2}\mathbf{v} \cdot \mathbf{v}$) plus internal energy ($u$)) of a body is equal to the rate at which work is done on the body and the rate at which heat is added to the body. This study invokes other terms related to the plaque growth and the metabolic heat generation in plaque; and it is given by [110]

$$\frac{\mathrm{d}}{\mathrm{d}t} \int_V \rho \left(\frac{1}{2} \mathbf{v} \cdot \mathbf{v} + u \right) \mathrm{d}V = \mathcal{W} + \mathcal{H} + \int_V r^g \left(\frac{1}{2} \mathbf{v}^g \cdot \mathbf{v}^g + u^g \right) \mathrm{d}V + \int_V \rho \mathcal{R}^g r^g \mathrm{d}V, \tag{5.24}$$

where the subscript g is the mass growth of plaque. The terms of $\frac{1}{2}\mathbf{v}^g \cdot \mathbf{v}^g$ and u^g present the kinetic and the internal energy of mass growth in plaque, respectively.

$\mathcal{R}^g r^g$ means the rate of chemical energy per unit current mass by plaque growth. Applying the Reynolds transport theorem to the term in left-hand side in Eq. 5.24 yields

$$\frac{d}{dt}\int_V \rho\left(\frac{1}{2}\mathbf{v}\cdot\mathbf{v}+u\right)dV = \int_V \rho\frac{d}{dt}\left(\frac{1}{2}\mathbf{v}\cdot\mathbf{v}+u\right)dV + \int_V r^g\left(\frac{1}{2}\mathbf{v}\cdot\mathbf{v}+u\right)dV. \quad (5.25)$$

The first term of right-hand side in Eq. 5.24 is the rate of work (force times velocity) done on the surface and body force on the current mass [111], and it is defined as

$$\mathcal{W} = \int_S \mathbf{T}\cdot\mathbf{v}\mathrm{d}S + \int_V \rho\mathbf{b}\cdot\mathbf{v}\mathrm{d}V, \quad (5.26)$$

where the rate of work done on the surface is transformed in terms of transpose of a tensor, $\sigma\mathbf{n}\cdot\mathbf{v} = \mathbf{n}\cdot\sigma^T\mathbf{v}$ (see [116], p. 433), into

$$\int_S \mathbf{T}\cdot\mathbf{v}dS = \int_S \sigma\mathbf{n}\cdot\mathbf{v}dS = \int_S \mathbf{n}\cdot\left(\sigma^T\mathbf{v}\right)dS. \quad (5.27)$$

Using the divergence theorem in Eq. 5.27, the rate of work done on the surface is

$$\int_S \mathbf{n}\cdot\left(\sigma^T\mathbf{v}\right)dS = \int_V \nabla\cdot\left(\sigma^T\mathbf{v}\right)dV = \int_V \left[(\nabla\cdot\sigma)\cdot\mathbf{v} + tr\left(\sigma^T\nabla\mathbf{v}\right)\right]dV, \quad (5.28)$$

where the velocity gradient $\nabla\mathbf{v}$ is substituted with $\mathbf{L}$ defined in the section of Kinetics. Using Eqs. 5.27 - 5.28, Eq. 5.26 becomes

$$\mathcal{W} = \int_V \left[(\nabla\cdot\sigma+\rho\mathbf{b})\cdot\mathbf{v} + tr\left(\sigma^T\mathbf{L}\right)\right]dV, \quad (5.29)$$

which, applying the linear momentum equation (Eq. 5.23), can be rewritten as

$$\mathcal{W} = \int_V \left[\rho\frac{d}{dt}\left(\frac{1}{2}\mathbf{v}\cdot\mathbf{v}\right) + tr\left(\sigma^T\mathbf{L}\right)\right]dV. \quad (5.30)$$

Here, the velocity gradient $\mathbf{L}$ is substituted with the stretching tensor $\mathbf{D}$ because the plaque is assumed to be growing without the rotational deformation $\mathbf{W}$, that is $tr\left(\sigma^T\mathbf{L}\right) = tr\left(\sigma^T\mathbf{D}\right)$. The trace operation of second order tensors are expressed by the scalar product (or double dot) between two second-order tensors as $tr\left(\sigma^T\mathbf{D}\right) = \sigma^T\!:\mathbf{D}$. The symmetry of the Cauchy stress tensor, $\sigma = \sigma^{\mathbf{T}}$, is valid if the plaque is assumed as an isotropic material as body moments per unit volume is ignored. Thus, Eq. 5.30 is rewritten by

$$\mathcal{W} = \int_V \left[\rho\frac{d}{dt}\left(\frac{1}{2}\mathbf{v}\cdot\mathbf{v}\right) + \sigma^T\!:\mathbf{D}\right] dV. \tag{5.31}$$

In Eq. 5.24, the rate of total heat input shows the heat input values of metabolic heat generation, which represent the inflammatory response taking place in the plaque. Using the divergence theorem, the rate of heat for a growing body is given by

$$\mathcal{H} = -\int_S \mathbf{q}\cdot\mathbf{n}dS + \int_V \rho w dV = \int_V \left(-\nabla\cdot\mathbf{q} + \rho w\right) dV, \tag{5.32}$$

where $\mathbf{q}$ is the rate of heat flow by conduction across the surface element $\mathbf{n}\mathrm{d}S$ of plaque domain, and w is the rate of heat input per unit current mass due to macrophage cell layer as an internal heat source.

The energy equation in the spatial form is yielded by plugging Eqs. 5.25, 5.31 and 5.32 into Eq. 5.24.

$$\rho\frac{du}{dt} = \sigma^T\!:\mathbf{D} - \nabla\cdot\mathbf{q} + \rho w + \rho\mathcal{R}^g r^g + r^g\left[\left(\frac{1}{2}\mathbf{v}^g\cdot\mathbf{v}^g + u^g\right) - \left(\frac{1}{2}\mathbf{v}\cdot\mathbf{v} + u\right)\right], \tag{5.33}$$

where ρw presents the rate of heat input per unit current mass produced by macrophage cell layer and $\rho\mathcal{R}^g r^g$ is the rate of chemical energy by mass growth. The last term of right-hand side vanishes with the assumptions: **(1)** the molecules transferred through

plaque surface causing plaque growth are deposited with the same velocity as that of the formation of plaque, (i.e. $\mathbf{v} = \mathbf{v}^g$) and **(2)** the internal energy u^g from molecules of the growing mass is the same as the internal energy u existing in the plaque, or their difference is negligible. Thus, the energy equation in spatial form is reduced to

$$\rho \frac{du}{dt} = \sigma^T : \mathbf{D} - \nabla \cdot \mathbf{q} + \rho w + \rho \mathcal{R}^g r^g. \tag{5.34}$$

To apply the entropy inequality in a more convenient way, the energy equation is changed into the referential form. The first term of the right-hand side of Eq. 5.34 is rewritten using the facts that **(1)** Cauchy stress σ is directly related to the first Piola-Kirchhoff stress $\mathbf{P}$ through deformation gradient $\mathbf{F}$ and its determinant J (Eq. 5.6), and **(2)** the relation between deformation gradient $\mathbf{F}$ and kinematics of deformation $\mathbf{D}$ is introduced (Eq. 5.7), and repeated below:

$$\sigma^T : \mathbf{D} = \frac{1}{J} \mathbf{F} \cdot \mathbf{P}^T : \frac{d\mathbf{F}}{dt} \cdot \mathbf{F}^{-1} = \frac{1}{J} \mathbf{P}^T : \frac{d\mathbf{F}}{dt} \tag{5.35}$$

Plugging Eq. 5.35 into Eq. 5.33, the referential form of energy equation is

$$\rho_o \frac{du}{dt} = \frac{1}{J} \mathbf{P}^T : \frac{d\mathbf{F}}{dt} - \nabla_o \cdot \mathbf{q_o} + \rho_o w + \rho_o \mathcal{R}^g r^g. \tag{5.36}$$

where ∇_o the referential dell operator and $\mathbf{q_o}$ the referential heat flux vector which arise from metabolic heat generation of inflammatory response.

4. Entropy inequality

The entropy inequality known as the second law of thermodynamics is essential for developing a constitutive relation. This study introduces the second law in the referential form modified with the Clausius-Duhem equation proposed by Bowen [112]. That is

$$-\rho_o \frac{du}{dt} + \frac{1}{J}\mathbf{P}^T : \frac{d\mathbf{F}}{dt} - \frac{1}{T}\mathbf{q_o} \cdot \nabla_o T + \rho_o w + \rho_o \mathcal{R}^g r^g \geq 0 \tag{5.37}$$

where the internal energy u is related to the Helmholtz potential Ψ and entropy η as $u = \Psi + \eta T$. The entropy inequality is rewritten by

$$-\rho_o \left(\frac{d\Psi}{dt} + \eta \frac{dT}{dt} \right) + \frac{1}{J}\mathbf{P^T} : \frac{d\mathbf{F}}{dt} - \frac{1}{T}\mathbf{q_o} \cdot \nabla_o T + \rho_o w + \rho_o \mathcal{R}^g r^g \geq 0 \tag{5.38}$$

For the case of isothermal process (*i.e.*, T constant and $\mathbf{q_o} = 0$), the entropy inequality in Eq. 5.38 reduces as

$$-\rho_o \frac{d\Psi}{dt} + \frac{1}{J}\mathbf{P^T} : \frac{d\mathbf{F}}{dt} \geq 0.$$

However, to consider thermal heterogeneity resulting from metabolic heat generation in atherosclerotic plaque, this study requires the use of the equation of non-isothermal process (Eq. 5.38).

E. Constitutive Equations

Constitutive relations describe a material's behavior under specific conditions of interest [79]. The constitutive law for stress-modulated growth of tissue is required to analyze the finite growth kinematics in an elastic tissue because the constitutive law determines the residual stress satisfying the equilibrium and boundary condition. Although the constitutive equations under isothermal process have been suggested during the past several decades [79, 117], those are inappropriate for the atherosclerotic plaque having thermal heterogeneity due to metabolic heat generation [3, 13, 14, 15, 16, 18, 19, 20]. Therefore, a new constitutive law under non-isothermal process is necessary to describe the growth of atherosclerotic plaque with metabolic

heat generation. The second law of thermodynamics in Eq. 5.38 suggests that three constitutive functions for a general thermoelastic process are in forms for Helmholtz potential Ψ, entropy η, and stress $\mathbf{P}$.

In this model, the atherosclerotic plaque exhibits incompressible volumetric growth ($\rho = \rho^o$) and the local volume change is measured by $det\mathbf{F}$ ($= J$). As shown in Eq. 5.18, the restrictions are imposed by the kinematic constraint[13] $det\mathbf{F} = 1 + \frac{\alpha}{\rho^o}$ for all $\mathbf{F}$. As the case of isothermal derived by Humphrey [79, 117], a Lagrange multiplier p is introduced to impose the constraint of the incompressible volumetric growth to the entropy inequality in Eq. 5.38.

$$\tilde{\Psi} = \Psi(\mathbf{F}) - p\left(det\mathbf{F} - 1 - \frac{\alpha}{\rho_o}\right) \tag{5.39}$$

where α is $\int_0^t r_g^o d\tau$. Helmholtz potential Ψ is the function of position (by deformation gradient) and temperature as $\Psi = \Psi(\mathbf{F}, T)$, and the Lagrange multiplier p depends on position and time t. Therefore,

$$\frac{d\tilde{\Psi}}{dt} = \frac{\partial\Psi}{\partial\mathbf{F}} : \frac{d\mathbf{F}}{dt} + \frac{\partial\Psi}{\partial T}\frac{dT}{dt} - \frac{dp}{dt}\left(J - 1 - \frac{\alpha}{\rho_o}\right) - p\frac{d}{dt}(J). \tag{5.40}$$

where the derivative of Ψ is taken by assuming each of the components of $\mathbf{F}$ to be independent (their dependence being accounted for via p). Plugging Eq. 5.40 and $J = det\mathbf{F}$ into Eq. 5.38, the inequality introduces

$$-\rho_o\left(\frac{\partial\Psi}{\partial\mathbf{F}} : \frac{d\mathbf{F}}{dt} + \frac{\partial\Psi}{\partial T}\frac{dT}{dt} - \frac{dp}{dt}\left(J - 1 - \frac{\alpha}{\rho_o}\right) - p\frac{dJ}{dt} + \eta\frac{dT}{dt}\right)$$
$$+\frac{1}{J}\mathbf{P}^T : \frac{d\mathbf{F}}{dt} - \frac{1}{T}\mathbf{q_o}\cdot\nabla_o T + \rho_o w + \rho_o^g\mathcal{R}^g r^g \geq 0,$$

[13]Kinematic constraints refer to internal mechanisms, operative under specific conditions, that are largely independent of the applied loads

which, using Eq. 5.9 to evaluate dJ/dt and $tr\mathbf{D} = \mathbf{F}^{-T}\colon \frac{d\mathbf{F}}{dt}$, becomes

$$-\rho_o\left(\frac{\partial\Psi}{\partial\mathbf{F}}\colon\frac{d\mathbf{F}}{dt}+\frac{\partial\Psi}{\partial T}\frac{dT}{dt}-\frac{dp}{dt}\left(J-1-\frac{\alpha}{\rho_o}\right)-pJ\mathbf{F}^{-\mathbf{T}}\colon\frac{d\mathbf{F}}{dt}+\eta\frac{dT}{dt}\right)$$
$$+\frac{1}{J}\mathbf{P}^T\colon\frac{d\mathbf{F}}{dt}-\frac{1}{T}\mathbf{q_o}\cdot\nabla_o T+\rho_o w+\rho_o^g\mathcal{R}^g r^g\geq 0,$$

and rearrange it to make scalar product for arbitrary $\mathbf{F}$, T and p

$$\left(-\rho_o\frac{\partial\Psi}{\partial\mathbf{F}}+\rho_o pJ\mathbf{F}^{-\mathbf{T}}+\frac{1}{J}\mathbf{P}^{\mathbf{T}}\right)\colon\frac{d\mathbf{F}}{dt}+\rho_o\left(J-1-\frac{\alpha}{\rho_o}\right)\frac{dp}{dt}-\rho_o\left(\frac{\partial\Psi}{\partial T}+\eta\right)\frac{dT}{dt}$$
$$-\frac{1}{T}\mathbf{q_o}\cdot\nabla_o T+\rho_o w+\rho_o^g\mathcal{R}^g r^g\geq 0. \tag{5.41}$$

where the values of $\frac{d\mathbf{F}}{dt}$, $\frac{dT}{dt}$ and $\frac{dp}{dt}$ could be separately positive, negative, or zero. Therefore, if the last three terms in right-hand side are positive in formal sign convention, three terms within parenthesis must vanish for the sufficient condition of Eq. 5.41 for any $\mathbf{F}$, T and p. The last three terms in right-hand side are evaluated to have positive sign with the followings: **(1)** when $\frac{dT}{dx}$ is a negative sign due to metabolic heat generation in plaque, $-\frac{1}{T}\mathbf{q_o}\cdot\nabla_o T$ has a positive sign. **(2)** The rate of heat input w per unit current mass produced by macrophage cell layer would be positive as $\rho_o w\geq 0$ **(3)** The rate of chemical energy by mass growth is also positive as $\rho_o^g\mathcal{R}^g r^g\geq 0$. As a result, three constitutive relations from Eq. 5.41 are yielded by

$$\mathbf{P}=\rho_o J\left(\frac{\partial\Psi}{\partial\mathbf{F}^T}-pJ\mathbf{F}^{-1}\right), \tag{5.42}$$

$$J=1+\frac{\alpha}{\rho_o}\quad\text{where}\quad\alpha=\int_0^{\mathrm{t}}\mathrm{r_g^o d}\tau, \tag{5.43}$$

$$\eta = -\frac{\partial \Psi}{\partial T}. \tag{5.44}$$

where the Lagrange multiplier p enforcing the incompressible volumetric growth (Eq. 5.43) introduces a reaction stress in Eq. 5.42. Three constitutive functions are necessary to describe the non-isothermal hyperelastic behavior of an atherosclerotic plaque.

In Eq. 5.42, the first Piola-Kirchhoff stress tensor $\mathbf{P}$ is derivable from the Helmholtz potential Ψ and the Lagrange multiplier p, which reveals that the Helmholtz potential and the stress are not independent on constitutive functions. Recalling the interrelations between the various forms of stress in Eq. 5.6, the Cauchy stress for a behavior of incompressible volumetric growth is

$$\sigma = \left(\frac{\alpha}{1-J}\right)\left(pJ\mathbf{I} - \mathbf{F}\cdot\frac{\partial \Psi}{\partial \mathbf{F}^T}\right). \tag{5.45}$$

where the term containing the Lagrange multiplier p is called the reaction term and the other term is called the extra stress. The second condition (Eq. 5.43) shows an incompressible behavior ($\rho = \rho^o$) during the mass growth of the atherosclerotic plaque. The third condition (Eq. 5.44) expresses that the entropy η and Helmholtz potential $\mathbf{\Psi}$ are related in a non-isothermal processes. In isothermal processes, the Helmholtz potential Ψ and the strain-energy W are simply related, (i.e. $\rho_o \mathbf{\Psi}(\mathbf{F}) = W(\mathbf{F})$), and stress is determined directly from a strain-energy function $W(\mathbf{F})$. Many empirical functional forms of strain-energy functions $W(\mathbf{F})$ has been achieved by evaluating the Helmholtz free energy at the fixed temperature at which deformation takes place. Meanwhile, there has been little evaluation of strain-energy function $W(\mathbf{F}, T)$ or Helmholtz free energy function $\Psi(\mathbf{F}, T)$ under non-isothermal process; Chadwick's study introduced the Helmholtz free energy function $\Psi(\mathbf{F}, T)$ to be valid for all elastic materials [118]. The entropy η (Eq. 5.44) is substituted for the equation

of the internal energy, $u = \Psi + \eta T$, defined by the Helmholtz potential Ψ and entropy η. Therefore,

$$u = \Psi - T\frac{\partial \Psi}{\partial T},$$

and the specific heat at constant deformation c is defined by

$$c = \frac{\partial u}{\partial T} = -T\frac{\partial^2 \Psi}{\partial T^2},$$

Integrating the specific heat c twice between reference temperature T_o and T (see [118], p. 32-41), the helmholtz free energy $\Psi(\mathbf{F}, T)$ is expressed by

$$\Psi(\mathbf{F}, T) = \Psi(\mathbf{F}, T_o)\frac{T}{T_o} - u(\mathbf{F}, T_o)\left(\frac{T}{T_o} - 1\right) - \int_{T_o}^{T}\left(\frac{T}{T'} - 1\right)c(\mathbf{F}, T')\,dT',$$

where the first term in the right-hand side, $\Psi(\mathbf{F}, T_o)$, presents the strain energy function per unit mass for isothermal deformation at the reference temperature T_o. For example, in his study [113], the form of the Helmholtz free energy function $\Psi(\mathbf{F}, T)$ for the behavior of rubberlike material in temperature range was discussed in detail.

F. Multiplicative Decomposition of Plaque Growth

Atherosclerotic plaque is grown with a volumetric growth through the mass transport of cellular species which depends on characteristics of blood flow and arterial geometries. During the growth, atherosclerotic plaque experiences temperature heterogeneity due to metabolic activation of inflammatory cells, which causes the deformation of plaque structure for thermal stress. As the soft-tissue growth showing large deformation is accompanied by residual stresses due to incompatible strains [106], the large deformation for the volumetric growth of plaque structure must consider the residual

stresses containing the thermal stress due to metabolic activations. According to the theory of plasticity, the stress modulated growth in arbitrarily large deformation can be appropriately explained by elastic-plastic decomposition of the deformation gradient [117]; the multiplicative decomposition of deformation gradient $\mathbf{F}$ is decomposed into its elastic $\mathbf{F}_e$ and growth $\mathbf{F}_g$ parts, that is $\mathbf{F} = \mathbf{F}_e \cdot \mathbf{F}_g$ [106, 107, 108, 109]. Likewise, the plaque body can undergo the growth without discontinuities through two processes: (1) the growth deformation $\mathbf{F}_g$ of material added and changed to the local stress-free state and (2) elastic deformation $\mathbf{F}_e$ to make the total growth deformation compatible [109, 110].

1. Plaque growth through mass transport

Atherosclerotic plaque is growing with mass transport of chemical and cellular species such as LDL, oxLDL, chemoattractant, immune cells (monocytes), inflammatory cells (macrophages), smooth muscle cells (MSC) and cellular debris that constitute necrotic core. The transient mass transport and accumulation of chemical species and cellular components are described by the convection-diffusion equations [44] as follows:

$$\frac{\partial \mathbf{C_i}}{\partial t} - \mathbf{D_{C_i}} \nabla^2 \mathbf{C_i} - R_{C_i} = 0 \quad \text{for} \quad i = 1, 2, 3, \tag{5.46}$$

$$\frac{\partial \mathbf{n_i}}{\partial t} - \mathbf{D_{n_i}} \nabla^2 \mathbf{n_i} - S_{n_i} = 0 \quad \text{for} \quad i = 1, 2, 3, \tag{5.47}$$

where $\mathbf{C}_i$ represents the solute concentration of chemical species such as LDL ($i = 1$), oxLDL ($i = 2$), and chemoattractant ($i = 3$). n_i denotes the cell number of cellular components such as monocytes ($i = 1$), smooth muscle cells ($i = 2$), macrophages ($i = 3$) and dead cells or debris cells ($i = 4$). For the simplicity in this study, all components related with the plaque formation have the same material properties.

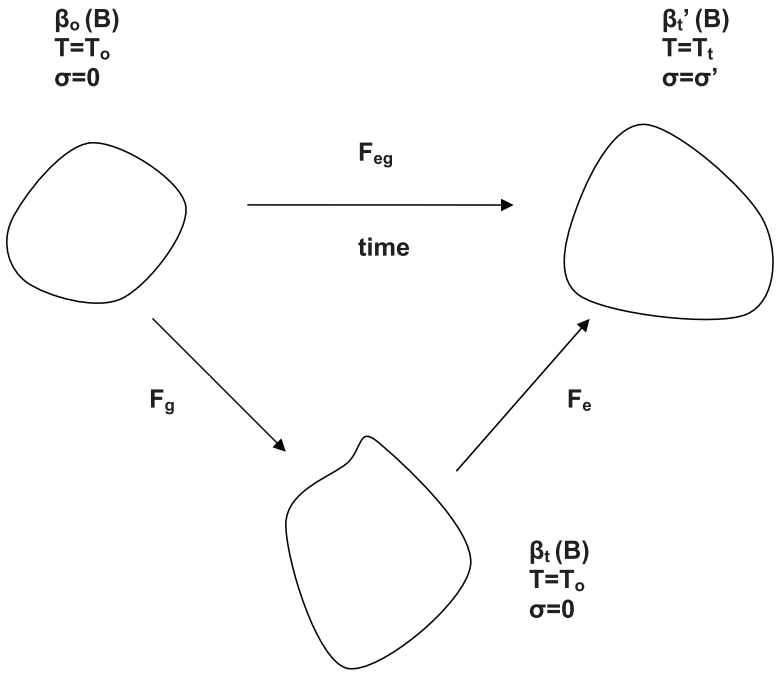

Fig. 59. Three states for the overall growth deformation in finite growth. **(a)** the initial zero-stress reference state $\beta_o(B)$ at the reference temperature T_o and time $t = 0$, **(b)** the grown zero-stress state $\beta_t(B)$ at the reference temperature T_o and time $t = t$, and **(c)** the grown unloaded state $\beta'_t(B)$ at the current temperature T_t and time $t = t$ where the residual stress σ' including the thermal stress caused by the temperature change from T_o to T_t. The growth deformation gradient $\mathbf{F}_g$ maps β_o into β_t, but may not be compatible the finite growth. The elastic deformation gradient $\mathbf{F}_e$ maps β_t into β'_t so that the overall growth deformation may be compatible.

2. Kinematics of plaque growth

As aforementioned, the overall growth deformation is decomposed into two parts: a transformation of growth $\mathbf{F}_g$ in zero-stress reference state, and an elastic deformation $\mathbf{F}_e$ with residual stress containing thermal stress to ensure the compatibility of the total growth deformation. For the growth deformation gradient $\mathbf{F}_g$ in Figure 59, the growth from the original zero-stress reference state $\beta_o(B)$ to a new locally stress-free state $\beta_t(B)$ is defined at reference temperature T_o as

$$\mathbf{F}_g = \mathbf{D} + \mathbf{W} \quad \text{at} \quad T_o \tag{5.48}$$

where $\mathbf{D}$ is the growth stretch tensor and $\mathbf{W}$ is the rotation tensor of the growth deformation. Because this study assumes that the growth law is formulated by the growth stretch $\mathbf{D}$, the growth deformation gradient is presented by $\mathbf{F}_g = \mathbf{D}$. Next, to ensure the continuity of the growing tissue, an elastic deformation $\mathbf{F}_e$ is applied to map $\beta_t(B)$ at reference temperature T_o to the state $\beta_t'(B)$ at current temperature T_t, which consider the residual stress σ' with thermal stress. So that the overall growth deformation is compatible, the elastic deformation $\mathbf{F}_e$ gives rise to the residual stress σ'.

$$\mathbf{F}_{eg} = \mathbf{F}_e \cdot \mathbf{F}_g \quad \text{at} \quad T_t \tag{5.49}$$

Here, the total deformation of atherosclerotic plaque $\mathbf{F}_{eg}$ experience temperature change from $\beta_o(B)$ at reference temperature T_o to $\beta_t'(B)$ at current temperature T_t.

3. Modeling of atherosclerotic plaque

A plaque model with macrophage cell layer shows how an atherosclerotic plaque gives a volumetric growth with the growth and elastic deformations. For the two-

dimensional plaque model, it is assumed that the plaque consists of fibrous cap (fc) and macrophage layer (mp) and has incompressible non-isothermal elastic behavior. The fibrous cap and macrophage layer are assumed to grow under two different linear functions. The macrophage layer along a longitudinal axis of vessel produces heat generation causing thermal stress that would affect additional deformation leading to plaque rupture.

Figure 60 describes the overall growth deformation $\mathbf{F}_{eg}$ of atherosclerotic plaque decomposed into two parts: **(1)** the growth deformation $\mathbf{F}_g$ and **(2)** elastic deformation $\mathbf{F}_e$. To describe the growth deformation $\mathbf{F}_g$, the fibrous cap and macrophage layer establishes two different growth deformations with different linear functions. If a point $\mathbf{p}$ in the original stress-free configuration $\beta_o(B)$ at reference temperature T_o has the coordinates (R, Θ), the growth deformation $\mathbf{F}_g$ maps the original state $\beta_o(B)$ into the new locally stress-free state $\beta_t(B)$, in which $\mathbf{p}$ has coordinates (ρ, φ) at reference temperature T_o. It is prescribed by the growth displacements in Eqs. 5.50 and 5.51.

$$\rho_{fc} = P_{fc}(R)\, R, \quad \varphi_{fc} = K_{fc}(R)\, \Theta, \tag{5.50}$$

$$\rho_{mp} = P_{mp}(R)\, R, \quad \varphi_{mp} = K_{mp}(R)\, \Theta. \tag{5.51}$$

where the subscripts of fc and mp present the fibrous cap and the macrophage layer, respectively. The term $P(R)$ is a radial growth stretch ratio and $K(R)$ is a circumferential growth stretch ratio that depends on the radius. As $P(R) > 1.0$ and $K(R) > 1.0$, the growth deformation $\mathbf{F}_g$ is occurred as shown in Figure 60, meanwhile when $P(R) < 1.0$ and $K(R) < 1.0$, the deformation is resorbed. At locally stress-free state $\beta_t(B)$, the plaque and macrophage layer have a superposition or discontinuity

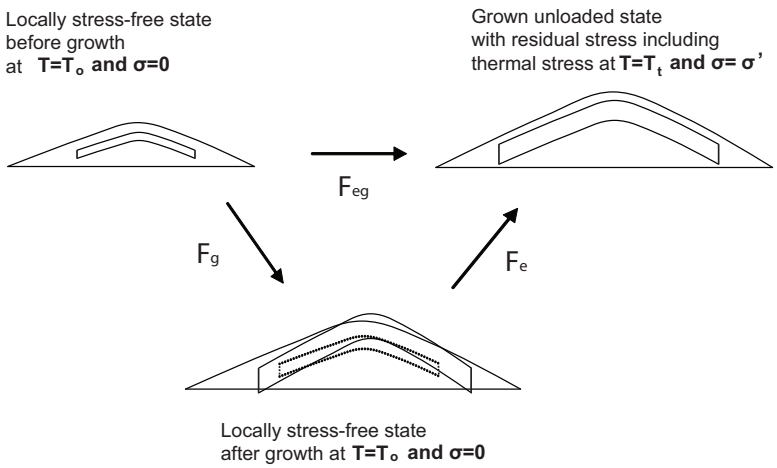

Fig. 60. The growth model of atherosclerotic plaque. The original zero-stress is a smaller plaque before growing at time $t = 0$ and temperature T_o. After growing process $\mathbf{F}_g$, the grown state β_t in stress-free has deformation but shows discontinuity between macrophage layer and fibrous part. To achieve a complete plaque shape, an elastic deformation $\mathbf{F}_e$ takes two different-grown parts β_t at T_o into compatible grown state β_t' at current temperature T_t. This elastic deformation $\mathbf{F}_e$ will give rise to residual stress σ' which include the thermal stress due to the temperature change from T_o to T_t.

of material at the interface region of two materials.

For compatibility of the overall growth deformation in finite elasticity, an elastic growth deformation $\beta_t'(B)$ experiences the residual stress considering thermal stress due to the temperature change from the reference temperature T_o to the current temperature T_t. The state $\beta_t(B)$ at T_o is mapped to the final state of $\beta_t'(B)$ at T_t where $\mathbf{p}$ has coordinates (r, θ). The elastic displacements for fibrous cap and macrophage layer are prescribed as;

$$r_{fc} = h_{fc}(\rho)\,\rho, \quad \theta = g_{fc}(\rho)\,\varphi, \tag{5.52}$$

$$r_{mp} = h_{mp}(\rho)\,\rho, \quad \theta = g_{mp}(\rho)\,\varphi. \tag{5.53}$$

where $h(\rho)$ is a radial elastic ratio and $g(\rho)$ is a circumferential elastic ratio, which are chosen to allow the overall growth deformation $\mathbf{F}_e \cdot \mathbf{F}_g$ to be compatible at the interface between the fibrous cap (fc) and the macrophage layer (mp). For example, if P_{fc} and K_{fc} are constant, simply the functions are $h_{fc} = 1/P_{fc}$ and $g_{fc} = 1/K_{fc}$ to be compatible by restoring continuity of displacements at the interface. The elastic deformation will be considered by the constitutive equation which determines the residual stress of the plaque material that must satisfy equilibrium and the zero traction boundary condition. The constitutive equations under non-isothermal process was already introduced in the previous chapter.

G. Conclusions of Plaque Evolution

This chapter presented a constitutive relation of thermal-stress modulated growth of atherosclerotic plaque with large deformation of two components, such as fibrous cap (fc) and macrophage layer (mp). The governing equations of the solid mechanics with

a volumetric growth were formulated with the balance of mass, momentum, energy and entropy under non-isothermal process, which was given in the framework of finite deformations. The constitutive relations (Equations 5.42 - 5.44) of the non-isothermal process were developed by extending the classical Clausius-Duhem (CD) inequality. Subsequently, the atherosclerotic plaque model in terms of the thermal-stress modulated growth was described by the constitutive relations of non-isothermal process. The model of plaque growth adopted the theory of the multiplicative decomposition of the deformation gradient into its elastic and growth parts. The deformation of plaque components, fibrous cap (fc) and macrophage layer (mp), had a volumetric and linear growth with an isotropic behavior. In the model, the non-isothermal process due to thermal heterogeneity was required with the hypothesis; temperature increase by inflammatory process in macrophage layer might cause thermal stress that contributes to weakening of the sensitive plaque surface including enzymatic degradation of the connective tissue matrix. This might directly affect endothelium permeability to increase the transport of macromolecules and, consequently cause the evolution of atherosclerosis and plaque growth.

There are still many improvements necessary. The 2-D simplified model that expresses the growth of atherosclerotic plaque should be modified for the realistic model in accordance with the experimental observations for the plaque structure and components properties, which is the essential part of further research. Nevertheless, this basic model of a plaque growth may become the first discussion in regard to non-isothermal process due to thermal stress. The governing equations derived and theoretical concepts developed herein can provide the comprehensive information to more realistic numerical model to analyze the growth of an atherosclerotic plaque. This description might be a useful to understand how temperature increase by inflammatory process could affect the growth of atherosclerotic plaque.

REFERENCES

[1] X.M. Yuan, U.T. Brunk, and L. Hazell, "The morphology and natural history of atherosclerosis," in *Atherosclerosis, Gene Expression, Cell Interactions and Oxidation*. Roger T. Dean and David T. Kell, 1st Ed., New York, Oxford University Press, 2000, chap.12, pp. 490–522.

[2] American Heart Association, *2006 Heart Disease and Stroke Statistics - 2006 Update*, Dallas, TX: American Heart Association, 2006.

[3] M. Naghavi, M. Madjid, K. Gul, M.S. Siadaty, S. Litovsky, J.T. Willerson, and S. W. Casscells, "Thermography basket catheter: In vivo measurement of the temperature of atherosclerotic plaques for detection of vulnerable plaques," *Catheterization and Cardiovascular Interventions*, vol. 59, pp. 52–59, 2003.

[4] R. Virmani, F.D. Kolodgie, A.P. Burke, A. Farb, S. M. Schwartz, "Lessons from sudden coronary death: a comprehensive morphological classification scheme for atherosclerotic lesions," *Arterioscler Thromb. Vasc. Biol.*, vol. 20, pp. 1262–1275, 2000.

[5] R.A. Baldewsing, J.A. Schaar, F. Mastik, C.W.J. Oomens, and A.F.W. van der Steen, "Assessment of vulnerable plaque composition by matching the deformation of a parametric plaque model to measured plaque deformation," *IEEE Transaction on Medical Imaging*, vol. 24, pp. 514–528, 2005.

[6] D. Tang, C. Yang, J. Zheng, P.K. Woodard, J.E. Saffitz, G.A. Sicard, T.K. Pilgram, and C. Yuan, "Quantifying effects of plaque structure and material properties oon stress distributions in human atherosclerotic plaques using 3D

FSI models," *Journal of Biomechanical Engineering*, vol. 127, pp. 1185–1194, 2005.

[7] B.D. MacNeill, H.C. Lowe, M. Takano, V. Fuster, and I. Jang, "Introvascular modalities for detection of vulnerable plaque; current status," *Arterioscler Thromb Vasc Biol*, vol. 23, pp. 1333–1342, 2003.

[8] E. Falk, "Morphologic features of unstable atherothrombotic plaques underlying acture coronary syndromes," *Am. J. Cardiol*, vol. 63, pp. 114E–120E, 1989.

[9] E.Falk, P.K. Shah, and V. Fuster, "Coronary plaque disruption," *Circulation*, vol. 92, pp. 657–671, 1995.

[10] W.C. Little, M. Constantinescu, R.J. Applegate, M.A. Kutcher, M.T. Burrows et al., "Can coronary angiography predict the site of a subsequent myocardial infarction in patients with mild-to-moderate coronary artery disease?," *Circulation*, vol. 78, pp. 1157–1166, 1988.

[11] A. Farb, A.L. Tang, and A.P. Burke, "Sudden coronary death. Frequency of active coronary lesions, inactive coronary lesions, and myocardial infarction," *Circulation*, vol. 92, pp. 1701–1709, 1995.

[12] W. Casscells, B. Hathorn, M. David, T. Krabach, W.K. Vaughn, H.A. McAllister, and G. Bearman, "Thermal detection of cellular infiltrates in living atherosclerotic plaques: possible implications for plaque rupture and thrombosis," *The LANCET*, vol. 347, pp. 1447–1449, 1996.

[13] C. Stefanadis, L. Diamantopoulos, C. Vlachopoulos, E. Tsiamis, J. Dernellis, K. Toutouzas, E. Stefanadi, and P. Toutouzas, "Thermal heterogeneity within

human atherosclerotic coronary arteries detected in vivo; A new method of detection by application of a special thermography catheter," *Circulation*, vol. 99, pp. 1965–1971, 1999.

[14] S. Verheye, G.R.Y. De Meyer, G. Van Lanenhove, M.W.M. Knaapen, and M.M. Kockx, "In vivo temperature heterogeneity of atherosclerotic plaquesis determined by plaque composition," *Circulation*, vol. 105, pp. 1596–1601, 2002.

[15] M. Madjid, M. Naghavi, B.A. Malik, S. Litovsky, J.T. Wilerson, and W. Casscells, "Thermal detection of vulnerable plaque," *American Journal of Cardiology*, vol. 90, pp. 36L–39L, 2002.

[16] C. Stefanadis, K. Toutouzas, M. Vavuranakis, E. Tsiamis, S. Vaina, and P. Toutouzas, "New balloon-thermography catheter for in vivo temperature measurements in human coronary atherosclerotic plaques: A novel approach for thermography?," *Catheterization and Cardiovascular Interventions*, vol. 58, pp. 344–350, 2003.

[17] D. Nemirovsky, "Imaging of high-risk plaque," *Cardiology*, vol. 100, pp. 160–175, 2003.

[18] V. Bhatia, R. Bhatia, S. Dhindsa, and M. Dhindsa, "Imaging of the vulnerable plaque: New modalities," *Southern Medical Journal*, vol. 96(11), pp. 1142–1147, 2003.

[19] L. Diamantopoulos, "Arterial wall thermography," *Journal of Interventional Cardiology*, vol. 16(3), pp. 261–266, 2003.

[20] L. Diamantopoulos, X. Liu, I.D. Scheerder, R. Krams, S. Li, J.V. Cleemput, W. Desmet, and P.W. Serruys,"The effect of reduced blood-flow on the coronary wall

temperature: Are significant lesions suitable for intravascular thermography?," *European Heart Journal*, vol. 24, pp. 1788–1795, 2003.

[21] C. Stefanadis, K. Toutouzas, E. Tsiamis, I. Mitropoulos, C. Tsioufis, I. Kallikazaros, C. Pitsavos, P. Toutouzas, "Thermal heterogeneity in stable human coronary atherosclerotic plaques is underestimated in vivo: the 'cooling effect' of blood flow," *Journal of the American College of Cardioloy*, vol. 41, pp. 403–408, 2003.

[22] J.F. Green, *Fundamental Cardiovascular and Pulmonary Physiology, An Integrated Approach for Medicine*, Philadelphia: LEA and FEBIGER, 1982.

[23] J.J. Smith and J.P. Kampine, *Circulatory Physiology*, Baltimore, MD: Williams and Wilkins, 1980.

[24] J.M. Tarbell and Y.Qiu, "Arterial wall mass transport: The possible role of blood phase resistance in the localization of arterial disease," in *The Biomedical Engineering Handbook* . J.D. Bronzino, 2nd Ed., Boca Raton, FL: CLC Press LLC, 2000, chap. 100.

[25] A.M. Malek, S.L. Alper, and S. Izumo, "Hemodynamic shear stress and its role in atherosclerosis," *JAMA*, vol. 282, pp. 2035–2042, 1999.

[26] C.R. Ethier, "Computational modeling of mass transfer and links to atherosclerosis," *Annals of Biomedical Engineering*, vol. 30, pp. 461–471, 2002.

[27] R. Ross, "Atherosclerosis - an inflammatory disease," *Mechanism of Disease*, vol. 340(2), pp. 115–126, 1999.

[28] A.C. Langheinrich, A. Michniewicz, D.G. Sedding, G. Walker, P.E. Beighley, W.S. Rau, R.M. Bohle, and E.L. Ritman, "Correlation of vasa vasorum neo-

vascularization and plaque progression in aortas of apolipoprotein $E^{-/-}$ / low-density lipoprotein$^{-/-}$ double knockout mice," *Arterioscler Thromb Vasc Biol*, vol. February, pp. 347–352, 2006.

[29] M. Gossl, D. Versari, D. Mannheim, E.L. Ritman, L.O. Lerman and A. Lerman, "Increased spatial vasa vasorum density in the proximal LAD in hypercholesterolemia - Implications for vulnerable plaque-development," *Atherosclerosis*, vol. 192, pp. 246–252, 2007.

[30] D.E. Gutstein and V. Fuster, "Pathophyiology and clinical significance of atherosclerotic plaque rupture," *Cardiovascular Research*, vol. 41, pp. 323–333, 1999.

[31] W. Jessup, A. Baoutina, and L. Kritharides, "Macrophages in cardiovascular disease," in *The Macrophage*. B. Burke and C.E. Lewis, 2nd Ed., New York: Oxford University Press, 2002, chap.1, pp. 1–23.

[32] C.K. Zarins, D.P. Giddens, B.K. Bharadvaj, V.S. Sottiurai, R.F. Mabon and S. Glagov, "Carotid bifurcation atherosclerosis: Quantitative correlation of plaque localization with flow velocity profiles and wall shear stress," *Circulation Research*, vol. 53, pp. 502–514, 1983.

[33] S.D. Gertz and W.C. Roberts, "Hemodynamic shear force in rupture of coronary arterial atherosclertic plaques," *Am. J. Cardiol.*, vol. 66, pp. 1368–1372, 1990.

[34] B.K. Bharadvaj, R.F. Maron, and D.P. Giddens, "Steady flow in a model of the human carotid bifurcation, I: flow visualization," *Journal of Biomechanics*, vol. 28, pp. 1515–1528, 1995.

[35] A. Gnasso, C. Irace, C. Carallo, M.S. De Franceschi, C. Motti, P.L. Mattioli

and A. Pujia, "In vivo association between low wall shear stress and plaque in subjects with asymmetrical carotid atherosclerosis," *Stroke*, vol. 28, pp. 993–998, 1997.

[36] G.C. Cheng, H.M. Loree, R.D. Kamm, M.C. Fishbein and R.T. Lee, "Distribution of circumferential stress in ruptured and stable atherosclerotic lesions," *Circulation*, vol. 87(4), pp. 1179–1187, 1993.

[37] H.M. Loree, R.D. Kamm, R.G. Stringfellow and R.T. Lee, "Effects of fibrous cap thickness on peak circumferential stress in model atherosclerotic vessels," *Circulation Research*, vol. 71, pp. 850–858, 1992.

[38] P.D. Richardson, M.J. Davies and G.V.R. Born, "Influence of plaque configuration and stress distribution on fissuring of coronary atherosclerotic plaques," *LANCET*, vol. 334, pp. 941–944, 1989.

[39] R.A. Baldewsing, F. Mastik, J.A. Schaar, P.W. Serruys, P W and A.F. van der Steen, "Young's modulus reconstruction of vulnerable atherosclerotic plaque components using deformable curves," *Ultrasound in Medicine & Biology*, vol. 32, pp. 201–210, 2006.

[40] H. Guretzki, K. Gerbitz, B. Olgemoller, and E. Schleicher, "Atherogenic levels of low density lipoprotein alter the permeability and composition of the endothelial barrier," *Atherosclerosis*, vol. 107, pp. 15–24, 1994.

[41] D.K. Stangeby and C.R. Ethier, "Computational analysis of coupled blood-wall arterial LDL transport," *Journal of Biomechanical Engineering*, vol. 124, pp. 1–8, 2002.

[42] D.K. Stangeby and C.R. Ethier, "Coupled computational analysis of arterial

LDL transport. Effects of hypertension," *Computer Methods in Biomechanics and Biomedical Engineering*, vol. 5, pp. 223–241, 2002.

[43] P. Libby, "Pathophysiology of the atheroma and mechanisms of plaque rupture," *The 64th Annual Scientific Meeting of the Japanese Circulation Society*, Osaka, Japan, 1–3 April, 2000.

[44] A.I. Ibragimov, C.J. McNeal, L.R. Ritter, and J.R. Walton, "A mathematical model of atherogenesis as an inflammatory response," *Mathematical Medicine and Biology*, vol. 22, pp. 305–333, 2005.

[45] G. Rappitsch and K. Perktold, "Pulsatile albumin transport in large arteries: A numerical simulation study," *Journal of Biomechanical Engineering*, vol. 118, pp. 511–519, 1996.

[46] S. Wada and T. Karino, "Theoretical prediction of low-density lipoproteins concentration at the luminal surface of an artery with a multiple bend," *Annals of Biomedical Engineering*, vol. 30, pp. 778–791, 2002.

[47] T. Asakura and T. Karino, "Flow patterns and spatial distribution of atherosclerotic lesions in human coronary arteries," *Circ. Res.*, vol. 66, pp. 1045–1066, 1990.

[48] K. Perktold, M. Resch, and R. O. Peter, "Three-dimensional numerical analysis of pulsatile flow and wall shear stress in the carotid artery bifurcation," *Journal of Biomechanics*, vol. 24, pp. 409–420, 1991.

[49] N. Filipovic, and M. Kojic, "Computer Simulations of blood flow with mass transport through the carotid artery bifurcation," *Theoret.Appl. Mech.*, vol. 31, pp. 1–33, 2004.

[50] C.G. Caro, T.J. Pedley, R.C. Schroter, and W.A. Seed, *The Mechanics of the Circulation*, New York: Oxford University Press, 1978.

[51] K. Perktold, M. Hofer, G. Rappitsch, M. Loew, B. D. Kuban, M. H. Friedman, "Validated computation of physiologic flow in a realistic coronary artery branch," *Journal of Biomechanics*, vol. 31, pp. 217–228, 1998.

[52] G. Pontrelli, "Pulsatile blood flow in a pipe," *Computers and Fluids*, vol. 27, pp. 367–380, 1998.

[53] D.N. Ku, "Blood flow in arteries," *Annu. Rev. Fluid Mech.*, vol. 29, pp. 399–434, 1997.

[54] K. Perktold and G. Rappitsch, "Computer simulation of local blood flow and vessel mechanics in a complaint carotid artery bifurcation model," *Journal of Biomechanics*, vol. 28, pp. 845–856, 1995.

[55] A.J. Carter and W. Wei, "Emerging animal models of the vulnerable plaque," in *Handbook of the Vulnerable Plaque*. R. Waksman and P. W. Srruys, 1st Ed., London, United Kingdom: Taylor and Francis, 2004, chap.8, pp. 153–171.

[56] R. Virmani, A. Burke, A. Farb, F. D. Kolodgie, A. V. Finn, and H. Gold, "Pathology of the vulnerable plaque," in *Handbook of the Vulnerable Plaque*. R. Waksman and P. W. Srruys, 1st Ed., London, United Kingdom: Taylor and Francis, 2004, chap.3, pp. 33–48.

[57] F. Colbourne, and D. Corbett, "Lessons from sudden coronary death: A comprehensive morphological classification scheme for atherosclerotic lesions," *Arterioscler Thromb Vasc Biol*, vol. 20, pp. 1262–1265, 2000.

[58] F. Mallinger and D. Drikakis, "Instability in three-dimensional, unsteady, stenotic flows," *International Journal of Heat and Fluid Flow*, vol. 23, pp. 657–663, 2002.

[59] B.M. Johnston, P.R. Johnston, S. Corney, D. Kilpatrick, "Non-Newtonian blood flow in human right coronary arteries: Transient simulations," *Journal of Biomechanics*, vol. 39, pp. 1116–1128, 2006.

[60] D. Zeng, Z. Ding, M.H. Friedman, and C.R. Ethier, "Effects of cardiac motion on right coronary artery hemodynamics," *Annals of Biomedical Engineering*, vol. 31, pp. 420–429, 2003.

[61] Y. Liu, Y. Lai, A. Nagaraj, B. Kane, A. Hamilton, R. Greene, D.D. McPherson and K.B. Chandran, "Pulsatile flow simulation in arterial vascular segments with intravascular ultrasound images," *Medical Engineering and Physics*, vol. 23, pp. 583–595, 2001.

[62] M. Zamir, *The Physics of Pulsatile Flow*, New York: AIP Press, 2000.

[63] F.A. Duck, *Physical Properties of Tissue: A Comprehensive Reference Book*, vol. 1, San Diego, CA: Academic Press, 1990.

[64] A. J. Welch and M.J.C. Van Gemert, *Optical Thermal Response of Laser-Irradated Tissue*, vol. 1, New York: Plenum, 1995.

[65] J.W. Valvano and B. Chitsabesan, "Thermal conductivity and diffusivity of arterial wall and atherosclerotic plaque," *Lasers in the Life Sciences*, vol. 1, pp. 219–229, 1987.

[66] J. Ross and M. Auger, "The biology of the macrophage," in *The Macrophage*. B. Burke and C.E. Lewis, 2nd Ed., New York: Oxford University Press, 2002,

chap.1, pp. 1–23.

[67] S.A. Thoren, M. Monti, and B. Holma, "Heat conduction microcalorimetry of overall metabolism in rabbit alveolar macrophages in monolayers and in suspensions," *Biochimica et Biophysica Acta*, vol. 1033, pp. 305–310, 1990.

[68] G. Rappitsch and K. Perktold, "Computer simulation of convective diffusion processes in large arteries," *Journal of Biomechanics*, vol. 29, pp. 207–215, 1996.

[69] L.D. Jou, R. van Tyen, S.A. Berger, and D. Saloner, "Calculation of the magnetization distribution for fluid flow in curved vessels," *Magnetic Resonance in Medicine*, vol. 35, pp. 577–584, 1996.

[70] D.W. Crowder and P.Diplas, "Vorticity and circulation: spatial metrics for evaluating flow complexity in stream habitats," *Can. J. Fish Aquat. Sci.*, vol. 59, pp. 633–645, 2002.

[71] J.B. Umland and J.M. Bellama, *General Chemistry*, Pacific Grove, CA: Brooks and Cole Publishing Company, 2nd Ed., 2000.

[72] D.A. McDonald, *Blood Flow in Arteries*, London: Edward Arnold, 2nd Ed., 1974.

[73] F.J.H. Gijsen, E. Allanic, F. N. Vosse, J. D. Janssen, "The influence of the non-Newtonian properites of blood on the flow in large arteries: unsteady flow in a 90^o curved tube," *Journal of Biomechanics*, vol. 32, pp. 705–713, 1999.

[74] J. Chen and X.Y. Lu, "Numerical investigation of the non-Newtonian pulsatile blood flow in a bifurcation model with a non-planar branch," *Journal of Biomechanics*, vol. 39, pp. 818–832, 2005.

[75] C. Stefanadis, K. Toutouzas, E. Tsiamis, M. Vavuranakis, I. Kallikazaros, P. Toutouzas, "Thermography of human arterial system by means of new thermography catheter," *Catheterization and Cardiovascular Interventions,* vol. 54, pp. 51–58, 2001

[76] O. Ley and T. Kim, "Numerical prediction of atherosclerotic plaque temperature as function of plaque size and composition," *2005 ASME International Mechanical Engineering Congress and Exposition*, Orlando, Florida, USA, 5–11 November, 2005.

[77] O. Ley and T. Kim, "Calculation of arterial wall temperature in atherosclerotic arteries: Effect of pulsatile flow, arterial geometry, and plaque structure," *Biomedical Engineering Online*, 2006.

[78] O. Ley and T. Kim, "Determination of atherosclerotic plaque temperature in large arteries," *International Journal of Thermal Sciences*, In press (THESCI-D-06-00348), 2007.

[79] J.D. Humphrey, *Cardiovascular Solid Mechanics; Cells, Tissues, and Organs*, New York: Springer, 2002.

[80] H.W. Weizsacker and J.G. Pinto, "Isotropy and anisotropy of the arterial wall," *Journal of Biomechanics*, vol. 21, pp. 477–487, 1988.

[81] R.A. Baldewsing, C.L. de Korte, J.A. Schaar, F. Mastik and A.F.W. van der Steen, "Finite element modeling and intravascular ultrasound elastography of vulnerable plaques: Parameter variation," *Ultrasonics*, vol. 42, pp. 723–729, 2004.

[82] H. Kanai, H. Hasegawa, M. Ichiki, F. Tezuka, and Y. Koiwa, "Elasticity imaging

of atheroma with transcutaneous ultrasound: Preliminary study," *Circulation*, vol. 107, pp. 3018–3021, 2003.

[83] K.B. Chandran, J.H. Mun, K.K. Choi, J.S. Chen, A. Hamilton, A. Nagaraj, and D.D. McPherson, "A method for in-vivo analysis for regional arterial wall material peroperty alterations with atherosclerosis: Preliminary results," *Med. Eng. Phys.*, vol. 25, pp. 289–298, 2003.

[84] M. Wan, Y. Li, J. Li, Y. Cui and X. Zhou, "Strain imaging and elasticity reconstruction of arteries based on intravascular ultrasound video images," *IEEE Trans. Biomed. Eng.*, vol. 48(1), pp. 116–120, 2001.

[85] D.J. Patel, J.S. Janicki and T.E. Carew, "Static anisotropic elastic properties of the aorta in living dogs," *Circ Res*, vol. 25, pp. 765–779, 1969.

[86] W.W. von Maltzahn, R.G. Warriyar, and W.F. Keitzer, "Experimental measurements of elasticd properties of media and adventitia of bovine carotid arteries," *Journal of Biomechanics*, vol. 17, pp. 839–847, 1984.

[87] C.J. Chuong, and Y.C. Fung, "On residual stress in arteris," *ASME J. Biomech. Eng.*, vol. 108, pp. 189–192, 1986.

[88] K. Takamizawa, and K. Hayashi, "Strain energy density function and uniform strain hypothesis for arterial mechanics," *Journal of Biomechanics*, vol. 20, pp. 7–17, 1987.

[89] K. Hayashi and Y. Imai, "Tensile property of atheromatous plaque and an analysis of stress in atherosclerotic wall," *Journal of Biomechanics*, vol. 30, pp. 573–579, 1997.

[90] R.T. Lee, H.M. Loree, G.C. Cheng, E.H. Lieberman, N. Jaramillo and F.J. Schoen, "Computational structural analysis based on intravascular ultrasound imaging before in vitro angioplasty: Prediction of plaque fracture locations," *J. Am. Coll. Cardiol.*, vol. 21, pp. 777–782, 1993.

[91] S.L. Mautner, F. Lin and W.C. Roberts, "Composition of atherosclerotic plaques in the epicardial coronary arteries in juvenile (type I) diabetes mellitus," *Am. J. Cardiol.*, vol. 70, pp. 1164–1168, 1992.

[92] R.P. Vito and S.A. Dixon, "Blood vessel constitutive models - 1995-2002," *Annu. Rev. Biomed. Eng.*, vol. 5, pp. 413–439, 2003.

[93] G. Finet, J. Ohayon and G. Rioufol, "Biomechanical interaction between cap thickness, lipid core composition and blood pressure in vulnerable coronary plaque: Impact on stability or instability," *Coronary Artery Disease*, vol. 15, pp. 13–20, 2004.

[94] H. Huang, R. Virmani, H. Younis, A.P. Burke, R.D. Kamm and R.T. Lee, "The impact of calcification on the biomechanical stability of atherosclerotic plaques," *Circulation*, vol. 103, pp. 1051–1056, 2001.

[95] H.M. Loree, B.J. Tobias, L.J. Gibson, R.D. Kamm, D.M. Small and R.T. Lee, "Mechanical properties of model atherosclerotic lesion lipid pools," *Arterioscler. Thromb.*, vol. 14, pp. 230–234, 1994.

[96] R.T. Lee, H.M. Loree and M.C. Fishbein, "High stress regions in saphenous vein bypass graft atherosclerotic lesions," *J. Am. Coll. Cardiol.*, vol. 24, pp. 1639–1644, 1994.

[97] D. Beattie, C. Xu, R. Vito, S. Glagov and M.C. Whang, "Mechanical analysis

of heterogeneous, atherosclerotic human aorta," *Journal of Biomechanical Engineering*, vol. 120, pp. 602–607, 1998.

[98] S.D. Williamson, Y. Lam, H.F. Younis, H. Huang, S. Patel, M.R. Kaazempur-Mofrad and R.D. Kamm, "On the sensitivity of wall stresses in diseased arteries to variable material properties," *Journal of Biomechanical Engineering*, vol. 125, pp. 147–155, 2003.

[99] P.B. Dobrin and J.M. Doyle, "Vascular smooth muscle and the anisotropy of dog carotid artery," *Circulation Research*, vol. XXVII, pp. 105–119, 1970.

[100] P.S. Steif, M.C. Palastro and Y. Rabin, "Analysis of the effect of partial vitrification on stress development in cryopreserved blood vessels," *Medical Engineering & Physics*, vol. 29, pp. 661–670, 2007.

[101] R.M. Jones, "Macromechanical behavior of a lamina," in *Mechanics of Composite Materials*, New York: McGraw-Hill Book, pp. 31–57, 2nd Ed., 1975.

[102] A.P. Boresi and K.P. Chong, *Elasticity in Engineering Mechanics*, New York: Wiley-Interscience Publication, pp. 261–271, 2nd Ed., 2000.

[103] D.J. Patel and J.S. Janicki, "Static elastic properties of the left coronary circumflex artery and the common carotid artery in dogs," *Circ. Res.*, vol. 27, pp. 149–158, 1970.

[104] M.L. Palmeri, and K.R. Nightingale, "On the themal effects associated with radiation force imaging of soft tissue," *IEEE Transaction on Ultrasonics, Ferroelectrics, and Frequency Controls*, vol. 51, no. 5, pp. 551–565, May 2004.

[105] Y.W. Kwon and H. Bang, *The Finite Element Method*, Boca Raton, FL: CRC Press, 2nd Ed., 2000.

[106] R. Skalak, "Growth as a finite displacement field," *In Proc. IUTAM Symp. on Finite Elasticity*. D.E. Carlson and R.T. Shield, The Hague: Martinus Nijhoff, 1981, pp. 348–355.

[107] R. Skalak, G. Dasgupta, M. Moss, E. Otten, P. Dullemeijer and H. Vilmann, "Analytical description of growth," *J. Theor. Biol.*, vol. 94, pp. 555–577, 1982.

[108] R. Skalak, S. Zargaryan, R.K. Jain, P.A. Netti and A. Hoger, "Compatibility and the genesis of residual stress by volumetric growth," *J. Math. Biol.*, vol. 34, pp. 889–914, 1996.

[109] E.K. Rodriguez, A. Hoger and A.D. McCulloch, "Stress-dependent finite growth in soft elastic tissues," *J. Biomechanics.*, vol. 27, pp. 455–467, 1994.

[110] V.A. Lubarda and A. Hoger, "On the mechanics of solids with a growing mass," *International Journal of Solids and Structure*, vol. 39, pp. 4627–4664, 2002.

[111] L.E. Malvern, *Introduction to the Mechanics of a Continuous Medium*, Englewood Cliffs, NJ: Prentice-Hall, 1969.

[112] R.M. Bowen, *Introduction to Continuum Mechanics for Engineers*, New York: Plenum Press, 1989.

[113] P. Chadwick, "Thermo-mechanics of rubberlike materials," *Philosophical Transactions of the Royal Society of London. Series A, Mathematical and Physical Sciences*, vol. 276, pp. 371–401, 1973.

[114] C. Truesdell and W. Noll, *The Non-linear Field Theories of Mechanics*, Berlin, Germany: Springer-Verlag, 1965.

[115] Benjamin Loret and F.M.F. Simoes, "A framework for deformation, generalized diffusion, mass transfer and growth in multi-species multi-phase biological tissues," *European Journal of Mechanics A/Solids*, vol. 24, pp. 757–781, 2005.

[116] W.M. Lai, D. Rubin and E. Krempl, *Introduction to Continuum Mechanics*, Oxford, Pergamon Press, 1978.

[117] J. Lubliner, *Plasticity Theory*, New York: Macmillan Publishing Company, 1990.

[118] P. Chadwick and L.T.C. Seet, *Trends in Elasticity and Thermoelasticity*, Groningen, The Netherlands: Wolters-Noordhoff, 1971.

[119] A.G. ten Have, F.J.H. Gijsen, J.J. Wentzel, C.J. Slager, and A.F.W. van der Steen, "Temperature distribution in atherosclerotic coronary arteries: influence of plaque geometry and flow (a numerical study)," *Physics in Medicine and Biology*, vol. 49, pp. 4447–4462, 2004.

VITA

Taehong Kim received his Bachelor of Science degree in mechanical engineering from Ajou University in Korea in 1999. He entered the Mechanical Engineering program at Texas A&M University in September 2000 and received his Master of Science degreee in May 2003. His research interests include bio-heat transfer and fluid mechanics.

Mr. Kim may be reached at 10806 Kingslake Dr. Apt.#D, Cincinnati, OH 45242. His email is mechlist@hotmail.com

The typist for this dissertation was Taehong Kim